



Ghent University
Faculty of Sciences

Scalable Synthesis of Covalent Organic Frameworks for Capture and Conversion of Carbon Dioxide

Andreas Laemont



Dissertation to obtain the degree of
Doctor of Science: Chemistry
Academic year 2024–2025

Promotors

Prof. Dr. Pascal Van Der Voort Ghent University
Dr. Karen Leus Ghent University

Affiliation

Chair

Prof. Dr. Laszlo Vincze Ghent University

Affiliation

Members of the jury

Prof. Dr. Sven Rogge Ghent University
Prof. Dr. Filip Du Prez Ghent University
Prof. Dr. Kristof Van Hecke Ghent University
Prof. Dr. Tom Breugelmans University of Antwerp
Dr. Chidharth Krishnaraj JSR Micro NV

Affiliation

Ghent University
Faculty of Sciences

Department of Chemistry
Krijgslaan 281 Building S3, 9000 Gent, Belgium

© 2021 Ghent University, Department of Chemistry, COMOC-Center for Ordered Materials, Organometallics & Catalysis, Krijgslaan 281-S3, 9000 Gent, Belgium

Alle rechten voorbehouden. Niets uit deze uitgave mag worden gereproduceerd, opgeslagen in een geautomatiseerd gegevensbestand, of openbaar gemaakt, in enige vorm of op enige wijze, hetzij elektronisch, mechanisch, door printouts, kopieën, of op welke manier dan ook, zonder voorafgaande schriftelijke toestemming van de uitgever.

All rights reserved. No part of this publication may be reproduced, stored in a retrieval system or transmitted in any form or by any means, electronic, mechanical, photocopying, recording or otherwise, without prior permission from the publisher.

Acknowledgements

to be added

Contents

Acknowledgements	iii
Summary	ix
Samenvatting	xiii
1. Introduction	3
1.1. One name, many materials	3
1.1.1. Linker variation	5
1.1.2. Linkage variation	7
Imine	8
Thiazole	9
Triazine	11
1.1.3. Topology Variation	13
1.2. Applications	15
1.2.1. Covalent organic frameworks for carbon capture and utilization	16
1.2.2. CO ₂ sorption	17
1.2.3. CO ₂ conversion	20
Electrochemical reduction of CO ₂	20
Photochemical reduction of CO ₂	22
Hydrogenation of CO ₂	24
1.3. Challenges	25
Scalability	25
Generalizability	26
Pore collapse	27
1.4. Thesis outline	29

References	31
2. Simplifying Solvothermal Synthesis of Covalent Organic Frameworks	43
2.1. Introduction	44
2.2. Optimization of imine-linked COF synthesis	45
2.3. The role of the solvent on the formation of COFs	48
2.4. General green synthesis of imine-linked COFs	55
2.5. A terpyridine covalent organic framework	57
2.5.1. A preliminary test: photocatalytic CO ₂ reduction	61
2.6. Conclusion	64
2.7. Experimental	65
2.7.1. Monomer synthesis	65
2.7.2. Optimization of COF synthesis	70
2.7.3. General COF synthesis	70
2.7.4. Synthesis of TABPy-TFM	72
2.7.5. Materials characterization	73
2.7.6. Photocatalytic CO ₂ reduction	74
2.7.7. Structural modelling	75
References	75
3. Linkage modification of covalent organic frameworks for enhanced CO₂ sorption	81
3.1. Introduction	82
3.2. Synthesis and characterization	83
3.3. CO ₂ sorption performance	90
3.4. Conclusion	91
3.5. Experimental	91
3.5.1. Monomer synthesis	91
3.5.2. Synthesis of TAPB-TTT and TAPB-TTT-S	92
3.5.3. Materials Characterization	93
3.5.4. Structural Modelling	94
References	96

4. Covalent Triazine Framework/Carbon Nanotube Hybrids as Electrocatalysts for the Reduction of CO₂	99
4.1. Introduction	100
4.2. Synthesis of CTF@MWCNT hybrids	101
4.3. Characterization of CTF@MWCNT hybrids	105
4.4. Electrocatalytic performance CTF@MWCNT hybrids	110
4.5. Conclusion	113
4.6. Experimental	114
4.6.1. Linker Synthesis	114
4.6.2. Synthesis of MWCNT-OH	115
4.6.3. Synthesis of CTF@MWCNT-OH hybrid materials	115
4.6.4. Materials Characterization	116
References	118
5. Conclusions	123
5.1. Conclusions	123
A. Appendix	125
A.1. Supporting information of Chapter 1	125
A.2. Supporting information of Chapter 2	126
A.3. Supporting information of Chapter 3	141
A.4. Supporting information of Chapter 4	143
A.5. Scientific Publications	151
References	154

Summary

Covalent organic frameworks (COFs), discovered in 2005, are crystalline porous materials that hold promise for many applications. In particular, due their abundant nanopores and catalytic properties, COFs show a lot of potential for carbon capture and utilization (CCU). However, despite promising academic results, industrial implementation of COFs has thus far not been realized. In this work, we have tried to improve both the synthesis of COFs on a large scale and their applications for the capture and utilization of CO₂.

In **chapter 1**, we give an introduction to what exactly covalent organic frameworks are. The different levels of variability - linker, linkage and topology - are discussed, with examples relevant to this thesis. We then give a brief overview of reported applications of these materials. In a second part of this chapter, we talk about carbon capture and utilization, and how COFs can be used for this application. An overview of the state-of-the art COFs is given for the adsorption of CO₂ and the different methods of converting CO₂. We take a closer look at why COFs are not yet industrialized and discuss the challenges that would need to be overcome in order to make it so. Finally, we outline what will be done in this thesis in order to improve the synthesis of imine COFs, and advance their use for carbon capture and utilization.

Chapter 2 introduces a mild, green and general method for scalable solvothermal synthesis of imine COFs. We start by optimizing five reaction parameters - solvent nature, water content, acetic acid content, temperature and time - on one single model COF. With the optimal conditions - n-butanol containing 10% H₂O and 4M AcOH at 70°C for 16

hours - we prepare and characterize an additional eleven distinct COFs. Furthermore, we attempt to understand why this solvent works well for COF synthesis, and others do not. From the combined observations of optical microscopy, SEM, TEM, FT-IR and in situ Raman, we propose a mechanism for the solvent-dependent synthesis of COFs. We hypothesize how this mechanism is linked to the concepts of stacking and pore collapse, and perform control experiments to see if our findings can be extended to other solvents. We show that by this method, imine COF synthesis can be easily scaled up to produce over 10 gram of COF in one batch. We apply our newly found method to produce a new COF, containing a terpyridine ligand. This ligand can be loaded with metals to create active sites for catalysis. As a proof of concept, we show that decoration with inexpensive $\text{CuCl}_2 \cdot 2\text{H}_2\text{O}$ yields a photocatalyst capable of highly selective CO generation.

In **chapter 3**, we study the influence of linkage conversion on the CO_2 capture capabilities of covalent organic frameworks. Using the method devised in the previous chapter, we produce an imine linked COF containing the highly nitrogen-rich (tris((1,2,4)triazolo)-(1,3,5)-triazine motif. Via a post-synthetic modification process, we convert the imine-linked COF to a thiazole-linked COF, which is characterized in depth via FTIR, PXRD, N_2 -sorption and XPS. The resulting COF showed an 87% increase in CO_2 uptake at 1 bar and 273 K compared to the parent imine COF, accompanied by a decrease in isosteric heat of adsorption.

Chapter 4 addresses the use of covalent triazine frameworks (CTFs) as electrocatalysts for CO_2 reduction. To overcome the low conductivity of these materials, we prepare hybrid electrocatalysts by growing a layer of CTF on premodified highly conductive multiwalled carbon nanotubes (MWCNTs). Starting from three monomers with varying nitrogen content, we prepare three different hybrid CNT@MWCNT materials. These are thoroughly characterized by elemental analysis, XRD, N_2 -sorption, XPS and ADF-STEM, before being tested for electrocatalytic reduction of CO_2 . The CTF@MWCNT hybrids are shown to be capable of reduction of CO_2

towards CO, with a maximum Faradaic Efficiency of 81 % at a very low overpotential of 380 mV. Via control experiments, we prove that the in situ growth of CTF on conductive carbon nanotubes increases the amount of CO produced by more than a factor 10 as compared to a physical mixture of CTF and MWCNTs.

Finally, in **chapter 5**, we discuss the general conclusions of this work.

Samenvatting

Covalent organische roosters (COFs), ontdekt sinds 2005, zijn kristallijne poreuze materialen die veelbelovend zijn voor zeer veel toepassingen. Door door hun nanoporiën en katalytische eigenschappen vertonen COFs veel potentieel voor de sorptie en omzetting van CO₂. Ondanks veelbelovende academische resultaten is industriële toepassing van COFs tot nu toe echter uitgebleven. In dit werk hebben we geprobeerd om zowel de synthese van COFs op grote schaal, als hun toepassingen voor de sorptie en omzetting van CO₂ te verbeteren.

In **hoofdstuk 1** geven we een introductie over wat covalent organische roosters precies zijn. De verschillende niveaus van variabiliteit - linker, *linkage* en topologie - worden besproken, met voorbeelden die relevant zijn voor deze thesis. Vervolgens geven we een kort overzicht van gerapporteerde toepassingen van deze materialen. In een tweede deel van dit hoofdstuk bespreken we de sorptie en omzetting van CO₂, en hoe COFs voor deze toepassing kunnen worden gebruikt. Er wordt een overzicht gegeven van de beste COFs voor de adsorptie van CO₂ en de verschillende methoden om CO₂ om te zetten d.m.v. COFs. We gaan dieper in op de vraag waarom COFs tot op heden nog niet geïndustrialiseerd zijn, en bespreken de uitdagingen die overwonnen moeten worden om dat wel te doen. Tot slot schetsen we wat er in deze thesis gedaan zal worden om de synthese van imine COFs te verbeteren en het gebruik ervan voor koolstofafvang en -gebruik te bevorderen.

Hoofdstuk 2 introduceert een milde, groene en algemene methode voor schaalbare solvothermale synthese van imine COFs. We beginnen met

het optimaliseren van vijf reactieparameters - de aard van het oplosmiddel, watergehalte, azijnzuurgehalte, temperatuur en tijd - op één welbepaalde imine COF. Met de optimale condities - reactie in n-butanol met 10% H₂O en 4M azijnzuur bij 70°C gedurende 16 uur - synthetiseren en karakteriseren we nog eens elf verschillende COFs. Verder proberen we te begrijpen waarom net dit oplosmiddel goed werkt voor COF-synthese, en andere niet. Op basis van de gecombineerde waarnemingen van optische microscopie, SEM, TEM, FT-IR en *in situ* Raman stellen we een mechanisme voor voor de synthese van COFs afhankelijk van het solvent. We stellen een hypothese op over hoe dit mechanisme gekoppeld is aan de concepten van *stacking* en *pore collapse*, en voeren controle-experimenten uit om te zien of onze bevindingen kunnen worden uitgebreid naar andere oplosmiddelen. We demonstreren dat met deze methode de synthese van imine COFs eenvoudig kan worden opgeschaald tot meer dan 10 gram COF in één keer. We passen onze nieuw gevonden methode verder toe om een nieuwe COF te produceren die een terpyridine-ligand bevat. Dit ligand kan worden beladen met metalen teneinde actieve sites voor katalyse te creëren. Als *proof of concept* laten we zien dat belading van de terpyridine COF met CuCl₂·2H₂O een fotokatalysator oplevert die zeer selectief CO kan genereren.

In **hoofdstuk 3** bestuderen we de invloed van de omzetting van de *linkages* op het vermogen van covalente organische raamwerken om CO₂ op te vangen. Met behulp van de methode uit het vorige hoofdstuk produceren we een imine-gelinkte COF dat het zeer stikstofrijke (tris((1,2,4)triazolo)-(1,3,5)-triazine-motief bevat. Via een post-synthetisch modificatieproces zetten we de imine-gelinkte COF om in een thiazool-gelinkte COF, die grondig wordt gekarakteriseerd via FTIR, PXRD, N₂-sorptie en XPS. De resulterende COF vertoont een toename van 87% in de opname van CO₂ bij 1 bar en 273 K vergeleken met de oorspronkelijke imine COF, samen met een afname van de isosterische adsorptiewarmte.

Hoofdstuk 4 behandelt het gebruik van covalent triazine roosters (CTFs) als elektrokatalysatoren voor de reductie van CO₂. Om de lage elektri-

sche geleidbaarheid van deze materialen te verbeteren, synthetiseren we hybride elektrokatalysatoren door een laag CTF te groeien op voorgemodificeerde hooggeleidende meerwandige koolstofnanobuizen (MWCNTs). Uitgaande van drie monomeren met variërend stikstofgehalte bereiden we drie verschillende hybride CNT@MWCNT-materialen. Deze worden grondig gekarakteriseerd door middel van elementaire analyse, XRD, N₂-sorptie, XPS en ADF-STEM, voordat ze getest worden voor de elektrokatalytische reductie van CO₂. De CTF@MWCNT hybriden blijken in staat tot reductie van CO₂ naar CO, met een maximale Faradaic Efficiency van 81 % bij een zeer lage overpotentiala van 380 mV. Via controle-experimenten bewijzen we dat de *in situ* groei van de CTF op de geleidende koolstofnanobuizen de hoeveelheid geproduceerd CO met meer dan een factor 10 verhoogt in vergelijking met een fysisch mengsel van CTF en koolstofnanobuizen.

Tot slot bespreken we in **hoofdstuk 5** de algemene conclusies van dit werk.

Introduction

Covalent organic frameworks (COFs) are a class of crystalline porous organic 2D or 3D polymers which were discovered by Yaghi et al. in 2005. COFs are constructed starting from organic monomers, denoted as the 'linkers', coupled together via covalent bonds, denoted as 'linkages'. One, two or even more linkers react with one another, forming reticular structures. The strength of COFs lies in the fact that the structure of a COF can be predicted *a priori* given sufficient knowledge of the linker and linkage. This allows for precise control of the structure and chemical properties of the resulting material at the molecular level.

1.1 One name, many materials

COFs are a very active field of research: since their discovery in 2005, over 14000 articles have been published on the topic, with over 2800 alone in the year 2023 (**Figure A.1**). The reason for this can be found in the immense variability of this materials class. For a start, there is a very wide array of possible linkers, small, typically rigid organic monomers with two or more reactive endgroups. These can then be combined with one another using different linkages, by changing the nature of the reactive group on the linker. Then there are many different topologies which the COFs can take, depending on the symmetry of the linkers. The same two linkers can give two COFs with different topologies, depending on the reaction conditions that were used (**Figure 1.1**).

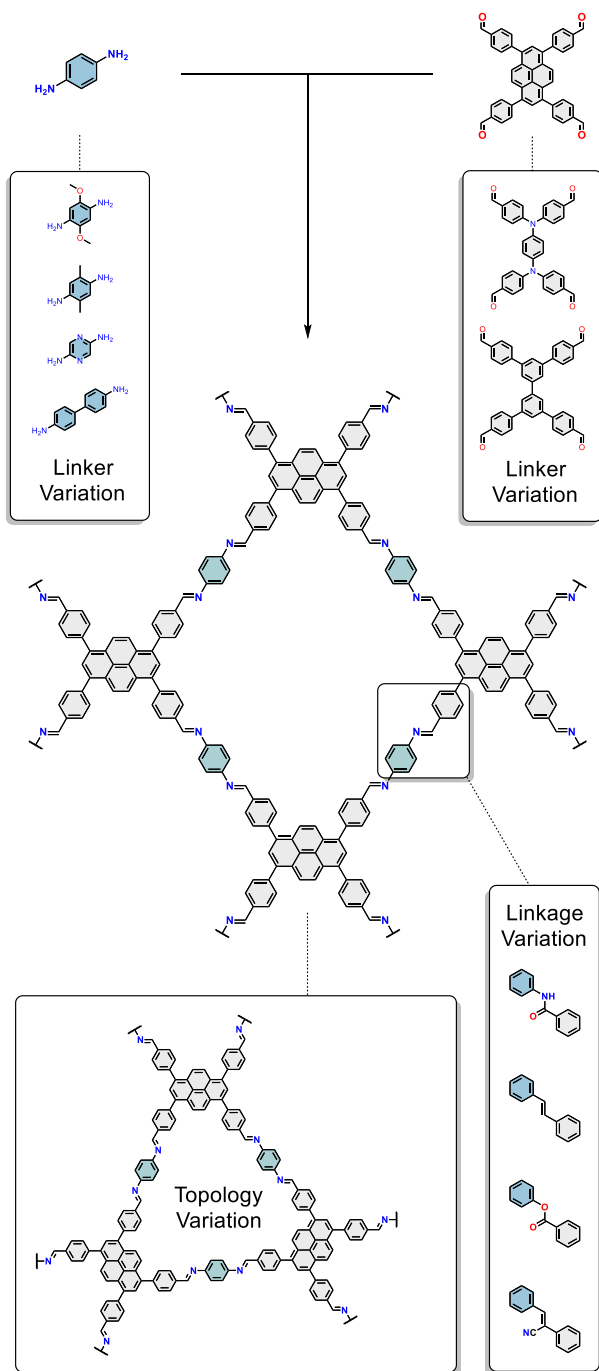


Figure 1.1. An example of a COF synthesis, showing the three levels of variability: variation in linkers, linkages and topology.

One can immediately appreciate that because of these three different ways of variability, the set of possible COFs that can be formed is extremely large. Below, we elaborate on the concepts of linker, linkage and topology, and show some common examples.

1.1.1 Linker variation

As we mentioned above, a COF is made up of repeating organic monomers, the linkers. Linkers come in all shapes and sizes. The only theoretical prerequisites are that they contain at least two reactive groups which can form linkages, and possess a suitable symmetry to be able to combine with another linker into a regular structure. Other than that pretty much the only restriction is the imagination of the materials scientist (and his or her organic synthesis skills to actually make them). In **Figure 1.2**, a small selection is given of reported linkers which have been used to synthesize COFs. The specific linkers that were used in this thesis are highlighted in blue. Note that this is only a fraction of all reported linkers, and new linkers are being synthesized every year. The linkers can be classified in terms of the number of reactive groups they bear that are able to form linkages. Linkers with two, three, four or six reactive groups are denoted as di-, tri-, tetra-, or hexatopic respectively - pentatopic linkers exist as well, but are very rare [1]. The grand majority of COF linkers are rigid and twodimensional, for the simple reason that most linkers are based on aromatic systems. However, linkers containing flexible bonds, or even completely non-aromatic linkers, have also been reported [2–4]. The combination of two two-dimensional linkers gives in most (but not all [5, 6]) cases rise to two-dimensional COFs. As a result, 2D COFs make up the vast majority of reported COFs in literature. The linkers can be tuned according to the desired properties of the resulting COF: substituents, such as hydroxylgroups or halides can be introduced, or heteroatoms within the aromatic rings.

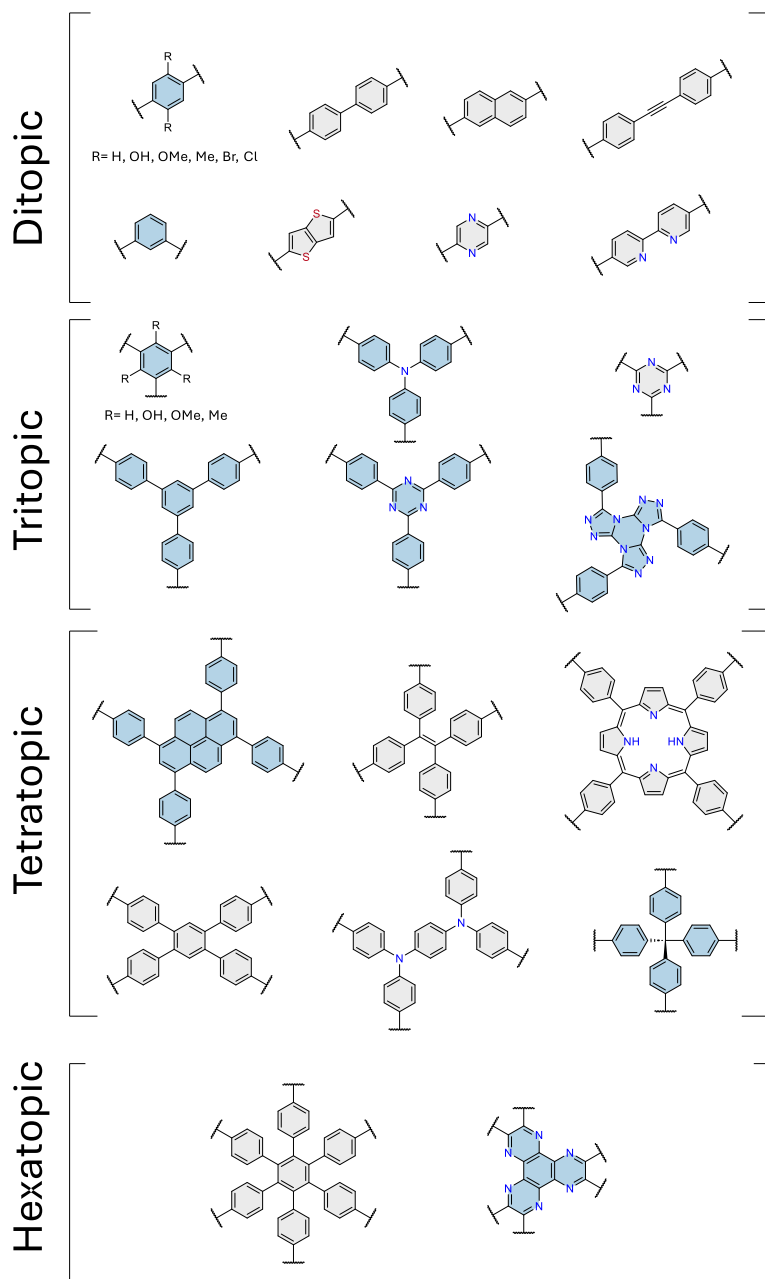


Figure 1.2. An overview of some of the linker architectures used in COF synthesis, sorted by number of linker groups. The teal circles depict a functional linker group. The monomers depicted in blue were used in this thesis.

1.1.2 Linkage variation

The choice of available linkages is markedly more limited than that of the linkers. The formation of a COF requires a chemical reaction that forms in the end a covalent bond that is thermodynamically strong enough to drive the polymerization reaction towards the side of the COF. On the other hand, to form a crystalline structure, the process of error-correction is vital. During the synthesis, the monomers bind randomly to one another, usually not immediately in the desired crystalline topology. If the linkage formation is sufficiently reversible, the COF formation reaction is under thermodynamic control. The linkage bond can be formed, broken, and reformed very fast, so that a reaction which leads to a linker being in the wrong place to form a regular structure, can be easily corrected by breaking the bond. In this way, the intermediates can equilibrate in a reasonable amount of time towards the thermodynamically most stable product, the crystalline COF. If the formed linkage is chemically very stable, the linkage formation reaction is a lot less reversible, and the reaction is under kinetic control. A linker which has reacted in the wrong place, will stay there, and create defects in the crystalline structure - or if too many errors occur, lead to an amorphous structure altogether.

Error-correction can take place much faster when the formed bonds are less stable. As a result of this, COF synthesis is faced with a dilemma:

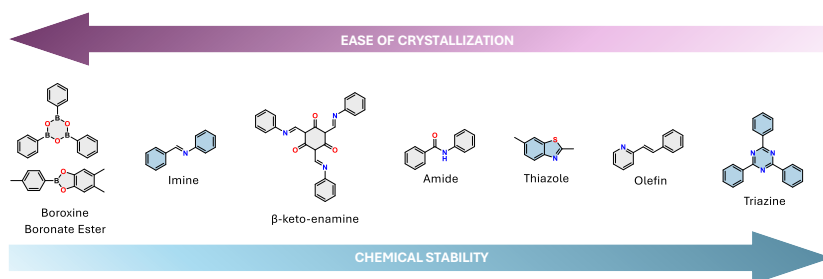


Figure 1.3. An overview of common linkages in COF formation. The linkage types used in this thesis are colored in blue.

less stable linkage types such as boroxines typically can be made with high crystallinity and less defects under mild conditions, but have less practical applications due to their limited chemical stability. COFs with chemically very stable linkages such as olefin and triazine bonds are much more resilient to chemical degradation, but as a result require much harsher conditions to form a crystalline material. This in turn limits the number of linkers than can be used with this linkage: certain functionalities on the linker might give side reactions during the COF formation. Quite some research has been dedicated to identifying new, milder conditions, that allow for the formation of stable COFs with high crystallinity. At the same time, new linkage types are still being discovered. In **Figure 1.3** a selection of the most reported types of linkage are shown, ordered by their chemical stability. The linkage types that will occur in this thesis are colored in blue, we briefly discuss those types below.

Imine

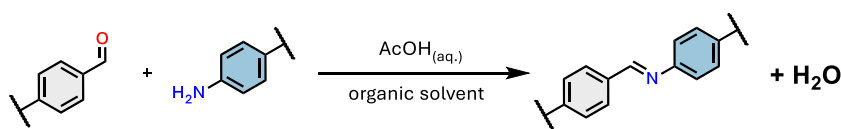


Figure 1.4. Overview of the most common synthesis method for imine-linked COFs

The first imine-linked COF was introduced in 2009 by Uribe-Romo et al., from the group of Omar Yaghi. The imine linkage is conveniently made by condensation of an aldehyde and an amine group, with the loss of a molecule of water. Although ketone groups can in theory also form imine linkages, they are rarely used for COF formation [7].

Imine-linked COFs make up the grand majority of all reported COFs thus far. This can be explained by the fact that the imine linkage is a good compromise between bond reversibility and bond stability. The most common route of imine COF synthesis is solvothermal. Both monomers

are dissolved in an organic solvent, and an aqueous solution of acetic acid is added. The reaction mixture is then heated under inert atmosphere, usually to 120 °C for 72 hours. The water in the reaction mixture can hydrolyze the newly formed imine bonds, increasing the rate of the reverse reaction and thus the degree of error-correction. The acetic acid acts as a catalyst, improving the reaction rate of the forward and reverse reaction and thus speeding up the crystallization process. Under these conditions, an imine-linked COF can be obtained with, depending on the linker, medium to very high crystallinity. On top of that, both amine and aldehyde groups are synthetically easily accessible, meaning there exists a wide variety of possible linkers that are either commercially available or readily synthesized.

A typical imine COF can withstand treatment with organic solvents and neutral water, but will hydrolyze in strongly alkaline or acidic conditions. With the right choice of linker, the stability can be enhanced. These relatively stable bonds allow imine COFs to be used for a plethora of applications, as will be discussed in **section 1.2**.

Thiazole

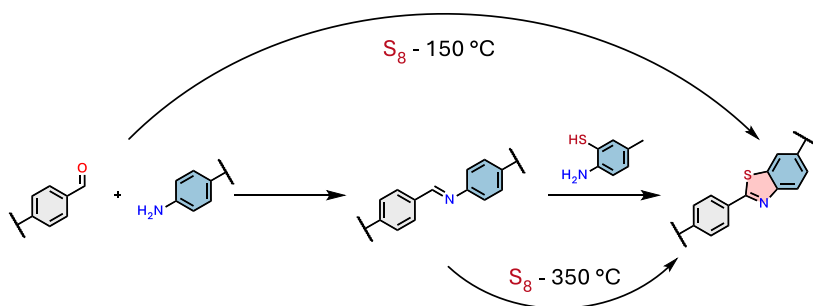


Figure 1.5. Overview of the most common synthesis methods for thiazole-linked COFs

The thiazole linkage is a much more stable bond. The fused structure is strongly conjugated, and difficult to break. In theory, this linkage could be

formed by condensation of aldehyde with an aromatic amine containing a thiol group in the ortho-position. However, this reaction is insufficiently reversible to allow for efficient error correction, and amorphous materials are obtained as a result.

An elegant workaround for this problem can be found in post-synthetic modification. Instead of building the stable thiazole linkage *de novo*, it can be made by modification of a previously made crystalline imine COF. The conversion of imine to thiazole linkage is an irreversible reaction, but since it starts from a crystalline material, this is not an issue: the crystallinity of the original imine COF is largely retained. In this way, post-synthetic modification solves the COF synthesis dilemma: a material with both high crystallinity and high stability can be obtained.

So far, three routes have been reported to convert imine COFs to thiazole COFs. Waller et al., again from the group of Yaghi, converted an imine linked COF based on a 1,4-phenylenediamine linker [8]. After synthesis, these linker moieties were substituted with 2,5-diaminobenzene-1,4-dithiol dihydrochloride. This causes the mild introduction of thiol groups in ortho-position to the imine bond. These then cyclize to form thiazoline groups, which were oxidized under an atmosphere of oxygen to form thiazole groups. The same strategy could also be applied to form benzoxazole linkages, by using 2,5-diaminohydroquinone dihydrochloride. While very mild, this method is restricted to amine monomers for which a thiol-functionalized substitute is available. Furthermore, it requires a fourfold excess of the thiolated monomer to sufficiently drive the substitution reaction, and the applicability was only demonstrated for one single imine-linked framework.

A harsher conversion method was demonstrated by Haase et al [9] in 2018. They treated an imine COF with molten elemental sulfur at 150°C, then at 350°C for three hours under inert atmosphere. At this temperature, the molten sulfur reacts with the imine bond to form an intermediate thioamide, which then cyclizes to form a thiazole. This method only needs very cheap elemental sulfur, and relatively short reaction times.

The authors demonstrated that the method works on at least two different COFs, and later articles using the same method have further proved the wide applicability [10–12]. However, the high temperature limits the scope of COFs that can be used: COFs containing temperature- or oxidation sensitive groups will likely undergo side reactions under the harsh thiazole-forming conditions.

Wang et al. continued on these findings in 2020, by performing the imine COF formation and the subsequent conversion to thiazole in one multicomponent reaction [13]. Practically, the imine COF synthesis was performed in the presence of elemental sulfur at a temperature of 150°C, with a small amount of DMSO as an oxidant. This method has the advantage of forming the thiazole-linked COFs in one pot, saving on time and reagents. However, elemental analysis indicated that the conversion to thiazole was not fully completed: depending on the linkers only ca. 80% to 90% of the imine bonds were converted to thiazole bonds. Furthermore, the authors only demonstrate the applicability of this method for amine containing linkers based on electron-rich anthracene-2,6-diamine or naphthalene-2,6-diamine linkers. The original organic procedure also mentions that the same reaction conditions do not work in the case of less electron-rich amines, such as aniline derivatives. This severely limits the amount of COFs that can be made using this procedure.

A typical triazine COF, due to the strong conjugated linkage, can withstand harsher conditions than an imine-linked COF. Even after treatment with strong acids and bases (14 M HCl, 14 M NaOH), reductants (1 M NaBH₄) or nucleophiles (1 M N₂H₄), thiazole-linked COFs have been shown to retain their crystallinity for the most part [9].

Triazine

The triazine linkage is the most stable bond that can be used to make crystalline COFs. The first report on this class of COFs was made in 2008

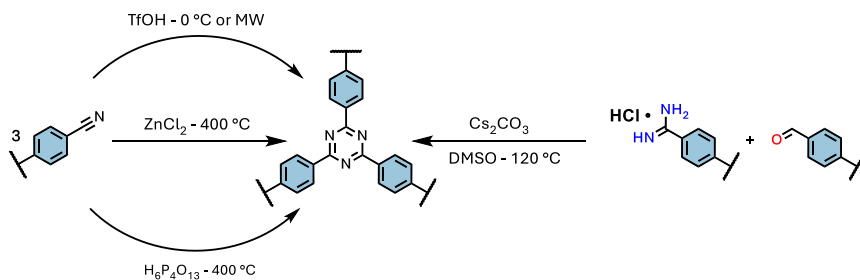


Figure 1.6. Overview of the most common synthesis methods for triazine-linked COFs

by the group of Antonietti and Thomas [14]. They prepared a triazine-linked COF by trimerization of nitrile-functionalized monomers, and coined the resulting materials as covalent triazine frameworks, CTFs. The trimerization of nitriles has a very high activation energy and is a poorly reversible reaction, which requires very harsh conditions to occur. The original synthesis method is ionothermal: the COF synthesis proceeds in an ionic melt of ZnCl_2 at 400 °C or higher. Even under these conditions, only a handful of monomers is capable of forming semi-crystalline materials. Because of the high temperature, partial carbonization occurs, leading to black materials with defects in their structure.

Over the years, some improvements could be made: Ren et al. from the group of prof. Cooper found out that CTFs could be made using trifluoromethanesulfonic acid (TfOH) at room temperature [15]. The resulting materials were amorphous, but not carbonized. When the reaction mixture was heated to 110 °C using a microwave, CTFs with weak crystallinity could be obtained. Because carbonization did not occur, the CTFs made by this method had a yellow to brown color, which allows them to be used for new applications, like photocatalysis. However, the reliance on TfOH, a superacid with a pKa of -14.7, limits the scope of monomers that can be used.

A radically different method was discovered by Wang et al., again from the group of Cooper. Instead of starting from very stable nitrile-

containing linkers, they started the synthesis from more reactive amidine-functionalized linkers. These can react with aldehyde-functionalized linkers to form triazine linkages via a relatively low-temperature (120 °C) polycondensation reaction [16]. The resulting materials showed moderate crystallinity, and were not carbonized. Minor improvements in the crystallinity could be gained by slow addition of the linkers, in situ generation of the aldehyde linkers, or the use of NaCl as a heterogeneous nucleation agent [17–19].

A breakthrough came in 2021, when Sun et al. reported a general and rapid synthesis method for synthesis of highly crystalline CTFs [20]. The method relies again on the superacid TfOH. By microwaving the monomers in TfOH at a temperature of 240-160 °C, they could obtain highly crystalline, non-carbonized CTFs in 20 minutes. The synthesis could even be performed in a regular domestic microwave. However, the use of TfOH at temperature above its boiling point (162 °C) poses some risk that might be an issue for upscaling. The authors noted themselves that the amount of triflic acid needs to be carefully controlled to avoid the extensive pressure causing an explosion.

The same group reported in 2022 a safer method that does allow for the scalable synthesis of crystalline CTFs. Instead of trifluoromethanesulfonic acid, they used this time polyphosphoric acid ($H_6P_4O_{13}$). The linkers were heated in this viscous acid at 300°C or 400°C to yield highly crystalline materials [21]. The synthesis could be scaled to produce 0.5 kg of CTF in one batch. Due to very strong triazine units, CTFs display exceptional chemical stability, surviving even strong alkaline and acid treatments at elevated temperatures.

1.1.3 Topology Variation

A final degree of variation can be found in the different topologies of the COF. Even with exactly the same linkers and linkages, different COFs can be made that are distinguished by their topology. The topology of a

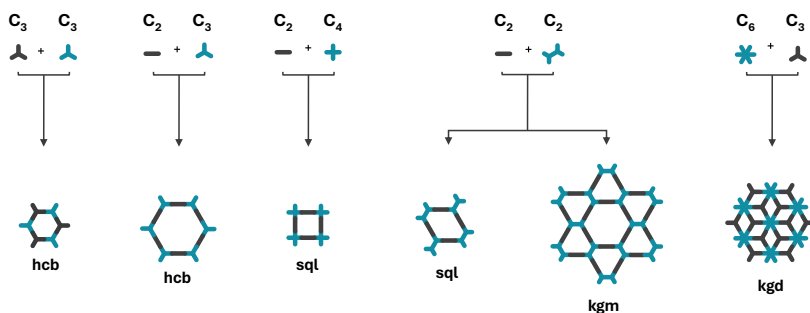


Figure 1.7. Overview of some common topologies for 2D COFs that can be formed depending on the geometry of the linkers.

COF is dependent on the geometry of and number of functional groups present on the linkers. An overview of common 2D COF topologies is shown in **Figure 1.7**.

For 2D COFs, often only one specific topology can be formed with one specific set of linkers. For example, the combination of two planar C_3 linkers leads invariably to a COF with a hexagonal (hcb) topology. However, in some cases, the COF can crystallize in different topologies. An example of this is the combination of a ditopic linker with C_2 symmetry and a tetratopic linker with C_2 symmetry. In such cases, both a COF with a rhombic structure (sql) or a dual-pore Kagome lattice (kgm) can be obtained, depending on the synthetic conditions [22–24]. In 3D COFs, the variety tends to be larger, and two linker geometries could give rise to several possible topologies [25]. The exact topology of the COF can be determined via PXRD: the experimental pattern is compared to the theoretical patterns obtained from *in silico* simulations of the different possible structures. An interesting case is the work of Gui. et al from 2023, who demonstrated it is in some cases possible to form both a 2D or 3D COF from the same set of linkers [26]. The synthesis could be steered towards the desired topology by simply altering the reaction temperature.

1.2 Applications

Given the aforementioned immense variability of COFs, it should come as no surprise that the range of possible applications for these materials is equally broad. Covalent organic frameworks possess some very interesting properties that are found in few other material classes. Arguably the most important one is their ordered reticular structure: provided they are sufficiently crystalline, COF materials are very well defined. Owing to their bottom-up synthesis, the properties of the COF can be tuned precisely via the choice of linker, linkage and topology. In practice, this means that all sort of functionalities can be implemented in the COF structure based on the building blocks.

Another major feature of COFs is their intrinsic nanoporosity. Inbetween the connected linkers, the COF contains micro- and/or mesopores, with sizes typically ranging between 1 and 3 nm (with extremes down to 0.6 nm and up to 10 nm [27, 28]). Contrary to many other porous materials, these pores are very well-defined, with a very narrow size distribution. Furthermore, due to the very large density of small pores, the density and surface area of COFs is exceptional: COFs with an ultralow density of down to 0.106 g cm^{-3} and surface area up to $4200 \text{ m}^2 \text{ g}^{-1}$ have been reported [29, 30]. The combination of these two properties opens up an immense field of applications in adsorption, (electro)-catalysis, sensing, separation, energy storage, drug delivery.

Within the nanopores, gasses such as CO_2 , CH_4 or H_2 , can condense via capillary condensation to be separated from other other gasses or stored, with selectivity depending on the chemical nature and structure of the pore [31]. Dissolved molecules or ions can be retained by the pores, for the efficient removal of dyes or noxious chemicals like PFAS in solution, or on the other hand selective extraction of valuable targets like uranium or gold [32–35]. Reagents and substrates can diffuse through the pores and react with catalytic sites embedded in the COF, possible aided by nanoconfinement within the pores. The catalytic sites can be organic in

nature, introduced via the linker or via post-synthetic modification, or ligands can be built into the COF and then decorated with metals as active sites [36]. The pores can further be used as nanocarriers for controlled delivery of drugs like ibuprofen [37].

Another interesting property is the semiconducting nature of many covalent organic frameworks. This allows COFs to be used for opto-electronic applications, luminescence, and photocatalysis [38, 39]. The latter application specifically has gained much academic interest in the past years, with COFs displaying potential for efficient photocatalytic generation of valuable chemicals such as H_2 , H_2O_2 or CO [40–42].

In this work, we will specifically focus on applications of covalent organic frameworks that can be used for carbon capture and conversion.

1.2.1 Covalent organic frameworks for carbon capture and utilization

Global warming is without doubt one of the greatest problems facing humanity in the years to come. The buildup of CO_2 and other greenhouse gases in our atmosphere, due to excessive emissions from human activity, directly causes the average global temperature to rise. The global surface temperature was 1.09 °C higher in the period of 2011–2020 than in the period of 1850–1900 °C, and continues to rise [43]. Widespread and rapid changes in the atmosphere, ocean and biosphere are already occurring, with new weather and climate extremes happening ever more frequently. The predicted consequences of further temperature increase are nothing short of catastrophic: among (many) others, a rise in the global sea level, massive loss of biodiversity, strong declines in crop and fishery yields.

The solution is evident: the emission of CO_2 needs to decrease, fast and by a lot. One proposed strategy for this is carbon capture and utilization (CCU). Instead of emitting CO_2 to the atmosphere, it is captured, and

converted to a useful chemical or fuel. Possible products that can be made from chemical conversion of CO₂ are CO, methane, methanol and ethylene. In this way, CO₂ would be used as a feedstock, instead of a waste product. If implemented on a large scale, CCU could effectively close the human-made carbon cycle. The tricky part lies of course in finding an efficient way to capture and convert CO₂. Ideally, this should be done using sustainable energy, in a way that emits little to no greenhouse gasses in the process. There exist several strategies for CCU. In what follows, we discuss some of them, specifically those where COFs could be usefully applied.

1.2.2 CO₂ sorption

Carbon capture and utilization starts with capturing and separating CO₂ from various emission sources, or directly from the air. The flue gas generated in power plants for example typically consists of 15-16% CO₂, 73-77% N₂ and other minor components such as H₂O, CO, SO_x and NO_x. Currently, the most mature technology for CO₂-sorption is amine scrubbing. The flue gas flows into an aqueous solution of an alkyl amine, such as monoethanolamine (MEA). The amine reacts at low temperature with the CO₂ and water to form in the end ammonium bicarbonates. The captured CO₂ is then desorbed using heat or vacuum, which reverses the chemical process and regenerates the free amines. This method however requires a lot of energy for the regeneration step. Furthermore, the amines tend to degrade in the presence of contaminants like SO₂ and have poor oxidative stability [44].

Alternative strategies for CO₂ capture are therefore required. Much research has been invested in porous materials for physical adsorption of CO₂. Examples of proposed materials include silicas, carbons, zeolites and metal-organic frameworks. Covalent organic frameworks also show much promise for this application. Their structured porous nature allows for fast diffusion of CO₂ inside the material. Due to their high surface area

Name	Type	CO ₂ uptake (mmol g ⁻¹)	Q _{st} (kJ mol ⁻¹)	Reference
CALF-20	MOF	4.07	-39.0	[47]
Zeolite 13X	Zeolite	4.22	-49.0	[48, 49]
ne 3D-OC-COF-OH	Imine COF	2.30	-22.4	[50]
PyTTA-BFBIIm-iCOF	Imine COF	4.15	-30.2	[51]
PD-COF	Imine COF	2.44	-31.9	[52]
df-TzCTF600	Triazine COF	4.60	-34.0	[53]
TzCTF600	Triazine COF	2.51	-28.0	[53]
3D CTF-TPM	Triazine COF	3.17	-26.9	[54]
3D CTF-TPA	Triazine COF	2.43	-24.7	[54]

Table 1.1. CO₂ uptake and Q_{st} of some of the best-performing COFs, MOF CALF-20 and zeolite 13X. The CO₂ uptake shown is measured at 298 K and 1 bar.

and pore volume, a lot CO₂ could be potentially stored inside the pores. Because the COFs are made up only of light, non-metallic elements, they have a very low density, and as a result, their CO₂-uptake expressed per gram of material can be very high. The inherently present nitrogen atoms in imine- or triazine-linked COFs directly provide a group with high CO₂ affinity.

An overview of some of the best performing COFs for CO₂-sorption are shown in **Table 1.1**. We have compared these with two industrially produced porous materials that show very good performance for CO₂ sorption: zeolite 13X and MOF CALF-20. The latter material is produced on tonne scale by BASF since 2023, to be used for CO₂ capture by the company Svante [45, 46].

Most efforts to design COFs with high CO₂ capture performance in COFs have focused on topology and linker variation. In this way, the shape and size of the pore is tailored to alter the the gas uptake properties. For example, nanopores with a diameter smaller than 0.8 nm, denoted as ultra-micropores, tend to favor CO₂ sorption at low partial pressures (< 0.15 bar). However, at higher pressures, further uptake is hindered by mass transfer resistance, as CO₂ molecules are occupying the pores

[55]. In contrast, mesopores, with a pore diameter between 2 and 50 nm are more suitable for CO₂ sorption at ambient pressure or higher. By linker variation, the internal surface of the pores can be adapted to include groups with high CO₂-affinity. Examples include hydroxyl, amine or carboxylic acid groups. Such groups can be incorporated *de novo*, or via post-synthetic modification: for example Guan et al. prepared in 2019 a COF containing nitrile groups, which were then hydrolyzed to primary amines [56].

The two main parameters to define the CO₂-sorption performance of a material are the total CO₂ uptake and the isosteric heat of adsorption. The CO₂ uptake is for most COF literature measured at near-ambient conditions: 1 bar CO₂ pressure, and temperatures of either 273 K or 298 K. Typical values for CO₂ uptake at 298 K and 1 bar range from 1 to 5 mmol g⁻¹. An overview of the CO₂ uptake at 298 K and 1 bar of some of the best-performing COFs, MOF CALF-20 and zeolite 13X is given in **Table 1.1**. The best reported COFs have an uptake in the same range, but on average slightly below the benchmark values of CALF-20 and 13X.

In general, porous materials can adsorb gasses via two mechanisms: either physisorption or chemisorption. Physisorption describes a quite weak physical force between adsorbent and adsorbate by means of Van der Waal's interaction. Chemisorption on the other hand implies that a chemical bond is formed between adsorbent and adsorbate, i.e. electrons are shared between the two to some extent. A significantly higher amount of energy is needed to desorb a chemisorbed molecule than a physisorbed molecule. This brings us to the second parameter in **Table 1.1**, the isosteric heat of adsorption Q_{st} , expressed in kJ mol⁻¹. This metric describes the bond strength of the adsorbed CO₂ with the adsorbent. As a rule of thumb, adsorption processes with an isosteric heat of adsorption more negative than -50 kJ/mol are usually chemisorption processes, while physisorption processes tend to have a Q_{st} of between -25 and -35 kJ mol⁻¹. Materials with a strongly negative Q_{st} have a high binding affinity towards CO₂. This is advantageous for selective sorption

of CO₂ at low pressures, for examples for directly capturing CO₂ from air. However, a high absolute value for Q_{st} also implies that more thermal energy will be needed to desorb the CO₂ from the adsorbent afterwards. This increases the total cost of the CO₂ separation process. Ideally, a good CO₂ adsorbent should therefore have a high CO₂ uptake under the relevant conditions, combined with a high (i.e. less negative) Q_{st}. As seen from **Table 1.1**, several COFs show a significantly less negative Q_{st} than zeolite 13X and CALF-20. This means that CO₂ desorption from COFs would require a lot less energy compared to these materials.

1.2.3 CO₂ conversion

The second step of the CCU process is the conversion of CO₂ to a useful chemical. By (in theory) relatively simple conversion reactions, CO₂ could be used a renewable chemical feedstock to produce valuable industrial base chemicals such as hydrocarbons, methanol, formic acid, and ethylene. However, CO₂ is a relatively inert and thermodynamically stable species. Significant energy is required to break the strong C=O bond (799 kJ/mol). This energy can be supplied in many different forms, e.g. by means of heat, light or plasma. Catalysis is in almost all cases crucial to convert CO₂ at meaningful rate, and direct the conversion process towards one specific endproduct. In what follows, we discuss three conversion routes of CO₂ to industrially relevant chemicals for which COFs have been used as catalysts: electrochemical reduction of CO₂, photochemical reduction of CO₂ and hydrogenation of CO₂.

Electrochemical reduction of CO₂

For the electrocatalytic CO₂ reduction reaction (CO₂RR), electrons are supplied via an external source of potential to an electrode which is brought into contact with a (usually aqueous) electrolyte. CO₂ adsorbs

Material	Current density (mA cm ⁻²)	Main product	Faradaic Efficiency	Reference
NiPor-CTF	-52.9	CO	97 %	[57]
MWCNT-Por-COF-Co	-0.2	CO	99.3%	[58]
FN-CTF-400	- 18.77	CH ₄	99.3%	[59]
Cu-Tph-COF-Dct	- 220	CH ₄	80 %	[60]
Co-N-COF	- 446	HCOO ⁻	97.4%	[61]
TPTA-Pz	- 2.2	C ₂ H ₄	19.1 %	[62]
PcCu-TFPN	- 12.5	CH ₃ COO ⁻	90.3 %	[63]

Table 1.2. Overview of some of the best performing COFs for electrochemical CO₂ conversion.

on the electrode, and the electron is transferred from the electrode surface to the adsorbed molecule. Based on the consecutive electron transfer, proton transfer and rearrangement steps, several industrially interesting chemicals can be obtained, including carbon monoxide, formic acid, methane, ethylene or methanol. The electrocatalyst is situated at the surface of the electrode, and thus forms the interface between electrode, electrolyte and CO₂. Depending on the adsorption energy of the different intermediates on the electrocatalyst, the reduction reaction can be increased in rate and steered towards specific products. In general, it is more difficult to produce species with more hydrogen atoms (methane, ethylene, methanol), as these require multiple consecutive electron and proton transfers to occur. Because the reaction is typically performed in water, there is also significant competition from the hydrogen evolution reaction (HER). Again, a proper electrocatalyst can suppress this sidereaction and promote the CO₂RR. Electrochemical CO₂RR is especially interesting for industrialization because it can be performed at ambient pressure and atmosphere, is scalable, and can be directly driven by renewable electricity.

In the case of COFs for CO₂RR, often single atom metals are used as the active sites. To this end, a COF is synthesized which contains a ligand to hold the metal, e.g. bipyridine or porphyrine. The metal can

be introduced in the COF after synthesis, or into the ligand-containing monomer before synthesis. The well-defined metal environment makes it possible to selectively produce a single reduction product from CO₂. Because of the mild conditions (ambient pressure and temperature, near pH-neutral aqueous electrolyte) under which CO₂RR can be performed, several linkage types can be used. The most reported classes are imine and triazine-linked COFs. An overview of some of the best performing COFs for CO₂ reduction are shown in **Table 1.2**. The activity of electrocatalysts is typically measured via the current density in mA cm⁻², i.e. the current normalized to the geometric electrode area. It should be noted that this value is very dependent on the design of the electrochemical cell that is used for testing, which makes it difficult to compare values between different literature reports. The selectivity of the catalysts is expressed as Faradaic Efficiency (FE), and is obtained by dividing the current produced by the desired reaction by the total current.

COFs have some interesting advantages for electrochemical CO₂RR. For one, their high porosity allows efficient diffusion of electrolyte and CO₂ within the pores. The variability in design means interesting active sites can be built into the COF, which make it possible to target a wide range of reduction products. However, the conductivity of COFs is generally very low, in the order of 10⁻⁹ to 10⁰ S m⁻¹ [64]. For comparison, copper has a conductivity of 5.96 × 10⁷ S m⁻¹ [65]. For this reason, COF electrocatalysts are usually coated as thin layers on top of a highly conductive current collector. Nonetheless, while COF electrocatalysts often show very high selectivity, their activity remains quite low as compared to metal-based electrocatalysts due to their lower conductivity.

Photochemical reduction of CO₂

Instead of supplying the potential necessary to drive the reaction via an external source, this can also be done photochemically. Theoretically, the same product range can be obtained as with electrochemical CO₂RR.

Material	Activity ($\mu\text{mol g}^{-1} \text{h}^{-1}$)	Main product	Selectivity	Reference
CT-COF	156	CO	99.3 %	[66]
COF-367 NSs	10162	CO	78 %	[67]
CuABD	1260	HCOOH	16 %	[68]
Pt@bpyCTF	152	HCOOH	95 %	[69]
Mo-COF	1.08	CH ₄	9.96%	[70]
Mo-COF	3.57	C ₂ H ₄	32.92 %	[70]
TRITER-2	4750	CH ₃ OH	69 %	[71]

Table 1.3. Overview of some of the best performing COFs for photochemical CO₂ conversion

Briefly, under irradiation with light, an electron is excited from the valence band to the conduction band, creating an electron-hole pair. The excited electron is then used to reduce CO₂, while the hole induces an oxidation reaction, e.g. the oxidation of water to O₂. COFs are ideally suited for this. Due to their conjugated structure, COFs usually have a bandgap in or near the visible light range (1.63 to 3.26 eV). This bandgap energy is theoretically sufficient to drive the combined reduction of CO₂ together with oxidation of water to O₂, provided the positions of the valence and conduction band are properly situated. The width of the bandgap can be finely tuned via the choice of linker or linkage [40, 72]. Furthermore, by building in donor and acceptor units in the COF, the separation and transmission of electron-hole pairs can be promoted [73]. The catalytic efficiency can be further increased by incorporating units that strongly absorb light. As crystallinity improves charge carrier transport [74], most COFs for photocatalytic CO₂RR are based on linkage types that are easy to crystallize, mainly imine COFs. Recent research has however shown that switching to other, more conjugated linkage types can drastically improve photocatalytic performance [12, 75]. Contrary to electrochemical CO₂ reduction, many photocatalytic CO₂ reductions are done with entirely metal-free COFs, where heteroatoms like nitrogen or sulfur act as the active sites [42]. An overview of some of the best performing COFs for photochemical CO₂-reduction is shown in **Table 1.3**.

Photochemical CO₂RR with COFs shows much promise as it can be performed at ambient pressure and temperature, and in many cases requires only visible light to work, which could even be supplied directly by the sun. However, much reported articles still rely on the use of expensive noble-metal based photosensitizers (e.g. [Ru(bpy)₃]Cl₂) to accelerate the reaction rate, or sacrificial reagents to drive the oxidation reaction (e.g. tri-ethanolamine). This hampers realistic application of these materials on a large scale.

Hydrogenation of CO₂

Hydrogenation of CO₂ involves reacting CO₂ directly with hydrogen gas. Possible endproducts are CO (the reverse water–gas shift reaction), methane (the Sabatier reaction) or methanol. The hydrogen gas necessary for the reaction can be obtained in a sustainable way via electrolysis of water with renewable energy. Contrary to the two previous conversion methods, CO₂ hydrogenation is a much more mature technology: in Iceland for example, a plant has been running since 2012, producing around 4000 tonnes of methanol from CO₂ and H₂ per year [76]. The energy necessary to break the C=O bond is supplied in this process as heat. Since the C=O bond is very stable, high reaction temperatures (200-300° C) and high pressures (50 - 100 bar) are required to drive the reaction. The literature on COFs for hydrogenation of CO₂ is a lot scarcer than for the previously mentioned methods, likely due to the harsher reaction conditions and the need for high-pressure equipment, which is rarely available in a common synthesis lab. The reported COFs are based on triazine, imine, azine and β -ketoenamine linkages, and were decorated with either Ir(III) or Ru(III) (**Table 1.4**). The usually reported metric to compare the activity of the different catalysts is the turnover frequency (TOF).

Material	TOF (h ⁻¹)	Main product	Selectivity	Reference
Ru10% TFB-Hz	243	HCOO ⁻	100 %	[77]
Ir _{0.68} -NHC-CTF	16000	HCOO ⁻	100 %	[78]
IrCp(HBF-2)Cl ₂	1500	HCOO ⁻	100 %	[79]

Table 1.4. Overview of some of the best performing COFs for CO₂ conversion by hydrogenation

1.3 Challenges

Despite all the promising results already reported in literature, COFs have yet to make an industrial breakthrough, not just for applications in CCU, but for any application for that manner. Indeed, despite the intense research interest, there are as of yet no large companies commercially producing COFs for industrial applications. The closely related metal-organic frameworks (MOFs) did make an industrial breakthrough: as mentioned in **subsection 1.2.2**, BASF is producing several hundred tons of CALF-20 per year as of 2023 [45]. We believe this difference in industrial advance has several reasons, including: scalability, generalizability and pore collapse.

Scalability

The only company currently producing COFs on a large scale is YOCOF Material, a small Chinese firm founded in 2023 by prof. Zhang Zhenjie from Nankai University. The company relies for this on the melt synthesis procedure developed earlier in the research group of prof. Zhenjie. This method uses a flux of molten benzoic anhydride at 180 °C to produce crystalline vinylene-linked COFs, or molten benzoic acid at 200-250 °C to produce imide-linked COFs on gram-scale [80, 81]. Both of these methods are capable of producing COFs on kilogram scale. As mentioned in **subsection 1.1.2**, a relatively general strategy for the synthesis of crystalline CTFs on a kilogram-scale based on the use of

H₆P₄O₁₃ as solvent and catalyst was reported in 2022. [21]. The group of Banerjee et al have made several reports on the scalable, solvent-free synthesis of β -ketoenamine COFs, using *p*-toluenesulfonic acid as catalyst. Their process could be successfully scaled to the multi-gram scale, and the resultant materials exhibited high porosity [82, 83]. However, this study focused solely on β -ketoenamine COFs, starting from 1,3,5-triformylphloroglucinol as the aldehyde monomer.

Counter-intuitively, for imine-linked COFs, there exists no general, scalable synthesis method, despite this linkage being far easier to crystallize, and far more studied in literature than the above mentioned linkages. A typical imine COF synthesis is performed solvothermally on milligram-scale at 120 °C for 72 hours or longer. To prevent possible oxidation of monomers under these harsh conditions, the solvent is thoroughly degassed by freeze-pump-thawing, usually in glass ampoules which are then flame-sealed before heating [84]. Common solvents are combinations of 1,4-dioxane, mesitylene, *n*-butanol, *o*-dichlorobenzene and *N,N*-dimethylacetamide. With the exception of *n*-butanol, these solvents are all relatively expensive and pose a health hazard. This requirement of pressurized vessels, thorough degassing and expensive solvents makes it difficult to scale COFs to industrially relevant levels. As a result of these factors, reports on gram-scale synthesis of imine-linked COFs are quite scarce [85–89].

Generalizability

Another roadblock for industrialization of COFs is the lack of generalizability of COF synthesis, in particular again for imine COFs. Each combination of monomers typically requires a distinct solvent combination to yield a COF of optimal quality. A solvent combination that works for one COF, might give a completely amorphous material for another COF. The synthesis of new imine COF is mostly done by trial-and-error: starting from a set of solvent combinations that are known to work in several cases

(e.g. dioxane:mesitylene 4:1 or o-dichlorobenzene:n-butanol 7:3) a lot of different tests are done until a COF of sufficient crystallinity is obtained. This tedious optimization process slows down the development of new COFs.

Pore collapse

In order to obtain a usable porous COF structure, activation is required to remove the reaction solvent, oligomers and unreacted monomers after synthesis. Typically, this is done by washing with several solvents, followed by vacuum drying. During this last step, the evaporation of the solvent can exert significant capillary forces on the pores. In some cases this can lead to pore collapse: a structural distortion of the pores or mismatch between the COF nanosheet layers. This leads to a severe loss of crystallinity and porosity of the material. The process of pore collapse had already been observed in other porous materials, like MOFs, but has only been understood properly in COFs since a few years.

Whether or not pore collapse will occur during activation depends for one part on the nature of the COF. In general, stronger interlayer interactions between the COF nanosheets of 2D COFs tends to make them less prone to pore collapse. Zhu et al. made an empirical study in 2022 and formulated three main factors that influence the tendency of a COF to undergo pore collapse [90]: pore size, pore functionality and pore architecture. COFs with a smaller pore size tend to be more robust, i.e. more resilient to pore collapse. Introducing functionalities on the pore walls, like methoxy or bromide groups also increases the COF robustness. Finally, the shape of the pores is also of importance: COFs with hexagonal pores were found to be more fragile (i.e. more prone to pore collapse) than COFs with rhombic pores [91].

Besides on the COF itself, the degree of pore collapse also depends on the capillary forces exerted by the solvent inside the pores during solvent evaporation. In order to mitigate the effect of pore collapse, activation

must be done with a low-surface tension solvent, which is referred to in COF literature as 'mild activation'. An ideal solvent for mild activation is supercritical CO₂ (scCO₂), which has zero surface tension. Furthermore, it has low viscosity, and is nontoxic, nonflammable and noncorrosive. Unfortunately, scCO₂ can only exist above the critical temperature (~31 °C) and critical pressure (~ 73.8 bar) of CO₂. The high supercritical pressure requires specialized equipment to produce and handle scCO₂. Alternatively, there are organic solvents with a very low surface tension that also minimize pore collapse. Zhu et al. showed that washing with hexane and perfluorohexane ($\gamma = 18.43 \text{ mN}^{-1}$ and $\gamma = 11.91 \text{ mN m}^{-1}$ at 20 °C respectively) followed by vacuum activation, allowed even the most fragile of COFs to be obtained with porosity and crystallinity very similar to that obtained by activation with scCO₂ [92].

From the combined works of Feriante et al. and Smith et al., we could extrapolate that COF robustness is not only dependent on the monomer, but also on the synthesis time [91, 93]. For the same COF, with harsh vacuum activation, very poor crystallinity and porosity were observed after 24 hours of reaction ($S^{\text{BET}} = 124 \text{ m}^2 \text{ g}^{-1}$). After 72 hours with harsh activation, the COF showed moderate crystallinity and porosity ($S^{\text{BET}} = 610 \text{ m}^2 \text{ g}^{-1}$). In the other study, after 4 hours with mild activation with scCO₂, the same COF was obtained as a crystalline and highly porous material ($S_{\text{BET}} = 2480 \text{ m}^2 \text{ g}^{-1}$), showing that the COF is fragile, and the loss of crystallinity in the reports of Smith et al. is the result of pore collapse. This implies that the COF becomes more robust as the synthesis time is prolonged.

While the use of these specialized solvents is effectively able to remediate the effects of pore collapse, this would require extra solvent consumption and washing time after every recycling step. A better solution would be to avoid pore collapse altogether, by synthesizing robust COFs from the start. A more in-depth understanding of pore collapse and the factors determining fragility during COF synthesis are crucial to achieve this.

1.4 Thesis outline

In the above, we have introduced COFs, how they can be used for CCU, and the challenges associated with their synthesis. In what follows, we will aim to address some of the problems with the synthesis of imine COFs, and improve the application potential for COFs in general for the sorption and conversion of CO₂. Rather than only making new materials, we try in this work to develop more general methods that can be broadly applied on entire classes of COFs.

In **chapter 1**, we try to tackle the existing issues of imine COF synthesis. We attempt to develop a new method that is both general and scalable, allowing synthesis of COFs on a multigram-scale. Ideally, this method should be convenient to use in both the lab and in industry, and require no specialized equipment. We also strive to simplify the mild activation process required for the work-up of fragile COFs. Furthermore, the dependency of imine COF synthesis on the nature of the COF solvent is poorly understood. With this study, we also set out to gain more understanding in the complex interplay of COF growth, stacking and robustness.

In **chapter 2**, we use the method developed in **chapter 1** to create a COF for CO₂ sorption. Rather than using specific linkers with high affinity for CO₂, we propose linkage modification as a broadly applicable strategy to improve the CO₂ sorption capacity of covalent organic frameworks. We convert a nitrogen-rich imine-linked COF to a thiazole-linked COF, and examine the CO₂ uptake before and after conversion.

Finally, in **chapter 3**, the focus lies on electrochemical conversion of CO₂ with ionothermally synthesized covalent triazine frameworks. Due to their high nitrogen content and the presence of defects, these materials are promising metal-free electrocatalysts. However, the low conductivity of CTFs poses an issue. We introduce a new way to overcome this, by growing CTF layers *in situ* onto premodified highly conductive multi-walled carbon nanotubes. After in-depth characterization of the new

hybrid materials, we test their activity and selectivity for electrochemical CO₂ reduction.

References

1. Wang, X., Han, X., Cheng, C., *et al.* 2D covalent organic frameworks with cem topology. *Journal of the American Chemical Society* **144**, 7366–7373 (2022).
2. Zou, L., Yang, X., Yuan, S. & Zhou, H.-C. Flexible monomer-based covalent organic frameworks: design, structure and functions. *CrysiEngComm* **19**, 4868–4871 (2017).
3. Liu, C., Wang, Z., Zhang, L. & Dong, Z. Soft 2D covalent organic framework with compacted honeycomb topology. *Journal of the American Chemical Society* **144**, 18784–18789 (2022).
4. Xu, T., Wang, Z., Zhang, W., *et al.* Constructing Photocatalytic Covalent Organic Frameworks with Aliphatic Linkers. *Journal of the American Chemical Society* (2024).
5. Zhu, D., Zhu, Y., Chen, Y., *et al.* Three-dimensional covalent organic frameworks with pto and mhq-z topologies based on Tri- and tetratopic linkers. *Nature Communications* **14**, 2865 (2023).
6. Nguyen, H. L., Gropp, C., Ma, Y., Zhu, C. & Yaghi, O. M. 3D covalent organic frameworks selectively crystallized through conformational design. *Journal of the American Chemical Society* **142**, 20335–20339 (2020).
7. Chen, H., Liu, W., Laemont, A., *et al.* A visible-light-harvesting covalent organic framework bearing single nickel sites as a highly efficient sulfur–carbon cross-coupling dual catalyst. *Angewandte Chemie* **133**, 10915–10922 (2021).
8. Waller, P. J., AlFaraj, Y. S., Diercks, C. S., Jarenwattananon, N. N. & Yaghi, O. M. Conversion of imine to oxazole and thiazole linkages in covalent organic frameworks. *Journal of the American Chemical Society* **140**, 9099–9103 (2018).

9. Haase, F., Troschke, E., Savasci, G., *et al.* Topochemical conversion of an imine-into a thiazole-linked covalent organic framework enabling real structure analysis. *Nature communications* **9**, 2600 (2018).
10. Yan, R., Mishra, B., Traxler, M., *et al.* A Thiazole-linked Covalent Organic Framework for Lithium-Sulphur Batteries. *Angewandte Chemie International Edition* **62**, e202302276 (2023).
11. Singh, V., Kim, J., Kang, B., *et al.* Thiazole-linked covalent organic framework promoting fast two-electron transfer for lithium-organic batteries. *Advanced Energy Materials* **11**, 2003735 (2021).
12. Deng, M., Sun, J., Laemont, A., *et al.* Extending the π -conjugation system of covalent organic frameworks for more efficient photocatalytic H₂O₂ production. *Green Chemistry* **25**, 3069–3076 (2023).
13. Wang, K., Jia, Z., Bai, Y., *et al.* Synthesis of stable thiazole-linked covalent organic frameworks via a multicomponent reaction. *Journal of the American Chemical Society* **142**, 11131–11138 (2020).
14. Kuhn, P., Antonietti, M. & Thomas, A. Porous, covalent triazine-based frameworks prepared by ionothermal synthesis. *Angewandte Chemie International Edition* **47**, 3450–3453 (2008).
15. Ren, S., Bojdys, M. J., Dawson, R., *et al.* Porous, fluorescent, covalent triazine-based frameworks via room-temperature and microwave-assisted synthesis. *Adv. Mater* **24**, 2357–2361 (2012).
16. Wang, K., Yang, L.-M., Wang, X., *et al.* Covalent triazine frameworks via a low-temperature polycondensation approach. *Angewandte Chemie International Edition* **56**, 14149–14153 (2017).
17. Liu, M., Jiang, K., Ding, X., *et al.* Controlling monomer feeding rate to achieve highly crystalline covalent triazine frameworks. *Advanced Materials* **31**, 1807865 (2019).
18. Liu, M., Huang, Q., Wang, S., *et al.* Crystalline covalent triazine frameworks by in situ oxidation of alcohols to aldehyde monomers. *Angewandte Chemie International Edition* **57**, 11968–11972 (2018).

19. Guo, L., Wang, X., Zhan, Z., *et al.* Crystallization of covalent triazine frameworks via a heterogeneous nucleation approach for efficient photocatalytic applications. *Chemistry of Materials* **33**, 1994–2003 (2021).
20. Sun, T., Liang, Y. & Xu, Y. Rapid, ordered polymerization of crystalline semiconducting covalent triazine frameworks. *Angewandte Chemie International Edition* **61**, e202113926 (2022).
21. Sun, T., Liang, Y., Luo, W., *et al.* A General Strategy for Kilogram-Scale Preparation of Highly Crystalline Covalent Triazine Frameworks. *Angewandte Chemie* **134**, e202203327 (2022).
22. Mo, Y.-P., Liu, X.-H. & Wang, D. Concentration-directed polymorphic surface covalent organic frameworks: Rhombus, parallelogram, and kagome. *ACS nano* **11**, 11694–11700 (2017).
23. Liang, R.-R., Cui, F.-Z., Qi, Q.-Y. & Zhao, X. A study on constitutional isomerism in covalent organic frameworks: Controllable synthesis, transformation, and distinct difference in properties. *CCS Chemistry* **2**, 139–145 (2020).
24. Li, Y., Guo, L., Lv, Y., *et al.* Polymorphism of 2D imine covalent organic frameworks. *Angewandte Chemie* **133**, 5423–5429 (2021).
25. Lin, G., Ding, H., Yuan, D., Wang, B. & Wang, C. A pyrene-based, fluorescent three-dimensional covalent organic framework. *Journal of the American Chemical Society* **138**, 3302–3305 (2016).
26. Gui, B., Xin, J., Cheng, Y., *et al.* Crystallization of dimensional isomers in covalent organic frameworks. *Journal of the American Chemical Society* **145**, 11276–11281 (2023).
27. Li, Y., Wu, Q., Guo, X., *et al.* Laminated self-standing covalent organic framework membrane with uniformly distributed subnanopores for ionic and molecular sieving. *Nature communications* **11**, 599 (2020).

28. Mu, Z., Zhu, Y., Li, B., *et al.* Covalent organic frameworks with record pore apertures. *Journal of the American Chemical Society* **144**, 5145–5154 (2022).
29. Zhao, Y., Das, S., Sekine, T., *et al.* Record ultralarge-pores, low density three-dimensional covalent organic framework for controlled drug delivery. *Angewandte Chemie International Edition* **62**, e202300172 (2023).
30. El-Kaderi, H. M., Hunt, J. R., Mendoza-Cortés, J. L., *et al.* Designed synthesis of 3D covalent organic frameworks. *Science* **316**, 268–272 (2007).
31. Wang, Z., Zhang, S., Chen, Y., Zhang, Z. & Ma, S. Covalent organic frameworks for separation applications. *Chemical Society Reviews* **49**, 708–735 (2020).
32. Cui, W.-R., Li, F.-F., Xu, R.-H., *et al.* Regenerable covalent organic frameworks for photo-enhanced uranium adsorption from seawater. *Angewandte Chemie* **132**, 17837–17843 (2020).
33. Qian, H.-L., Meng, F.-L., Yang, C.-X. & Yan, X.-P. Irreversible amide-linked covalent organic framework for selective and ultrafast gold recovery. *Angewandte Chemie International Edition* **59**, 17607–17613 (2020).
34. Wang, W., Jia, Y., Zhou, S. & Deng, S. Removal of typical PFAS from water by covalent organic frameworks with different pore sizes. *Journal of Hazardous Materials* **460**, 132522 (2023).
35. Bian, Y., Song, X., Han, Y., Wang, G. & Qiao, H. Carboxyl functionalized covalent organic framework material for selective adsorption of methylene blue in aqueous solutions. *Tetrahedron Letters*, 155281 (2024).
36. Yuxuan, C., Qi, C. & Zhanhui, Z. Application of covalent organic framework materials as heterogeneous ligands in organic synthesis. *Chinese Journal of Organic Chemistry* **41**, 3826 (2021).

37. Kaur, G. & Kumar, P. Ibuprofen tagged imine RT-COF-1 as customisable vehicle for controlled drug delivery application. *Inorganic Chemistry Communications* **145**, 110043 (2022).
38. Haug, W. K., Moscarello, E. M., Wolfson, E. R. & McGrier, P. L. The luminescent and photophysical properties of covalent organic frameworks. *Chemical Society Reviews* **49**, 839–864 (2020).
39. Yang, Q., Luo, M., Liu, K., Cao, H. & Yan, H. Covalent organic frameworks for photocatalytic applications. *Applied Catalysis B: Environmental* **276**, 119174 (2020).
40. Chen, Y., Luo, X., Zhang, J., *et al.* Bandgap engineering of covalent organic frameworks for boosting photocatalytic hydrogen evolution from water. *Journal of Materials Chemistry A* **10**, 24620–24627 (2022).
41. Krishnaraj, C., Sekhar Jena, H., Bourda, L., *et al.* Strongly reducing (diaryl-amino) benzene-based covalent organic framework for metal-free visible light photocatalytic H₂O₂ generation. *Journal of the American Chemical Society* **142**, 20107–20116 (2020).
42. Nguyen, H. L. & Alzamy, A. Covalent organic frameworks as emerging platforms for CO₂ photoreduction. *ACS Catalysis* **11**, 9809–9824 (2021).
43. Lee, H. & (eds.), J. R. *Summary for Policymakers. In: Climate Change 2023: Synthesis Report. Contribution of Working Groups I, II and III to the Sixth Assessment Report of the Intergovernmental Panel on Climate Change* tech. rep. (IPCC, 2023).
44. Dziejarski, B., Serafin, J., Andersson, K. & Krzyżyńska, R. CO₂ capture materials: a review of current trends and future challenges. *Materials Today Sustainability*, 100483 (2023).
45. Hoffmann, K. *BASF becomes first company to successfully produce metal organic frameworks on a commercial scale for carbon capture* <https://www.basf.com/global/documents/en/news-and->

- media/news-releases/2023/10/P327e_MOFs_Svante.pdf [Accessed: (14/05/2024)]. 2023.
46. Nitta, C. *Svante Secures Commercial Supply of MOF* <https://www.svanteinc.com/press-releases/svante-secures-commercial-supply-of-mof-advanced-sorbent-materials-with-basf-for-carbon-capture-market/> [Accessed: (25/05/2024)]. 2023.
 47. Pan, H., Yu, C., Suo, X., *et al.* Emerging porous materials for carbon dioxide adsorptive capture: progress and challenges. *Materials Chemistry Frontiers* (2023).
 48. Hauchhum, L. & Mahanta, P. Carbon dioxide adsorption on zeolites and activated carbon by pressure swing adsorption in a fixed bed. *International Journal of Energy and Environmental Engineering* **5**, 349–356 (2014).
 49. Liang, Z., Marshall, M. & Chaffee, A. L. CO₂ adsorption-based separation by metal organic framework (Cu-BTC) versus zeolite (13X). *Energy & Fuels* **23**, 2785–2789 (2009).
 50. Ji, C., Su, K., Wang, W., *et al.* Tunable cage-based three-dimensional covalent organic frameworks. *CCS Chemistry* **4**, 3095–3105 (2022).
 51. Huang, N., Wang, P., Addicoat, M. A., Heine, T. & Jiang, D. Ionic covalent organic frameworks: design of a charged interface aligned on 1D channel walls and its unusual electrostatic functions. *Angewandte Chemie* **129**, 5064–5068 (2017).
 52. Das, N., Paul, R., Chatterjee, R., *et al.* Tuning of Microenvironment in Covalent Organic Framework via Fluorination Strategy promotes Selective CO₂ Capture. *Chemistry–An Asian Journal* **18**, e202200970 (2023).
 53. Mukherjee, S., Das, M., Manna, A., Krishna, R. & Das, S. Newly designed 1, 2, 3-triazole functionalized covalent triazine frameworks with exceptionally high uptake capacity for both CO₂ and H₂. *Journal of Materials Chemistry A* **7**, 1055–1068 (2019).

54. Sun, R., Wang, X., Wang, X. & Tan, B. Three-Dimensional Crystalline Covalent Triazine Frameworks via a Polycondensation Approach. *Angewandte Chemie International Edition* **61**, e202117668 (2022).
55. Li, H., Dilipkumar, A., Abubakar, S. & Zhao, D. Covalent organic frameworks for CO₂ capture: from laboratory curiosity to industry implementation. *Chemical Society Reviews* **52**, 6294–6329 (2023).
56. Guan, X., Li, H., Ma, Y., *et al.* Chemically stable polyarylether-based covalent organic frameworks. *Nature chemistry* **11**, 587–594 (2019).
57. Lu, C., Yang, J., Wei, S., *et al.* Atomic Ni anchored covalent triazine framework as high efficient electrocatalyst for carbon dioxide conversion. *Advanced Functional Materials* **29**, 1806884 (2019).
58. Dong, H., Lu, M., Wang, Y., *et al.* Covalently anchoring covalent organic framework on carbon nanotubes for highly efficient electrocatalytic CO₂ reduction. *Applied Catalysis B: Environmental* **303**, 120897 (2022).
59. Wang, Y., Chen, J., Wang, G., Li, Y. & Wen, Z. Perfluorinated covalent triazine framework derived hybrids for the highly selective electroconversion of carbon dioxide into methane. *Angewandte Chemie International Edition* **57**, 13120–13124 (2018).
60. Wang, Y.-R., Ding, H.-M., Ma, X.-Y., *et al.* Imparting CO₂ Electrorreduction Auxiliary for Integrated Morphology Tuning and Performance Boosting in a Porphyrin-based Covalent Organic Framework. *Angewandte Chemie International Edition* **61**, e202114648 (2022).
61. Ali, S., Iqbal, R., Wahid, E., *et al.* Cobalt coordinated two-dimensional covalent organic framework a sustainable and robust electrocatalyst for selective CO₂ electrochemical conversion to formic acid. *Fuel Processing Technology* **237**, 107451 (2022).
62. Xiao, Y., Lu, J., Chen, K., *et al.* Linkage Engineering in Covalent Organic Frameworks for Metal-Free Electrocatalytic C₂H₄ Production from CO₂. *Angewandte Chemie*, e202404738 (2024).

63. Qiu, X.-F., Huang, J.-R., Yu, C., *et al.* A stable and conductive covalent organic framework with isolated active sites for highly selective electroreduction of carbon dioxide to acetate. *Angewandte Chemie* **134**, e202206470 (2022).
64. Wang, J., Hu, H., Lu, S., *et al.* Conductive metal and covalent organic frameworks for electrocatalysis: design principles, recent progress and perspective. *Nanoscale* **14**, 277–288 (2022).
65. Bhosale, A. A., Payne, K. & Zhang, X. *Numerical Study of Superconducting, Low Temperature and Room Temperature RF Coils at Ultra-Low Field 70mT/3MHz MRI in Proceedings of the International Society for Magnetic Resonance in Medicine... Scientific Meeting and Exhibition. International Society for Magnetic Resonance in Medicine. Scientific Meeting and Exhibition* **32** (2024).
66. Yu, X., Gong, K., Tian, S., *et al.* A hydrophilic fully conjugated covalent organic framework for photocatalytic CO₂ reduction to CO nearly 100% using pure water. *Journal of Materials Chemistry A* **11**, 5627–5635 (2023).
67. Liu, W., Li, X., Wang, C., *et al.* A scalable general synthetic approach toward ultrathin imine-linked two-dimensional covalent organic framework nanosheets for photocatalytic CO₂ reduction. *Journal of the American Chemical Society* **141**, 17431–17440 (2019).
68. Dong, M., Pan, Q., Meng, F., *et al.* Trinuclear Cu-based covalent organic framework: π -conjugated framework regulating electron delocalization to promote photoreduction CO₂. *Journal of Colloid and Interface Science* **662**, 807–813 (2024).
69. Kaya, K., Ditz, D., Jaworski, A., *et al.* Enhanced solar CO₂ photoreduction to formic acid by platinum immobilization on bipyridine covalent triazine framework with defects. *Advanced Sustainable Systems* **7**, 2300071 (2023).

70. Kou, M., Liu, W., Wang, Y., *et al.* Photocatalytic CO₂ conversion over single-atom MoN₂ sites of covalent organic framework. *Applied Catalysis B: Environmental* **291**, 120146 (2021).
71. Chakraborty, P., Ghosh, S., Das, A., Khan, A. & Islam, S. M. Visible-light-driven sustainable conversion of carbon dioxide to methanol using a metal-free covalent organic framework as a recyclable photocatalyst. *Catalysis Science & Technology* **12**, 3484–3497 (2022).
72. Chen, X.-R., Cui, W.-R., Liang, R.-P., *et al.* Band gap engineering in vinylene-linked covalent organic frameworks for enhanced photocatalytic degradation of organic contaminants and disinfection of bacteria. *ACS Applied Bio Materials* **4**, 6502–6511 (2021).
73. Jin, S., Supur, M., Addicoat, M., *et al.* Creation of superheterojunction polymers via direct polycondensation: segregated and bicontinuous donor–acceptor π -columnar arrays in covalent organic frameworks for long-lived charge separation. *Journal of the American Chemical Society* **137**, 7817–7827 (2015).
74. Zhang, W., Chen, L., Dai, S., *et al.* Reconstructed covalent organic frameworks. *Nature* **604**, 72–79 (2022).
75. Suleman, S., Sun, K., Zhao, Y., *et al.* Enhanced Photocatalytic CO₂ Reduction via Linkage Substitution in Porphyrinic Covalent Organic Frameworks. *CCS Chemistry* **6**, 1689–1697 (2024).
76. Sigurbjornsson, O. *Sustainable Fuels and Chemicals by Carbon Recycling* <https://www.mn.uio.no/smn/english/research/projects/chemistry/236830-electra/Dissemination/Presentation/no22-cri-uni-iceland-guest-lecture-13.11.2015-short.pdf> [Accessed: (14/08/2024)]. 2015.
77. Fellenberg, A. K., Addad, A., Chernyak, S. A., *et al.* Covalent organic frameworks for design of ruthenium catalysts with high single-atom site density for CO₂ hydrogenation into formic acid. *Cell Reports Physical Science* **5** (2024).

78. Gunasekar, G. H., Park, K., Ganesan, V., *et al.* A covalent triazine framework, functionalized with Ir/N-heterocyclic carbene sites, for the efficient hydrogenation of CO₂ to formate. *Chemistry of Materials* **29**, 6740–6748 (2017).
79. Hariyanandam, G. G., Hyun, D., Natarajan, P., Jung, K.-D. & Yoon, S. An effective heterogeneous Ir (III) catalyst, immobilized on a heptazine-based organic framework, for the hydrogenation of CO₂ to formate. *Catalysis Today* **265**, 52–55 (2016).
80. Wang, Z., Zhang, Y., Wang, T., *et al.* Organic flux synthesis of covalent organic frameworks. *Chem* **9**, 2178–2193 (2023).
81. Zhang, P., Wang, Z., Yang, Y., *et al.* Melt polymerization synthesis of a class of robust self-shaped olefin-linked COF foams as high-efficiency separators. *Science China Chemistry* **65**, 1173–1184 (2022).
82. Karak, S., Kandambeth, S., Biswal, B. P., *et al.* Constructing ultra-porous covalent organic frameworks in seconds via an organic terracotta process. *Journal of the American Chemical Society* **139**, 1856–1862 (2017).
83. Biswal, B. P., Chandra, S., Kandambeth, S., *et al.* Mechanochemical synthesis of chemically stable isoreticular covalent organic frameworks. *Journal of the American Chemical Society* **135**, 5328–5331 (2013).
84. Geng, K., He, T., Liu, R., *et al.* Covalent organic frameworks: design, synthesis, and functions. *Chemical reviews* **120**, 8814–8933 (2020).
85. Xu, L., Ding, S.-Y., Liu, J., *et al.* Highly crystalline covalent organic frameworks from flexible building blocks. *Chemical communications* **52**, 4706–4709 (2016).
86. Han, X.-H., Chu, J.-Q., Wang, W.-Z., Qi, Q.-Y. & Zhao, X. A two-step solvothermal procedure to improve crystallinity of covalent organic frameworks and achieve scale-up preparation. *Chinese Chemical Letters* **33**, 2464–2468 (2022).

87. Zhang, Y., Mao, T., Hao, L., *et al.* Solvent-Free Synthesis of C= N Linked Two-Dimensional Covalent Organic Frameworks. *Macromolecular Rapid Communications* **44**, 2200722 (2023).
88. Guo, L., Zhang, Q. Y., Yu, Z., Krishna, R. & Luo, F. Minute and Large-Scale Synthesis of Covalent-Organic Frameworks in Water at Room Temperature by a Two-Step Dissolution–Precipitation Method. *Chemistry of Materials* **35**, 5648–5656 (2023).
89. Tan, F., Zheng, Y., Zhou, Z., *et al.* Aqueous synthesis of covalent organic frameworks as photocatalysts for hydrogen peroxide production. *CCS Chemistry* **4**, 3751–3761 (2022).
90. Zhu, D., Zhang, J.-J., Wu, X., *et al.* Understanding fragility and engineering activation stability in two-dimensional covalent organic frameworks. *Chemical Science* **13**, 9655–9667 (2022).
91. Feriante, C. H., Jhulki, S., Evans, A. M., *et al.* Rapid Synthesis of High Surface Area Imine-Linked 2D Covalent Organic Frameworks by Avoiding Pore Collapse During Isolation. *Advanced Materials* **32**, 1905776 (2020).
92. Zhu, D. & Verduzco, R. Ultralow surface tension solvents enable facile COF activation with reduced pore collapse. *ACS applied materials & interfaces* **12**, 33121–33127 (2020).
93. Smith, B. J., Overholts, A. C., Hwang, N. & Dichtel, W. R. Insight into the crystallization of amorphous imine-linked polymer networks to 2D covalent organic frameworks. *Chemical Communications* **52**, 3690–3693 (2016).

Simplifying Solvothermal Synthesis of Covalent Organic Frameworks

¹ ***Parts of this work have been published in:*** Laemont, A., Matthys, G., Lavendomme, R. & Van Der Voort, P. Mild and Scalable Conditions for the Solvothermal Synthesis of Imine-Linked Covalent Organic Frameworks. *accepted at Angewandte Chemie - International Edition* (2024) .

2.1 Introduction

As explained in **section 1.3**, while relatively general and scalable synthesis methods exist for COF types that are more difficult to crystallize, the synthesis of imine-linked COFs remains a tedious and poorly scalable process of trial-and-error. Therefore, we figured that the first step in this research should be dedicated to the development of a general, scalable and convenient method to synthesize imine COFs.

Sporadic research on developing such methods has already been done in the past in the past. Many of these studies present new catalysts for COF formation, such as transition metal triflates, nitrates or oxides, organic Lewis acids or hydroxide bases [1–5]. While these catalysts can indeed produce certain crystalline COFs, their applicability was only demonstrated for a limited range of monomers: many of the COFs produced with these catalysts were shown to have lower crystallinity and porosity than those made with classical solvothermal synthesis. On top of that, these alternative catalysts are often significantly more expensive than acetic acid. Other reported strategies are (1) the use of monofunctional organic modulators, such as aniline or benzaldehyde, to enhance error correction, (2) the introduction of certain additives, such as Triton X-100 or imidazole, in the reaction mixture (3) prefunctionalization of the monomer, for example by conversion of the monomer amine groups to N-aryl benzophenone imines [6–11]. Besides the problems mentioned above, the methods also give rise to an extra synthetic cost and additional waste.

A relatively recent breakthrough is sonochemical synthesis, discovered by Zhao et al [12]. Using ultrasonication, a range of COFs can be produced at room temperature in aqueous acetic acid. This elegant method requires no heating nor any organic solvents other than ecofriendly acetic acid. However, the sonication power and acetic acid concentration still had to be optimized for each COF. Although the method could produce many COFs in some cases, the yield, crystallinity, or porosity were inferior to

that of their solvothermal counterparts. Furthermore, the method uses an ultrasonication microtip probe, hardware that is rarely available in a common lab and has yet to be employed in industrial chemistry. The authors scaled up the synthesis of one COF to 500 mg. The scaled COF had the same crystallinity and porosity as the small-scale reaction, but the yield dropped by over 20%. In short, there is definitely room for improvement.

2.2 Optimization of imine-linked COF synthesis

The formation of the imine bond relies on the reversible condensation of aldehydes and amines. This is basic organic chemistry which has been known for over a century. The synthesis of imines can occur under very simple conditions in virtually any solvent. A simple Brønsted acid is sufficient to efficiently catalyze the reaction. We therefore chose to use for our optimization green and inexpensive aqueous alcohol solutions as the solvent, and acetic acid as the catalyst, under aerobic conditions. The combination of 1,3,5-tris(4-aminophenyl)benzene (TAPB) and 2,5-dibromoterephthalaldehyde (TaBr₂) yields the COF TAPB–TaBr₂. This COF has been reported to be resilient to pore collapse, which removes the need for mild activation [13]. The COF was synthesized in a simple cap-closed vial under ambient atmosphere. We stirred the reaction to mitigate the effect of differing solubility of the monomers in different solvent mixtures. Five parameters were optimized: the carbon number of the alkyl alcohol (1-10), the reaction time, reaction temperature, and water and acid content of the mixture. The obtained materials were characterized by PXRD and N₂-sorption, and are shown in **Figure 2.1** for n-butanol as the best-performing alcohol and **Figure 2.2** for the alcohol alkyl chain length effect. Synthetic details of the different optimization attempts are given in **Table 2.1**.

Systematic variation of the water content between 0 v% and 80 v% showed an optimum at 10 v% water (**Figure 2.1A, D**). Water allows for the hydroly-

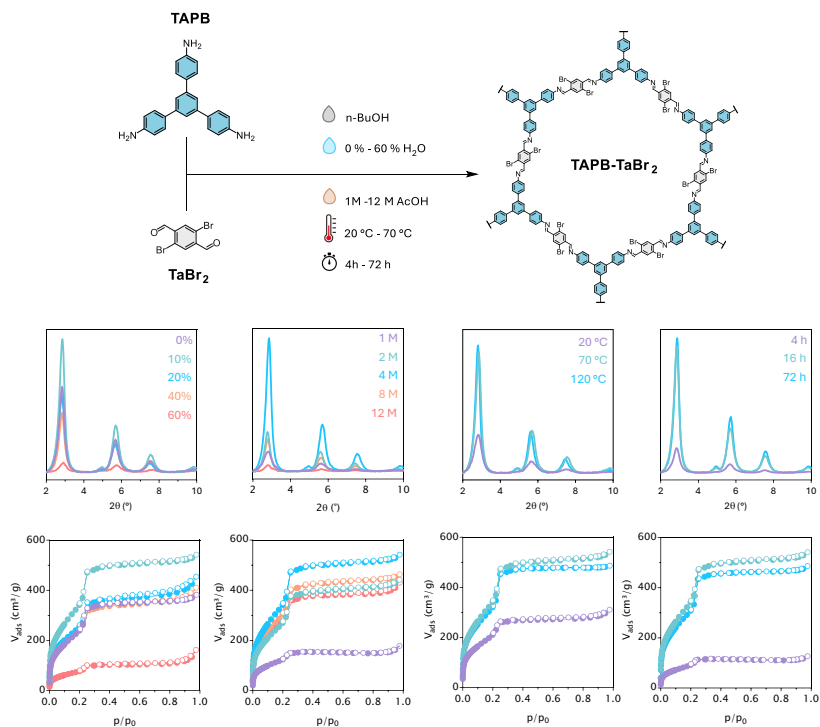


Figure 2.1. PXRD patterns and N_2 -sorption isotherms of TAPB–TaBr₂ COF synthesized in n-BuOH with variation of the water content (A,E), acetic acid content (B,F), reaction time (C,G) and temperature (D,H) from base parameters (10 v% H₂O, 4 M AcOH, 16 h, 70 °C).

sis of formed imine bond and thus improves error correction during COF formation. A too high water content however can drive the imine formation equilibrium towards the reactants, which hampers the formation of an ordered framework.

The acid content of the reaction mixture played a major role in the COF crystallization process (**Figure 2.1B, E**). With an acid content of 1M (based on the total solvent volume), a poorly crystalline and porous material was obtained. The COF quality increases with increasing acetic acid content, up to 4M. This agrees with the well-known fact that acetic

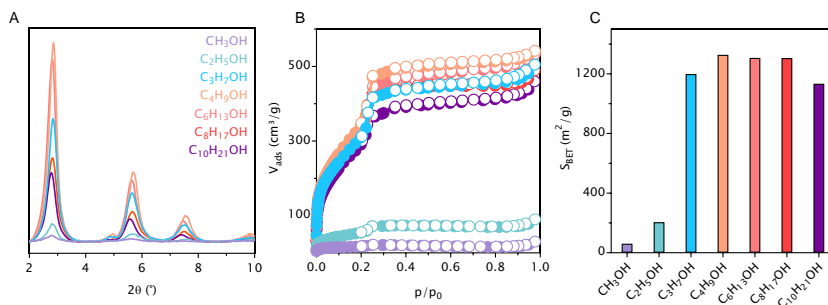


Figure 2.2. The PXRD patterns, N₂-sorption isotherms, and calculated S_{BET} of TAPB-TaBr₂ synthesized using different alkyl alcohols

acid catalyzes the reversible imine bond formation. However, beyond 4M the COF quality started to decrease again.

A COF of excellent quality was already formed after 16 hours of reaction. Increasing the reaction time led only to a minor improvement of crystalline features: the PXRD patterns of TAPB-TaBr₂ synthesized in 16 hours and 72 hours were very similar. However, with only 4 hours reaction time, the material showed significantly lower crystallinity (**Figure 2.1D, H**).

A similar trend was seen for the reaction temperature: synthesis at 70 °C yielded materials of markedly higher quality than those made at 20 °C. Further increase of the temperature to 120 °C only marginally enhanced the COF quality (**Figure 2.1C, G**).

The porosity and crystallinity of TAPB-TaBr₂ increased with increasing carbon number of the alcohol up to four, from a nearly amorphous and nonporous material in methanol, to a high-quality COF in n-butanol with a BET surface area exceeding 1300 m² g⁻¹ (**Figure 2.2C**). Literature synthesis of this COF yielded a material with very similar surface area, but took 3 days at 120 °C in degassed o-dichlorobenzene [14, 15]. Synthesis of TAPB-TaBr₂ in n-hexanol and n-octanol-containing mixtures gave similar results as n-butanol. The mixture of n-decanol, water, and acetic acid was no longer homogeneous, even at 70 °C. We believe this phase separation explains the decrease in COF quality.

2.3 The role of the solvent on the formation of COFs

To rationalize the difference in COF quality between methanol and n-butanol as solvents, we investigated the COF formation *in situ* using Raman spectroscopy over the course of 12 hours (**Figure 2.3A, B**) in mixture of methanol, respectively n-butanol with 10 v% water and 4 M acetic acid. In both cases, the aldehyde C=O stretching vibration of TaBr₂ around 1690 cm⁻¹ and the C-H stretching vibration of TAPB around 1360 cm⁻¹ disappeared within less than 2 minutes. A new intense peak occurred at 1570 cm⁻¹, which we ascribe to the phenyl C=C stretching vibration of the COF network. This peak is accompanied by a smaller C=N stretching vibration at 1616 cm⁻¹, indicative of imine bond formation [16]. Within less than 10 minutes, the measured spectrum was nearly identical to that of the finished and dried COF. In line with this observation, the reaction yield, calculated based on the weight of the COF, reached more than 90% after 10 minutes and hardly increased further (**Figure A.7**). This indicates that polymerization was nearly finished within a few minutes regardless of the solvent. However, over the next hours the overall Raman spectrum increased in intensity in both solvents. A plot of the intensity of the peak at 1570 cm⁻¹ is given in **Figure 2.3C**. The gradual increase in overall Raman intensity is much more outspoken for the reaction in n-butanol than that in methanol.

We found that the cause for this increased intensity finds its origin in a difference in particle growth over time in the two solvents. It has been reported that larger particles give rise to higher Raman intensity [17]. When we correct for the influence of particle size using multiplicative scatter correction (MSC), we found that the Raman intensity for the peak at 1570 cm⁻¹ increased up until around 10 minutes, and then remained constant, in line with the yields of the COF reaction (**Figure A.6, Figure A.7**).

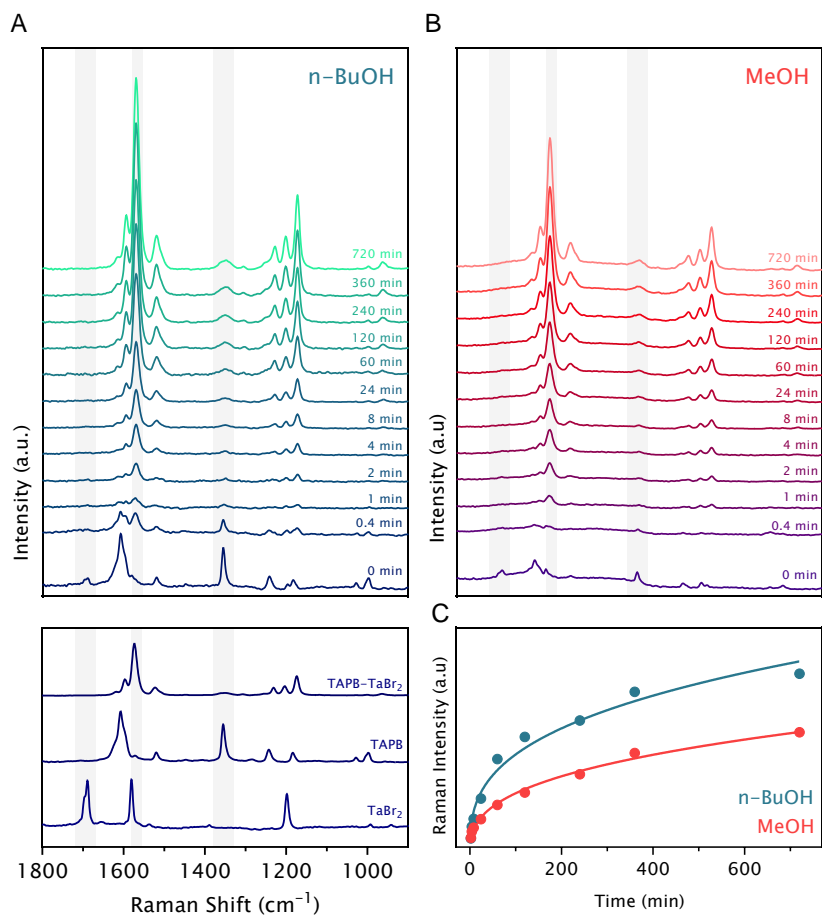


Figure 2.3. Evolution over time of the Raman spectrum of a mixture of TAPB and TaBr₂ in (A) n-butanol and (B) methanol; The intensity of the C=C stretch at 1570 cm⁻¹ over time of the reaction mixture containing n-BuOH (teal) or methanol (red) (C).

To support this hypothesis, we visually observed the aggregation of COF particles with optical microscopy (**Figure 2.4**). During the synthesis process, small aliquots of COF were taken from the vials, and gently pressed between two glass slides while still soaked with solvent. The images show clearly that in n-butanol, the COF particles aggregate over time to form larger particles. The average size of the COF aggregates is

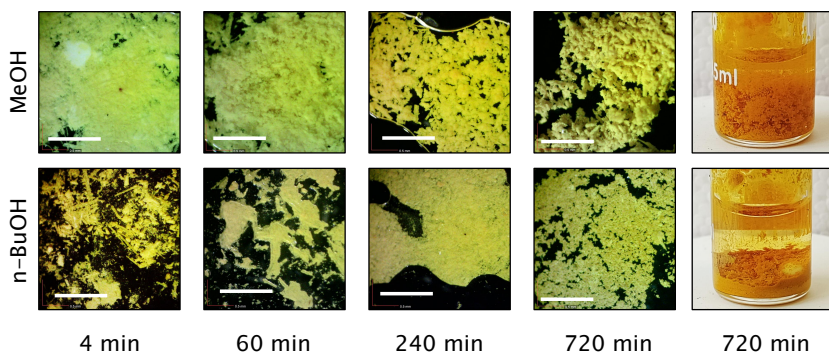


Figure 2.4. Optical microscopy images and photographs of TAPB-TaBr₂ during synthesis in n-butanol (left) or methanol (right) at different points in time. The white bar is 1 mm.

much smaller in methanol at any given point in time. SEM images of the COF particles after reaction, washing and drying confirm the same trend (**Figure A.9, Figure A.8**). The difference in morphology could even be observed with the naked eye at the end of the reaction. The reaction in methanol yielded a dense, sand-like powder resting at the bottom the vial, while in n-butanol we saw a voluminous fluffy powder which somewhat floated in the solvent.

We furthermore investigated the changes in the FTIR-spectra of the COFs over time. Small aliquots were taken from the reaction at four points in time and thoroughly filtered, washed and dried before measurement, to assure all unreacted monomers were removed. Notably, the peaks at 3355 and 3205 cm⁻¹, 1517 cm⁻¹ and 1282 cm⁻¹ decrease in intensity as the reaction time progresses (**Figure 2.5**). We hypothesize these peaks originate respectively from the N-H stretching vibrations, C-H rocking vibration and the C-N stretching vibrations of terminal TAPB-moieties located at the edge of a COF nanosheet, where one or two of the amine groups are still present. With n-butanol as a reaction solvent, these peaks diminish quickly over time and have almost completely disappeared after

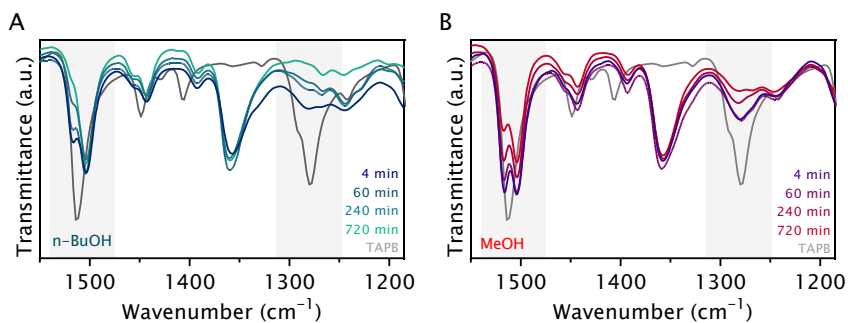
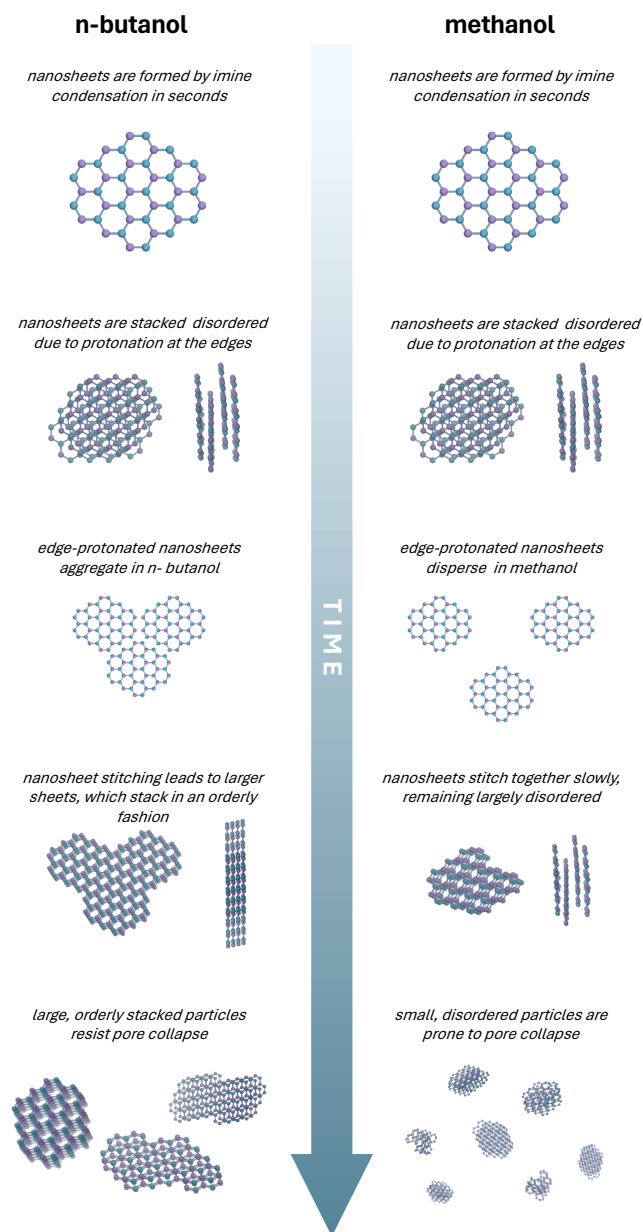


Figure 2.5. FTIR spectra of the washed and dried TAPB-TaBr₂ synthesised in reaction mixtures with n-butanol (A) or methanol (B)

12 hours. In methanol the peak intensity decreases much slower, and all four peaks are still well visible even after 12 hours of reaction.

From these combined observations, we propose a possible explanation for the divergent COF formation in the two solvents, building on the mechanism proposed by Feriante et al. (**Figure 2.6**) [18]. Due to the magnetic stirring, the monomers are quickly distributed evenly over the solvent. The presence of a large amount of catalytic acid allows for fast, near complete formation of COF nanosheets via imine condensation. The newly formed nanosheets are protonated at the edges, as a result of the dynamic imine condensation equilibrium with the surrounding acidic environment. These positive charges repel one another and in this way disrupt the ordered stacking of the COF nanosheets [18]. This is consistent with the observation that at higher acetic acid concentrations the crystallinity of the resultant COF decreased (**Figure 2.1B**). Due to the apolar butyl group, these edge-protonated nanosheets will tend to clump together in n-butanol. The close proximity of nanosheets stimulates them to stitch together. By this we mean that terminal aldehyde and amine groups on the edges of the nanosheets react with each other to form a larger nanosheet. The now larger nanosheets have a lower ratio of protonated edges to total surface area, which reduces the overall repulsion between the sheets and thus increases their tendency to stack



TIME

Figure 2.6. Proposed mechanism for the synthesis of COFs in a mixture containing n-butanol (left), or methanol (right)

in an ordered fashion. In the more polar methanol-containing mixture, the protonated nanosheets are more effectively dispersed and therefore less prone to aggregation. This results in the COF nanosheets stitching together slower over time. The smaller particles have a higher edge to surface ratio, and thus more protonated sites per nanosheets surface, counteracting the ordered stacking of the nanosheets. Such smaller particles as a result should have more exposed edges which contain unreacted terminal aldehyde and amine groups, as we indeed observed from FTIR-spectroscopy (**Figure 2.3D**). We could further confirm this mechanism with observations from transmission electron microscopy (TEM) measurements. In both methanol and n-butanol, COF nanosheets can be seen. However, the nanosheets in n-butanol are much larger than the sheets in methanol (**Figure A.10, Figure A.11**).

The difference in particle size and consequently ordered stacking has a pronounced effect on the robustness of the COF. Feriante et al. discovered that properly stacked COFs are more resilient to pore collapse [19]. We could confirm these findings by stopping the synthesis in n-butanol at 70 °C after one hour, and mildly activating the COF with a low surface tension solvent to prevent possible pore collapse (**Figure 2.7A**). The resulting material was highly crystalline even after 1 hour, while we previously found that the same COF synthesized in 4 hours with vacuum activation was only weakly crystalline (**Figure 2.1D**). In methanol, TAPB-TaBr₂ synthesized in one hour yielded a material of poor quality even with mild activation. After 16 hours, a similarly poorly crystalline material was obtained after vacuum activation, but mild activation gave a COF of high crystallinity (**Figure 2.7A**). Previous reports have already described how the robustness of a COF depends on pore size, architecture and functionality and synthesis time [13, 19]. We can now add that the right solvent is also crucial to promote robustness: faster stitching in n-butanol compared to methanol leads to far more robust Ta-TaBr₂ particles.

We have now established that alcohols with a long apolar linear alkyl chain, but still miscible with aqueous acetic acid are optimal to promote the growth of TAPB-TaBr₂. Control experiments were done to see if the same effect can be achieved using other solvents. We tried benzyl alcohol and benzonitrile with 10 v% water and 4M acetic acid, and obtained highly crystalline TAPB-TaBr₂ in both cases (**Figure 2.7B**). Alcohols and nitriles allow here for miscibility via hydrogen bonding, while the apolar benzyl group promotes COF stitching. Both the apolar group and the miscibility are necessary: synthesis in mixtures with the very polar N-methylpyrrolidone (NMP) yielded a nearly amorphous polymer. The other extreme, a stirred emulsion with apolar n-hexane gave a COF of poor crystallinity as well (**Figure 2.7B**).

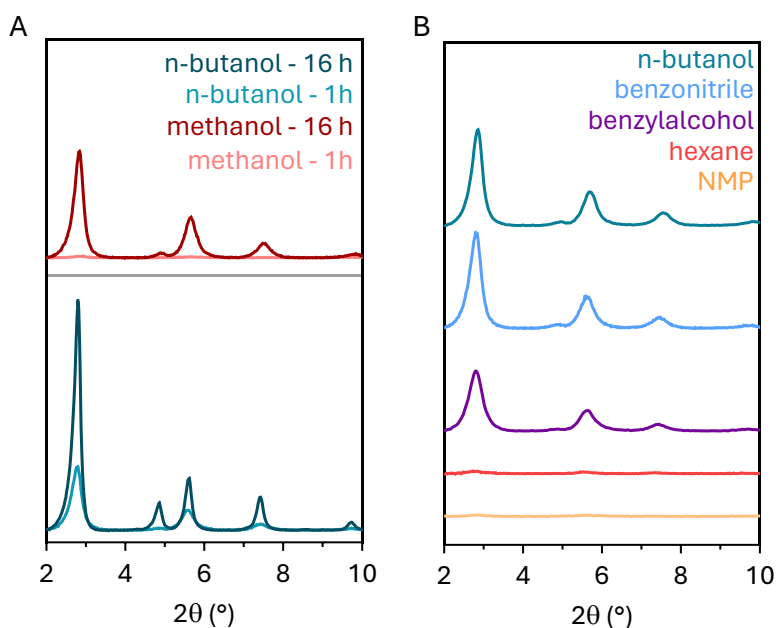


Figure 2.7. Synthesis of TAPB-TaBr₂ with mild activation, showing the influence of reaction time and solvent on the robustness of the COF (A); TAPB-TaBr₂ synthesized in mixtures of n-butanol, benzonitrile, benzylalcohol, hexane or N-methylpyrrolidone with 10 v% water and 4M acetic acid (B).

2.4 General green synthesis of imine-linked COFs

Using this set of reaction conditions, we synthesized an additional 11 COFs. We performed the reactions at 70 °C in n-butanol with 10v% H₂O and 4M AcOH. We chose n-butanol because it is a cheap commodity chemical, which can be produced from biomass [20]. The reactions were done for 16 hours, to give the COF particles more time to grow and become less prone to pore collapse. For every COF, the Pawley refined PXRD pattern corresponded well to the theoretical structure (**Figure A.2**). Successful formation was also confirmed by FTIR, which showed the presence of the imine stretching vibration around 1600-1620 cm⁻¹, and by N₂-sorption (**Figure A.3**, **Figure A.4**). The BET plots, surface area's and values for *C*, *R*² and *V_m* are shown in **Figure A.5** and **Table A.2**. Both variations in the aldehyde and amine linkers gave COFs with excellent crystallinity. The method proved to be successful for the synthesis of COFs of different topology, such as [3+3] and [4+2] combinations (**Figure 2.8E, G, H, I, J, K**). When using electron-rich 1,4-phenylenediamine (PDA), we found it necessary to perform the reaction under an inert atmosphere with degassed solvent to avoid aerobic oxidation of the linker (**Figure 2.8I**). Interestingly, although stacking does not occur in 3D-COFs, COF-300 could also be synthesized under these conditions with very good crystallinity, albeit in the hydrated state (**Figure 2.8J**) [21]. In the case of TAPT-IP, a geometrically challenging COF with a dialdehyde monomer where both aldehydes are not oriented along the same axis, the BET surface area of 570 m² g⁻¹ exceeded that of the same COF made by both solvothermal and sonochemical methods (**Figure 2.8L**) [12, 22]. The use of triformylphloroglucinol as the aldehyde linker yielded a COF of weak crystallinity (**Figure A.14**). We believe the conditions described here are not suited to ensure sufficient error correction due to the poor reversibility of the stable β-keto-enamine bonds. The structurally similar TAPT-TFPO COF, which contains only one hydroxylgroup on the aldehyde monomer, did show strong crystalline features in its PXRD pattern (**Figure 2.8K**).

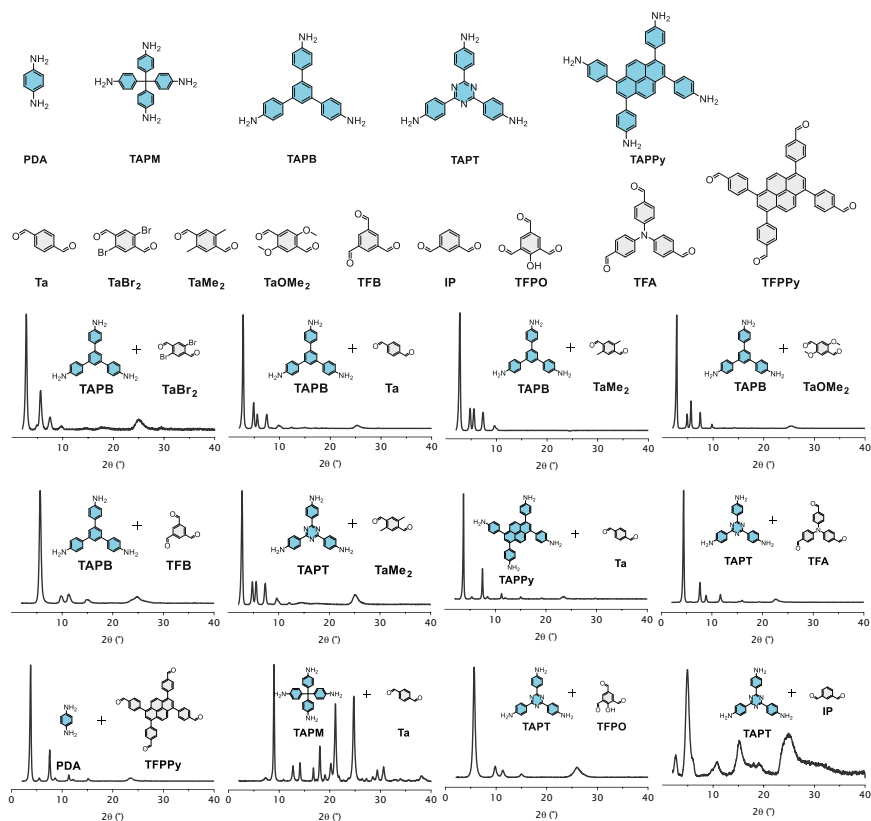


Figure 2.8. Overview of the different monomers and PXRD patterns of the 12 resultant COFs

Our synthesis method could also be used for the synthesis of known fragile COFs. We opted for diethyl ether as a low-surface tension solvent for mild activation instead of the previously reported supercritical CO_2 , hexane or perfluorohexane. Diethyl ether has a lower surface tension ($\gamma = 17.15 \text{ mN/m}$ at $25 \text{ }^\circ\text{C}$) than n-hexane ($\gamma = 18.43 \text{ mN/m}$), but is less environmentally damaging than n-hexane or perfluorohexane, and can, contrary to supercritical CO_2 , be used at ambient pressure. The BET surface area of TAPB-Ta ($2107 \text{ m}^2/\text{g}$) made in this manner was comparable to that of COFs activated with supercritical CO_2 ($2097 \text{ m}^2/\text{g}$), hexane ($2060 \text{ m}^2/\text{g}$) or perfluorohexane ($2121 \text{ m}^2/\text{g}$) [23].

Because of the cheap solvent and catalyst and the convenient synthetic conditions, our method allows for facile synthesis of COFs on a multigram scale. We could synthesize more than 10 grams of TAPT-TaMe₂ COF in one batch by simply scaling the monomer and solvent amount. The COF was obtained in 88% yield and showed a nearly identical crystallinity as the small-scale synthesis, indicating the potential of this method for the synthesis of COFs on an industrial scale (**Figure A.15**, **Figure A.16**).

2.5 A terpyridine covalent organic framework

Extensive work has been done on the use of covalent organic frameworks containing bidentate ligands (e.g. bipyridine or phenantroline), or tetradentate ligands (e.g. porphyrine and phthalocyanine) [24–27] (**Figure 2.9**). However, research on COFs with tridentate ligands is very scarce. To the best of our knowledge, only one article has been published which describes an imine-linked covalent organic framework containing a tridentate ligand. Chen et al. synthesized three COFs containing either ditopic pyridine-2,6-dicarbaldehyde or the tetratopic 4,4'-(1,4-phenylene)bis(pyridine-2,6-dicarbaldehyde) [28]. These monomers show rotation around the aldehyde bond. As a result, it is difficult to form a crystalline COF due to the high degree of freedom in bond connectivity. In order to obtain crystalline frameworks, the authors added Zn(NO₃)₂ during the COF synthesis. The zinc ions complex with the in situ formed

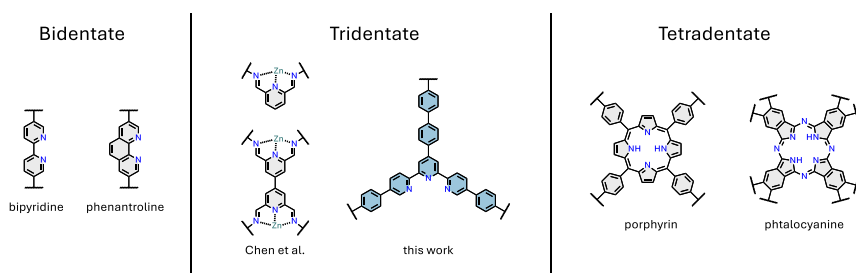


Figure 2.9. Reported multidentate ligands in COFs

pyridine-2,6-diimine motifs, forcing them into a curved geometry, which allows the formation of crystalline COFs. The resultant COFs are automatically metallated with zinc, and could be used for zinc ion conduction in batteries. While elegant, this method is restricted to the synthesis of metallated COFs. The authors attempted to remove the zinc ions after synthesis by treatment with aqueous ammonia, but more than 0.5 wt% was still present even after washing for three days. On top of that, the demetallated COF lost more than 50% of its BET surface area. Finally, the viability of this method was only demonstrated for zinc. The authors did not report whether they attempted other metals, but it is unlikely that this method will work for every metal. As the metal ion is directly bound to the imine nitrogen, it alters the electron density of the imine bond. The metal ion might in this way make the imine bond very stable, or just very labile, which interferes with the reversibility of the imine bond formation, crucial for the formation of a crystalline covalent organic framework. We therefore decide to attempt the synthesis of a COF containing a tridentate terpyridine ligand that contains no metal whatsoever. The open terpyridine site then offers a strong tridentate ligand which can readily accept and stabilize different metals.

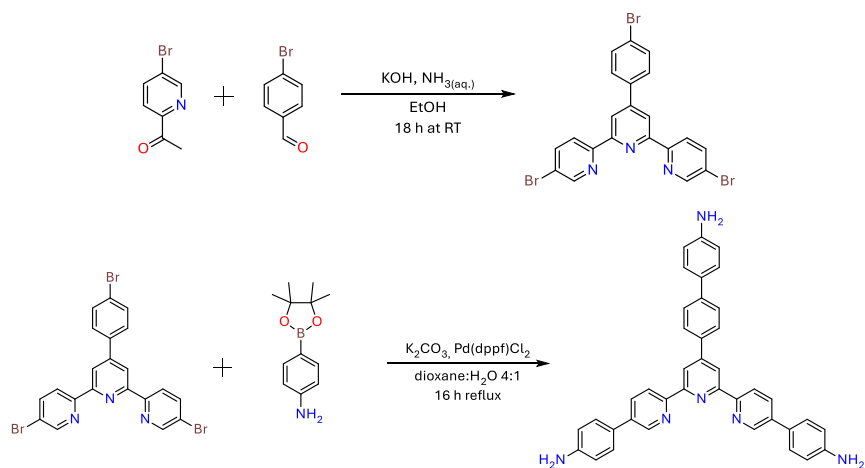


Figure 2.10. Synthesis of TABPy

To this end, we produced a novel amine containing terpyridine ligand, synthesized conveniently in two steps from commercially available compounds. 4-formylbenzotrile, 1-(5-bromopyridin-2-yl)ethanone reacted in a modified one-pot Kröhnke-type pyridine synthesis to form 1,3,5-tris(bromophenyl)terpyridine (TBP_y). This compound then underwent Suzuki coupling together with 4-aminophenylboronic acid pinacol ester to give 4,4'-(4'-(4'-2-amino-[1,1'-biphenyl]-4-yl)-[2,2':6',2''-terpyridine]-5,5''-diyl)dianiline (TABP_y) (**Figure 2.10**). In this monomer, the terpyridine group is inherently present: the imine bonds formed during COF synthesis make no part of it. This means that no metal ions are necessary to lock the symmetry during COF synthesis.

For the aldehyde monomer, we chose to use 2,4,6-trimethylbenzene-1,3,5-tricarbaldehyde (TFM). We chose this monomer for two reasons. For use in photocatalytic CO₂ reduction, the COF will be submerged in water. Recycling the COF can be done easily by simply filtrating the reaction mixture. As water has an exceptionally high surface tension, it is highly important that the COF is robust to pore collapse, so that recycling can be done without any additional mild activation steps. Due to its small size, the combination of TABP_y with TFM should give a COF with relatively small pores, which enhances resilience of the COF to pore collapse. Due to the presence of the methylgroups, this C₃-symmetric aldehyde has been shown to stabilize COF structures, further improving their robustness [29]. Furthermore, TFM can be easily made in two steps on gram scale starting from mesitylene with minimal purification. The synthetic details for both monomers, and confirmation of the correct structure of TABP_y via ¹H-NMR are described in **subsection 2.7.1**.

Again, simple stirring of both monomers in a mixture of n-butanol, acetic acid and water for 16 h at 70 °C under air yielded the COF TABP_y-TFM as a beige-brown crystalline powder with a yield of 91% (**Figure 2.11**). We found that Soxhlet extraction with THF overnight was in this case necessary to remove all traces of the poorly soluble monomer TABP_y

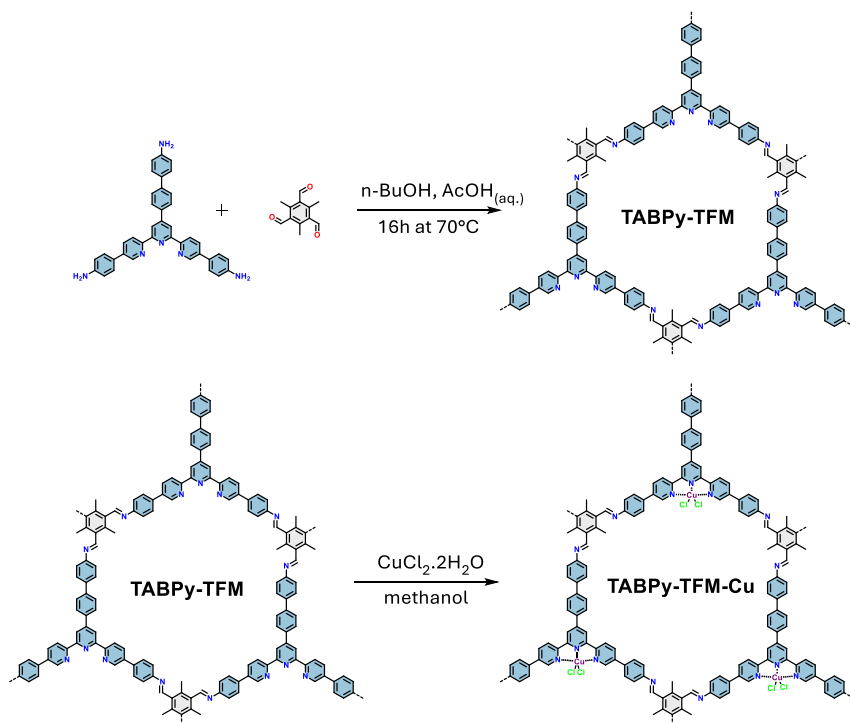


Figure 2.11. Synthesis of TABPy-TFM and TABPy-TFM-Cu

and possible oligomers. Details of the COF synthesis are given in **subsection 2.7.4**.

The successful polymerization of the monomers to the COF could be confirmed by FTIR spectroscopy (**Figure A.17**). The characteristic aldehyde $\text{C}=\text{O}$ vibration of TFM at 1680 cm^{-1} has largely disappeared, while a new peak at 1627 cm^{-1} can be seen, indicative of the imine bond $\text{C}=\text{N}$ stretching vibration.

Powder X-ray diffraction (PXRD) demonstrated the crystalline structure of TABPy-TFM. The major peak positions at 4.00° , 6.95° , 7.98° , 10.62° were ascribed to the (100), (110), (200) and (210) reflections respectively. These peaks correspond very well to the simulated pattern with AA stacking (**Figure 2.12**). TAPPy-TFM has a hexagonal topology with an in-plane

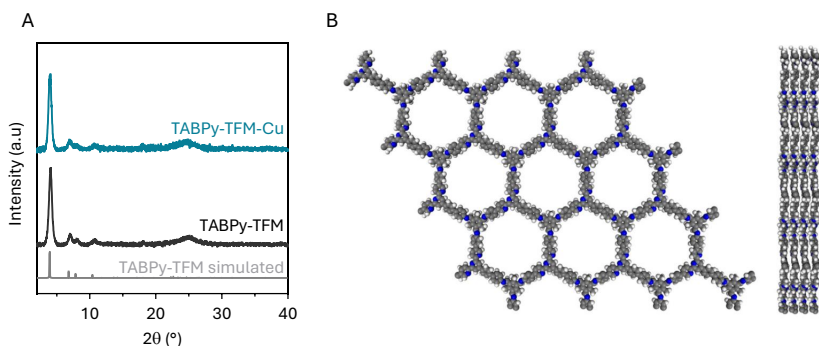


Figure 2.12. XRD pattern of TABPy-TFM, TABPy-TFM-Cu and the simulated AA stacking pattern of TABPy-TFM (A), the simulated AA structure of TABPy-TFM (B)

unit cell dimension of 25.9895 Å, and an interlayer stacking distance of 3.9824 Å. Pawley refinement further confirmed that this pattern is in good agreement with the theoretical structure (**Figure A.18**).

To assess the porosity of TABPy-TFM, N₂-sorption measurements were performed at 77K. As shown in **Figure 2.13A**, TAPBPY-TFM displays a typical type I isotherm, indicating the presence of micropores. To confirm this, the pore size distribution (PSD) was derived from the isotherm using quenched solid density functional theory (QSDFT). TAPBPY-TFM shows a narrow pore size distribution with a diameter of 1.92 nm, which matches well with the simulated maximum pore diameter of 1.96 nm. The Brunauer–Emmett–Teller (BET) surface area is 701 m² g⁻¹ and the total pore volume (at P/P₀= 0.95) 0.30 ml g⁻¹ (**Figure A.19**).

2.5.1 A preliminary test: photocatalytic CO₂ reduction

Having established the successful synthesis of the material, we aimed to demonstrate the capability of TABPy-TFM to adsorb metals in the open terpyridine sites. We chose to decorate the COF with copper, an abundant non-noble metal with many applications in catalysis. The

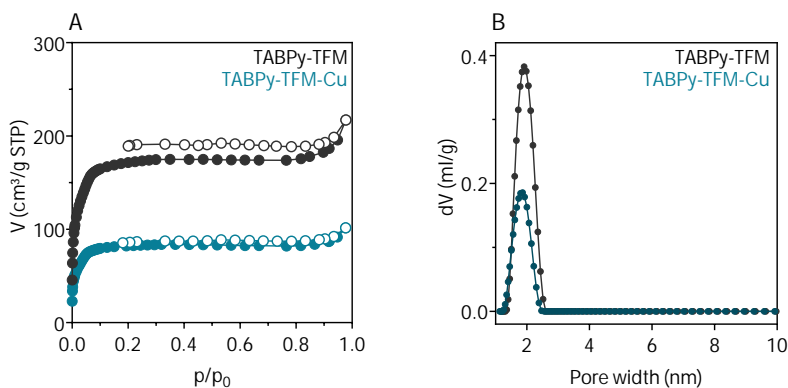


Figure 2.13. N_2 -isotherms measured at 77K of TABPy-TFM and TABPy-TFM-Cu (A), pore size distributions of TABPy-TFM and TABPy-TFM-Cu (B)

metallation of the COF was achieved by simply stirring the COF with a solution of $CuCl_2 \cdot 2H_2O$ in methanol at room temperature overnight (**Figure 2.11**). After washing and drying, the colour of the material had shifted from yellow-beige to red-brown. PXRD analysis showed that the crystallinity of the COF was retained, with virtually no shift in peak positions. The absence of peaks from $CuCl_2 \cdot 2H_2O$ indicates that no excess $CuCl_2 \cdot 2H_2O$ is left over in the pores.

An evident decrease in nitrogen gas uptake could be seen in the N_2 -sorption isotherms. The incorporation of $CuCl_2 \cdot 2H_2O$ lowered the total BET surface area and pore volume (at $P/P_0 = 0.95$) to respectively $337 \text{ m}^2 \text{ g}^{-1}$ and 0.13 ml g^{-1} . The coordinated copper and chloride ions takes up extra space in the pores, decreasing the pore volume, but also increasing the density of the COF, which inevitably also decreases the S_{BET} , since it is expressed per gram.

The incorporation of copper chloride was studied via X-ray photoelectron spectroscopy (XPS) measurements. The N 1s spectrum of TAPB-TTT was deconvoluted in two peaks, at 399.5 eV and 398.7 eV. These were assigned to the nitrogen from the imine linkages and the nitrogen from the terpyridine in TABPy respectively. Upon decoration with $CuCl_2 \cdot 2H_2O$, the peak

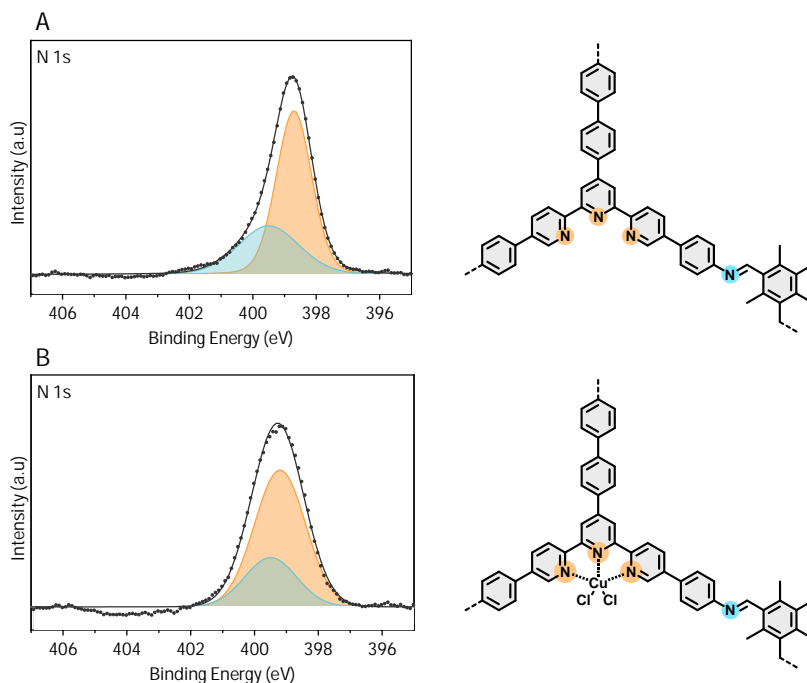


Figure 2.14. High-resolution XPS spectra of N 1s for TABPy-TFM (A) and TABPy-TFM-Cu (B). The deconvoluted peaks correspond in color to the chemical nitrogen species depicted on the right.

for the nitrogens in the terpyridine moieties had shifted significantly to 399.2 eV, indicating the different electron density around the nitrogen atoms in terpyridine as a result of the coordination with copper. The position of the imine peak meanwhile remained centered at 399.5 eV. Furthermore, signals for Cu and Cl were detected in TABPy-TFM-Cu. We quantified the amount of Cu and Cl to be 0.97 at% and 1.92 at%, which corresponds very well to the theoretically expected ratio of 1:2, indicating that Cu is still in the same oxidation state (+2) after complexation with terpyridine. From the quantitative signals of Cu and terpyridine nitrogen, we derived that about 51 % of the terpyridine sites are decorated with Cu.

From UV-Vis results and the corresponding Tauc plot, we obtained a band gap for TABPy-TFM-Cu of 1.43 eV (**Figure A.21**). This implies that the COF is theoretically capable of reducing CO₂ to CO and oxidizing water to O₂ at the same time ($\Delta E = 1.34$ eV). We tested this by irradiating the COF in a closed vial with water under a CO₂ atmosphere. To allow intimate contact with both the water and gaseous CO₂ phase, we added only a small amount of water, and stirred the reaction mixture. After 4 hours, we analyzed the headspace gas via GC. The results show that CO was produced. More importantly, only a trace amount of H₂ was formed over the same time period. No liquid products were detected by ¹H-NMR. This results in an impressive selectivity for CO of 98.7%. We determined the produced amount of CO to be 3.03 $\mu\text{mol g}^{-1} \text{h}^{-1}$. This is a modest value in comparison with reported COFs, however, these often rely on the addition of sacrificial agents for the oxidation reaction, or noble metal containing photosensitizers. Our system on the other hand requires only water, CO₂, and TABPy-TFM-Cu. Furthermore, after a catalytic reaction with CO₂, we could prove the retention of the chemical nature of the recycled catalyst with FT-IR (**Figure A.22A**). PXRD of the recycled catalyst also demonstrated that the crystallinity of TABPy-TFM-Cu was preserved (**Figure A.22B**). From XRF results, we found that the amount of Cu and Cl within the structure remained virtually the same before and after reaction, proving that terpyridine moieties are effective at binding the metal ions (**Figure A.22C**). These preliminary results prove that TABPy-TFM-Cu holds promise as a heterogeneous photocatalyst.

2.6 Conclusion

This work demonstrated that a wide variety of imine-linked covalent organic frameworks can be made in simple aqueous solutions of alkyl alcohols with acetic acid under mild conditions. Synthesis in alcohols with a carbon number higher than four produced well-ordered COFs, while in ethanol and methanol poorly crystalline polymers were obtained.

A combination of Raman spectroscopy, optical microscopy, PXRD and FTIR analysis indicated that alcohols with long alkyl chains promote efficient stitching of the COF nanosheets, leading to larger and well-stacked COF particles which resist pore collapse. We find this effect can be obtained by using in general a solvent with an apolar group that is still miscible with aqueous acetic acid. The green solvent combination of n-butanol, water and acetic acid was used to generate a variety of COFs under the same conditions with high crystallinity. This work proves that a broad range of highly crystalline COFs can be made without the use of ampules, high temperatures, expensive solvents, additives, or specialized catalysts. Rigorous exclusion of oxygen was also shown to be redundant in many COF syntheses. The method could moreover be easily scaled to the decagram scale. As a proof of concept, we synthesized a novel COF containing a terpyridine ligand. The terpyridine COF could be metallated easily with copper by simple stirring with $\text{CuCl}_2 \cdot 2\text{H}_2\text{O}$. As a proof of concept, we used the metallated COF for the photoreduction of CO_2 , and were capable of selectively reducing CO_2 to CO under visible light irradiation with 98.7% selectivity.

2.7 Experimental

2.7.1 Monomer synthesis

1,4-phenylenediamine (PDA) was obtained from TCI Europe. Tetrakisaminophenylmethane (**TAPM**), 1,3,5-tris(4-aminophenyl)benzene (**TAPB**), 1,3,5-tris(4-aminophenyl)triazine (**TAPT**), terephthalaldehyde (Ta), 1,3,5-triformylbenzene (**TFB**), isophthalaldehyde (**IP**) and tris(4-formylphenyl)amine (**TFA**) were obtained from BLD Pharmatech. 2,5-dibromoterephthalaldehyde (**TaBr₂**) [30], 2,5-dimethylterephthalaldehyde (**TaMe₂**) [31] and 1,3,5-triformylphenol (**TFPO**) [32] were synthesized according to literature. 1,3,6,8-tetrakis(4-aminophenyl)pyrene

(**TAPPy**) [33], 1,3,6,8-tetrakis(4-formylphenyl)pyrene (**TFPPy**) [33], 2,4,6-trimethylbenzene-1,3,5-tricarbaldehyde (**TFM**) [29], 5,5''-dibromo-4'- (4-bromophenyl)-2,2':6',2''-terpyridine [34] were synthesized using modified literature recipes.

1,3,6,8-tetrakis(4-aminophenyl)pyrene (TAPPy) 1,3,6,8-tetrabromopyrene (371 mg, 0.72 mmol, 1.0 eq.), 4-aminophenylboronic acid pinacol ester (756 mg, 3.45 mmol, 4.8 eq.) in 8 mL 1,4-dioxane and 2 mL H₂O were added to a 100 mL 2-necked round bottom flask. The mixture was refluxed under argon using a heating mantle for 30 minutes to degas the reaction mixture. Under an argon stream, K₂CO₃ (547 mg, 3.66 mmol, 5.5 eq.) and Pd(dppf)Cl₂ (26 mg, 0.036 mmol, 5 mol%) were added in one portion. Reflux under argon was continued for 16h. After cooling to room temperature, 20 mL H₂O was added. The resulting precipitate was collected via filtration and washed subsequently with H₂O and MeOH. The resulting yellow powder was dried under vacuum (354 mg, 0.63 mmol, 87% yield). ¹H-NMR (300 MHz, DMSO-*d*₆, 298 K): 8.14 (s, 4 H), 7.80 (s, 2 H), 7.35 (d, 8 H), 6.78 (d, 8 H), 5.31 (s, 8 H).

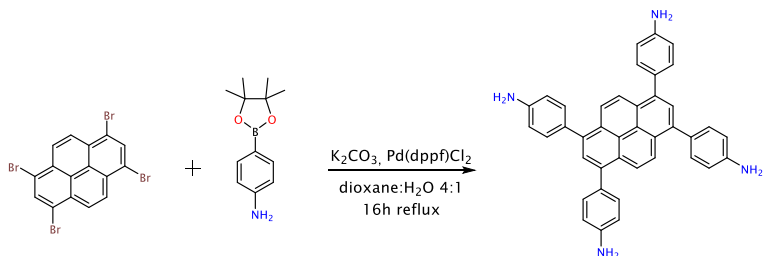


Figure 2.15. Synthesis of 1,3,6,8-tetrakis(4-aminophenyl)pyrene (TAPPy)

1,3,6,8-Tetrakis(4-formylphenyl)pyrene (TFPPy) 1,3,6,8-tetrabromopyrene (371 mg, 0.72 mmol, 1.0 eq) and 4-

formylphenylboronic acid (480 mg, 3.20 mmol, 4.8 eq.), 8 mL 1,4-dioxane and 2 mL H₂O were added to a 100 mL 2-necked round bottom flask. The mixture was refluxed under argon using a heating mantle for 30 minutes to degas the reaction mixture. Under an argon stream, K₂CO₃ (547 mg, 3.66 mmol, 5.5 eq.) and Pd(dppf)Cl₂ (26 mg, 0.036 mmol, 5 mol%) were added in one portion. Reflux under argon was continued for 16h. After cooling to room temperature, 20 mL H₂O was added to the mixture. The precipitate was collected by filtration and washed with H₂O and MeOH. The resulting yellow powder was dried under vacuum (404 mg, 0.65 mmol, 91% yield). ¹H-NMR (300 MHz, CDCl₃, 298 K): 10.17 (s, 4H), 8.18 (s, 4H), 8.10 (d, 8H), 8.04 (s, 2H), 7.86 (d, 8H).

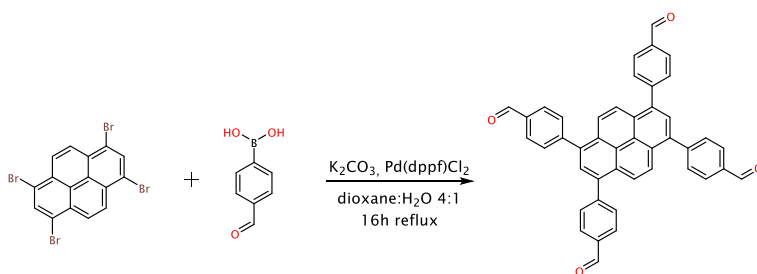


Figure 2.16. Synthesis of 1,3,6,8-Tetrakis(4-formylphenyl)pyrene (TFPPY)

5,5''-dibromo-4'-(4-bromophenyl)-2,2':6,2''-terpyridine (TBPY)

1-(5-bromopyridin-2-yl)ethanone (1680 mg, 8.4 mmol) and 4-bromobenzaldehyde (845 mg, 4.5 mmol) were suspended in 35 ml absolute ethanol in a 100 mL round bottom flask. After stirring for ten minutes, 1.10 g KOH was added. After stirring for another 10 minutes, 24 ml of a 25 wt NH₃ solution was added. The mixture was then stirred at room temperature for 18 hours. At the end of the reaction, a white precipitate was obtained, which was filtered, then washed

with water. Recrystallization from chloroform yielded the product as colorless needles, which were dried under vacuum for 16 hours. Yield 67% $^1\text{H-NMR}$ (300 MHz, CDCl_3 , 298 K): 8.77 (s, 2H), 8.68 (s, 2H), 8.54 (d, 2H), 8.00 (d, 2H), 7.75 (d, 2H), 7.65 (d, 2H).

4,4'-(4'-(4'-2-amino-[1,1'-biphenyl]-4-yl)-[2,2':6',2''-terpyridine]-5,5''-diyl)dianiline (TABPy)

273 mg TBPY (0.5 mmol) and 438 mg 4-aminophenylboronic acid pinacol ester (2 mmol, CAS: 214360-73-3) and 380 mg K_2CO_3 were suspended in 8 ml dioxane and 2 ml H_2O in a Schlenk flask or tube. The reaction mixture was degassed by bubbling argon for 30 minutes. Under an argon flow, 30 mg $\text{Pd}(\text{dppf})\text{Cl}_2$ was added. The mixture is stirred at $100\text{ }^\circ\text{C}$ for 18h under argon. After cooling to room temperature, 50 mL distilled water was added, and the reaction mixture was filtered. The brown precipitate was washed with water, methanol and chloroform, then dried under vacuum. Yield 83%. $^1\text{H-NMR}$ (300 MHz, DMSO-d_6 , 298 K): 9.01 (s, 2H), 8.73 (s, 2H), 8.68 (d, 2H), 8.20 (d, 2H), 7.97 (d, 2H), 7.80 (d, 2H), 7.57 (d, 4H), 7.51 (d, 2H).

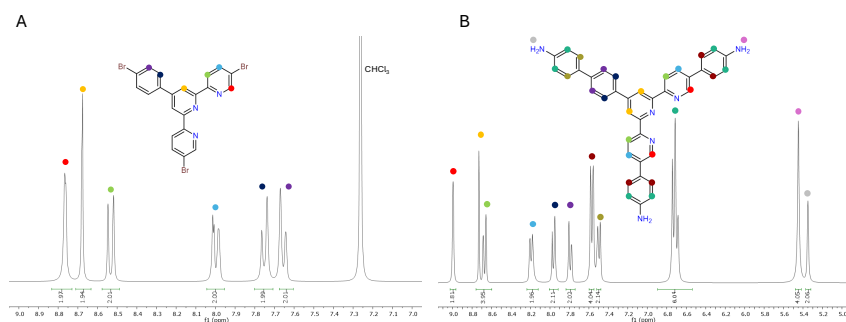


Figure 2.17. Assigned $^1\text{H-NMR}$ spectra of TBPY (A) and TAPBy (B) recorded at 300 MHz in respectively CDCl_3 and DMSO-d_6

1,3,5-tris(bromomethyl)-2,4,6-trimethylbenzene

2.33 mL mesitylene, 8.3 mL glacial acetic acid, and 8.3 mL HBr in acetic acid (30 wt% solution) and 2 g of paraformaldehyde were added in a 50 mL Schlenk tube. The atmosphere was replaced by argon, and the mixture

was then stirred at 90 °C overnight. A dense white precipitate formed already after a few minutes. After cooling down to room temperature, the mixture was poured in 100 mL of water. The white precipitate was filtered off, washed with water, then a little methanol, and dried under vacuum. The white solid was dissolved in DCM, and hexane was added until the solution turned cloudy. The cloudy suspension was then cooled to 0 °C in a fridge overnight to obtain white crystals, which were filtered and dried under vacuum. Yield 47 %. ¹H-NMR (300 MHz, CDCl₃, 298 K): 4.58 (s, 6H), 2.47 (s, 9H)

2,4,6-trimethylbenzene-1,3,5-tricarbaldehyde (TFM)

30 mL of anhydrous ethanol was added to a dry 100 mL round bottom flask, together with a stirring bar. After flusing with argon, 300 mg of Na metal was added, and stirred until dissolved (ca. 20 minutes). Then, 1.33 mL 2-nitropropane was added, and the solution was stirred for another hour to allow formation of the sodium salt of 2-nitropropane. After one hour, 1 g of 1,3,5-tris(bromomethyl)-2,4,6-trimethylbenzene was added, and the mixture was stirred for 16 hours under argon at room temperature. After this time, a white precipitate had formed. 20 mL of water was added, and the precipitate was filtered. The filtrate was then extracted with DCM (3 x 15 mL), dried over anhydrous MgSO₄ and the solvent removed under reduced pressure to obtain a white powder. The white powder was combined with the precipitate filtered from the earlier step, and the combined solid was recrystallized from a small amount of chloroform. Yield 53 %. ¹H-NMR (300 MHz, CDCl₃, 298 K): 10.62 (s, 6H), 2.65 (s, 9H)

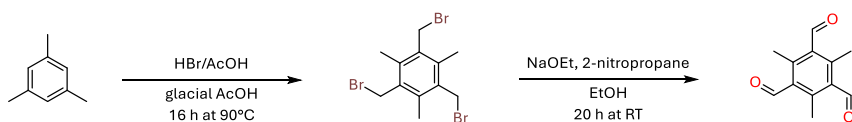


Figure 2.18. Synthesis of 1,3,5-tris(bromomethyl)-2,4,6-trimethylbenzene and 2,4,6-trimethylbenzene-1,3,5-tricarbaldehyde

2.7.2 Optimization of COF synthesis

10.5 mg TAPB (0.03 mmol, 0.09 mmol aminegroups) and 13.1 mg TaBr₂ (0.045 mmol, 0.09 mmol aldehydegroups) were added to a 4 mL glass vial containing an oblong teflon stirring bar with a length of 1 cm. 0.75 mL of a mixture of alkyl alcohol, acetic acid and water was added as described in **Table 2.1**. The vial was closed with a plastic screwcap, heated to 70°C in an aluminium heating block and stirred for 16 hours at 250 RPM. After cooling to room temperature, the obtained yellow slurry was filtered over a nylon filter of 0.45 µm pore diameter, washed with 10 mL H₂O, 2x10 mL methanol, then 2x10 mL acetone. The powder was soaked in the solvent for 10 minutes each washing step. The resulting yellow powder was dried at 90°C under vacuum for 16 hours. For mild activation, after washing with acetone, the COF was washed with 10 mL diethyl ether, then submerged in 10 mL diethyl ether for 6 hours. Care was taken to never let the COF become completely dry between the washing steps. The damp COF was dried at room temperature and ambient pressure for 16 hours.

2.7.3 General COF synthesis

An amount of amine-containing monomer was weighed so that the total amount of amine groups was 0.09 mmol. An amount of aldehyde-containing monomer was weighed so that the the total amount of aldehyde groups was 0.09 mmol. The exact weights for each COF are denoted below in **Table 2.2**. Both monomers were added to a 4 mL glass vial containing an oblong teflon stirring bar with a length of 1 cm. Next, 0.75 mL of a solution consisting of 0.503 mL n-butanol, 0.075 mL water and 0.172 mL glacial acetic acid was added via a syringe. A 50 mL stock solution of this mixture can be made by mixing 33.5 mL n-butanol, 11.5 mL acetic acid and 5 mL H₂O. The vial was closed with a plastic screwcap, heated to 70°C in an aluminium heating block and stirred for 16 hours at 250 RPM. After cooling to room temperature, the obtained yellow slurry was

Deviation from standard conditions	Solvent	Solvent (mL)	H ₂ O (mL)	AcOH (mL)	T (°C)	Time (h)
none	n-BuOH	0.503	0.075	0.172	70	16
0 v% H ₂ O	n-BuOH	0.578	0	0.172	70	16
20 v% H ₂ O	n-BuOH	0.428	0.15	0.172	70	16
40 v% H ₂ O	n-BuOH	0.278	0.3	0.172	70	16
60 v% H ₂ O	n-BuOH	0.128	0.60	0.172	70	16
1 M AcOH	n-BuOH	0.632	0.075	0.043	70	16
2 M AcOH	n-BuOH	0.589	0.075	0.086	70	16
8 M AcOH	n-BuOH	0.330	0.075	0.345	70	16
12 M AcOH	n-BuOH	0.158	0.075	0.517	70	16
20 °C	n-BuOH	0.503	0.075	0.172	20	16
120 °C	n-BuOH	0.503	0.075	0.172	120	16
4h	n-BuOH	0.503	0.075	0.172	70	4
72h	n-BuOH	0.503	0.075	0.172	70	72
methanol	MeOH	0.503	0.075	0.172	70	16
ethanol	EtOH	0.503	0.075	0.172	70	16
n-propanol	PrOH	0.503	0.075	0.172	70	16
n-hexanol	HxOH	0.503	0.075	0.172	70	16
n-octanol	OcOH	0.503	0.075	0.172	70	16
n-decanol	DcOH	0.503	0.075	0.172	70	16

Table 2.1. Optimization attempts of TAPB-TaBr₂

filtered over a nylon filter of 0.45 μm pore diameter, washed with 10 mL H₂O, 2x10 mL methanol, then 2x10 mL acetone. The powder was soaked in the solvent for 10 minutes each washing step. The resulting yellow powder was dried at 90°C under vacuum for 16 hours.

Mild activation was used for TAPB-Ta, TAPT-TFA and TAPT-IP: after washing with acetone, the COF was washed with 10 mL diethyl ether, then submerged in 10 mL diethyl ether. Care was taken to never let the COF become completely dry between the washing steps. The damp COF was dried at room temperature and ambient pressure for 16 hours.

COF	Aldehyde (mg)	Amine (mg)	Yield
TAPB-Ta	6.0	10.5	88%
TAPB-TaBr ₂	13.1	10.5	92%
TAPB-TaMe ₂	7.7	10.5	91%
TAPB-TaOMe ₂	8.7	10.5	94%
TAPB-TFB	4.9	10.5	94%
TAPM-Ta	6.0	8.6	84%
PDA-TFPPy	13.9	4.9	87%
TAPPy-Ta	12.8	12.8	96%
TAPT-IP	6.0	10.6	82%
TAPT-TaMe ₂	7.7	10.6	90%
TAPT-TFA	9.9	10.6	83%
TAPT-TFPO	5.3	10.6	82%

Table 2.2. Amounts of monomer used and yields for the different reported COFs

2.7.4 Synthesis of TABPy-TFM

TABPy-TFM 52.5 mg TABPy (0.09 mmol) and 18.3 mg TFM (0.09 mmol) were added to a 4 mL glass vial containing an oblong teflon stirring bar with a length of 1 cm. 2.25 mL of a solution consisting of 1.5 mL *n*-butanol, 0.225 mL water and 0.525 mL glacial acetic acid was added. The vial was closed with a plastic screwcap, heated to 70°C in an aluminium heating block and stirred for 16 hours at 250 RPM. After cooling to room temperature, the obtained yellow slurry was filtered over a nylon filter of 0.45 µm pore diameter, washed with 10 mL H₂O, 10 mL acetone, then 10 mL methanol. The powder was soaked in the solvent for 10 minutes each washing step. The COF was then thoroughly washed by Soxhlet extraction with THF for 16 hours. The resulting brown powder was dried at 90°C under vacuum for 16 hours (64.6 mg, 91% yield).

TABPy-TFM-Cu Loading with copper was done by dispersing 20 mg COF in 2 mL of methanol, then adding 20 mg CuCl₂·2H₂O and stirring at room temperature for 16 hours. The resulting red-brown material was filtered off, washed with H₂O, then MeOH, and dried under vacuum.

2.7.5 Materials characterization

Fourier Transform Infrared Spectroscopy (FT-IR) in the region of 4000 cm^{-1} to 650 cm^{-1} was recorded on a Perkin-Elmer Spectrum 1000 FTIR spectrometer with a PIKE Miracle ATR unit in a frequency range from 4000 to 600 cm^{-1} . Dispersive Raman spectra were recorded on a RXN1 Raman spectrometer (Kaiser Optical Systems) fitted with a 532 nm laser operating at 40 mW in the range 1800-900 cm^{-1} . Powder X-ray diffraction (PXRD) patterns were collected on a Bruker D8 Advance diffractometer equipped with an autochanger and LynxEye XE-T Silicon strip Line detector, operated at 40 kV, 30 mA using Cu-K α radiation ($\lambda = 1.5406 \text{ \AA}$) in Bragg-Brentano geometry. The patterns were baseline corrected using the Bruker DIFFRAC.EVA software. $^1\text{H-NMR}$ spectra were collected on a Bruker Avance 300 at 300 MHz. The residual solvent signal at 7.26 ppm for CDCl_3 and at 2.50 ppm for $\text{DMSO-}d_6$ was used for chemical shift referencing. Optical microscopy was performed with an Olympus SZ61-TR optical stereomicroscope, equipped with a Dino-Eye Edge USB camera. Scanning Electron Microscopy (SEM) was performed on a JCM-7000 NeoScopeTM Benchtop SEM from JOEL. Samples were fixed with double-sided carbon tape to the sample holder. The samples were vacuum coated with gold for 60 s at 20 mA using an automatic Au Sputter Coater K550X from EmiTech with a RV3 two-stage rotary vane pump before measurement. Diffuse Reflectance UV-Visible spectra were measured on a Varian Cary 500 scanning spectrophotometer and converted to absorbance spectra using the Kubelka-Munk transformation. X-ray fluorescence (XRF) spectra were recorded using a Rigaku NEX CG energy-dispersive X-ray fluorescence spectrometer with RX9 and Mo secondary targets. The surface chemical composition of the samples was investigated by X-ray photoelectron spectroscopy (XPS) using the PHI 5000 VersaProbe II spectrometer equipped with a monochromatic Al K α X-ray source ($h\nu = 1486.6 \text{ eV}$). To do so, the samples were excited with an X-ray beam (size: 200 μm) over an area of 500 x 500 μm^2 at a power of 50 W. Wide range survey scans and high-resolution spectra were recorded with

a pass energy of 187.85 eV and 23.5 eV and a step size of 0.8 eV and 0.1 eV respectively. All spectra were acquired at a take-off angle of 45° relative to the sample surface in the XPS chamber where the pressure was constantly maintained below 10⁻⁶ Pa. The high-resolution spectra were deconvoluted using Fityk 1.3.1. The spectra were background corrected using a Shirley baseline. The peaks were fitted to Pseudo-Voigt peak profiles. The fitting optimization was done using the Levenberg–Marquardt algorithm. Nitrogen sorption was performed at 77K using a Micromeritics Tristar II. Samples were activated before measurement by heating at 120 °C for 12 hours under vacuum. Adsorption points are depicted as closed circles, while open circles are desorption points. The range for calculation of the BET surface area was chosen so that the following criteria were met:

1. The term $V_{ads}(1 - \frac{p}{p_0})$ must continuously increase with $\frac{p}{p_0}$
2. C must be positive
3. The value for R^2 must be equal to or greater than 0.995
4. The $\frac{p}{p_0}$ value corresponding to V_m must lie within the selected BET range.

2.7.6 Photocatalytic CO₂ reduction

5 mg of TABPy-TFM was charged in a 4 mL vial with a septum and a stirring bar, and 100 μL distilled water was added. The vial was purged with CO₂ (99.999%, Air Liquide) for 10 minutes. 100 μL He (99.9999%, Air Liquide) was then added via a gas syringe as an internal standard. The sample was irradiated whilst stirring with a white light inside a PhotoRedOx Box™ (HepatoChem). After 4 hours of reaction, a sample was taken via a 10 mL gas syringe. An argon filled balloon was added via a needle during sampling to balance the pressure. The gas sample was then injected into an Agilent 990 Micro GC operating on Ar carrier gas, equipped with a Molsieve 5A, 10m column and a PoraPlot U, 10 m column. For quantitative determination, all chromatograms were normalized to the

He peak to account for small air leaks during sampling and sample introduction.

2.7.7 Structural modelling

Pawley refinement of the PXRD patterns was carried out using the Reflex module of BIOVIA Materials Studio 2017 (17.1.0.48) (Dassault Systèmes, San Diego, 2017). The geometry optimized models of the COFs were used to provide starting unit cell parameters for refinement. The experimental PXRD patterns were refined from 2.0 to 40° in 2θ , and peaks were fitted to Pseudo-Voigt peak profiles. The freely varying parameters set for the refinement were the full width at half maximum (FWHM) parameters U, V, W from the Caglioti formula (describing peak broadening), the profile parameters NA and NB (describing peak shape angle dependence), and the unit cell parameters a, b, c (while keeping atomic fractional coordinates fixed). The experimental background was modelled with a polynomial of degree 20. No corrections were made for line shift or peak asymmetry or broadening due to crystallite size, lattice strain, or preferred orientation. The Pawley refined patterns and the parameters are shown in **Figure A.2** and **Table A.1**.

References

1. Matsumoto, M., Dasari, R. R., Ji, W., *et al.* Rapid, low temperature formation of imine-linked covalent organic frameworks catalyzed by metal triflates. *Journal of the American Chemical Society* **139**, 4999–5002 (2017).
2. Zhu, D., Zhang, Z., Alemany, L. B., *et al.* Rapid, ambient temperature synthesis of imine covalent organic frameworks catalyzed by transition-metal nitrates. *Chemistry of Materials* **33**, 3394–3400 (2021).

3. Zhu, Y., Zhu, D., Yan, Q., *et al.* Metal oxide catalysts for the synthesis of covalent organic frameworks and one-step preparation of covalent organic framework-based composites. *Chemistry of Materials* **33**, 6158–6165 (2021).
4. Shi, X., Yi, L. & Deng, H. Covalent organic frameworks catalyzed by organic Lewis acid. *Science China Chemistry* **65**, 1315–1320 (2022).
5. Zhang, L., Liang, R., Hang, C., *et al.* A facile solution-phase synthetic approach for constructing phenol-based porous organic cages and covalent organic frameworks. *Green chemistry* **22**, 2498–2504 (2020).
6. Zhu, D., Alemany, L. B., Guo, W. & Verduzco, R. Enhancement of crystallinity of imine-linked covalent organic frameworks via aldehyde modulators. *Polymer Chemistry* **11**, 4464–4468 (2020).
7. Dautzenberg, E., Claassen, F. W. & de Smet, L. C. Functionalized modulators in imine-linked covalent organic frameworks (COFs). *Microporous and Mesoporous Materials* **350**, 112318 (2023).
8. Tan, F., Zheng, Y., Zhou, Z., *et al.* Aqueous synthesis of covalent organic frameworks as photocatalysts for hydrogen peroxide production. *CCS Chemistry* **4**, 3751–3761 (2022).
9. Guo, L., Zhang, Q. Y., Yu, Z., Krishna, R. & Luo, F. Minute and Large-Scale Synthesis of Covalent-Organic Frameworks in Water at Room Temperature by a Two-Step Dissolution–Precipitation Method. *Chemistry of Materials* **35**, 5648–5656 (2023).
10. Vitaku, E. & Dichtel, W. R. Synthesis of 2D imine-linked covalent organic frameworks through formal transimination reactions. *Journal of the American Chemical Society* **139**, 12911–12914 (2017).
11. Sprachmann, J., Grabicki, N., Möckel, A., *et al.* Substituted benzophenone imines for COF synthesis via formal transimination. *Chemical Communications* **59**, 13639–13642 (2023).
12. Zhao, W., Yan, P., Yang, H., *et al.* Using sound to synthesize covalent organic frameworks in water. *Nature Synthesis* **1**, 87–95 (2022).

13. Zhu, D., Zhang, J.-J., Wu, X., *et al.* Understanding fragility and engineering activation stability in two-dimensional covalent organic frameworks. *Chemical Science* **13**, 9655–9667 (2022).
14. Liu, Q., Liao, Q., Hu, J., *et al.* Covalent organic frameworks anchored with frustrated Lewis pairs for hydrogenation of alkynes with H₂. *Journal of Materials Chemistry A* **10**, 7333–7340 (2022).
15. Zhao, L., Tang, X., Ni, X., *et al.* Efficient and Selective Adsorption of cis-Diols via the Suzuki–Miyaura Cross-Coupling-Modified Phenylboronic-Acid Functionalized Covalent Organic Framework. *Langmuir* **40**, 1884–1891 (2024).
16. Schoustra, S. K., de Heer Kloots, M. H., Posthuma, J., *et al.* Raman Spectroscopy Reveals Phase Separation in Imine-Based Covalent Adaptable Networks. *Macromolecules* **55**, 10341–10355 (2022).
17. Gen, M. & Chan, C. K. Electro spray surface-enhanced Raman spectroscopy (ES-SERS) for probing surface chemical compositions of atmospherically relevant particles. *Atmospheric Chemistry and Physics* **17**, 14025–14037 (2017).
18. Feriante, C., Evans, A. M., Jhulki, S., *et al.* New mechanistic insights into the formation of imine-linked two-dimensional covalent organic frameworks. *Journal of the American Chemical Society* **142**, 18637–18644 (2020).
19. Feriante, C. H., Jhulki, S., Evans, A. M., *et al.* Rapid Synthesis of High Surface Area Imine-Linked 2D Covalent Organic Frameworks by Avoiding Pore Collapse During Isolation. *Advanced Materials* **32**, 1905776 (2020).
20. Alder, C. M., Hayler, J. D., Henderson, R. K., *et al.* Updating and further expanding GSK's solvent sustainability guide. *Green Chemistry* **18**, 3879–3890 (2016).
21. Ji, W., Kim, D. M., Posson, B. M., *et al.* COF-300 synthesis and colloidal stabilization with substituted benzoic acids. *RSC advances* **13**, 14484–14493 (2023).

22. Krishnaraj, C., Jena, H. S., Rawat, K. S., *et al.* Linker engineering of 2D imine covalent organic frameworks for the heterogeneous palladium-catalyzed Suzuki coupling reaction. *ACS Applied Materials & Interfaces* **14**, 50923–50931 (2022).
23. Zhu, D. & Verduzco, R. Ultralow surface tension solvents enable facile COF activation with reduced pore collapse. *ACS applied materials & interfaces* **12**, 33121–33127 (2020).
24. Hosokawa, T., Tsuji, M., Tsuchida, K., *et al.* Metal-doped bipyridine linked covalent organic framework films as a platform for photo-electrocatalysts. *Journal of Materials Chemistry A* **9**, 11073–11080 (2021).
25. Wang, W., Kale, V. S., Cao, Z., *et al.* Phenanthroline covalent organic framework electrodes for high-performance zinc-ion supercapattery. *ACS Energy Letters* **5**, 2256–2264 (2020).
26. Chen, M., Li, H., Liu, C., *et al.* Porphyrin-and porphyrinoid-based covalent organic frameworks (COFs): From design, synthesis to applications. *Coordination Chemistry Reviews* **435**, 213778 (2021).
27. Wang, M., Ballabio, M., Wang, M., *et al.* Unveiling electronic properties in metal–phthalocyanine-based pyrazine-linked conjugated two-dimensional covalent organic frameworks. *Journal of the American Chemical Society* **141**, 16810–16816 (2019).
28. Chen, F., Zhang, K., Yuan, Y., *et al.* Ion-Conductive Metallo-Covalent Organic Frameworks Constructed with Tridentate Ligand and Zn Nodes. *Journal of the American Chemical Society* **145**, 25341–25351 (2023).
29. Dautzenberg, E., Lam, M., Li, G. & de Smet, L. C. Enhanced surface area and reduced pore collapse of methylated, imine-linked covalent organic frameworks. *Nanoscale* **13**, 19446–19452 (2021).
30. Prusinowska, N., Bardziński, M., Janiak, A., Skowronek, P. & Kwit, M. Sterically Crowded Trianglimines—Synthesis, Structure, Solid-State

- Self-Assembly, and Unexpected Chiroptical Properties. *Chemistry–An Asian Journal* **13**, 2691–2699 (2018).
31. Krishnaraj, C., Sekhar Jena, H., Bourda, L., *et al.* Strongly reducing (diarylamino) benzene-based covalent organic framework for metal-free visible light photocatalytic H₂O₂ generation. *Journal of the American Chemical Society* **142**, 20107–20116 (2020).
 32. Petryk, M., Szymkowiak, J., Gierczyk, B., *et al.* Chiral, triformylphenol-derived salen-type [4+ 6] organic cages. *Organic & Biomolecular Chemistry* **14**, 7495–7499 (2016).
 33. Ascherl, L., Evans, E. W., Hennemann, M., *et al.* Solvatochromic covalent organic frameworks. *Nature Communications* **9**, 3802 (2018).
 34. Zeng, L., Chen, Y., Huang, H., *et al.* Cyclometalated ruthenium (II) anthraquinone complexes exhibit strong anticancer activity in hypoxic tumor cells. *Chemistry–A European Journal* **21**, 15308–15319 (2015).

Linkage modification of
covalent organic
frameworks for
enhanced CO₂ sorption

3.1 Introduction

The use of COFs for CO₂ sorption has been extensively explored [1]. As explained in **subsection 1.2.2**, most of these reports have tried to improve the CO₂ sorption characteristics of a COF by choosing linkers that contain groups with high CO₂-affinity, such as amines or carboxylic acids. Such groups can be introduced *de novo*, or added to the linker via post-synthetic modification. Some examples of the latter include to reduction of a nitrile-containing COF to primary amines [2], acylation of a hydroxyl-containing COF [3], or even incorporation of metals in COFs that contain ligand sites such as bipyridines [4]. However, this strategy requires very specific, often expensive linkers, which hampers their practical applicability on a large scale. A less explored alternative strategy is conversion of the linkages. Imine-linked COFs and triazine-linked COFs tend to have in general a moderate CO₂-uptake regardless of the linker choice, by virtue of the CO₂-philic nitrogen sites in the linkages. By post-synthetic conversion, the CO₂ uptake of these linkages could potentially be further increased. The main advantage of this method is the generality: provided that the conversion reaction can proceed under mild conditions, linkage transformation could be used to enhance the CO₂ uptake of the entire set of COFs that are held together by this linkage. Research on this topic is relatively scarce. Liu et al. converted in 2018 the imine linkages in the archetypical 3D COF-300 to secondary amine linkages by reduction with NaBH₄ [5]. The crystallinity was largely retained after conversion. The reduced COF showed a rather low CO₂ uptake of around 0.54 mmol g⁻¹ at 273 K and 1 bar of CO₂. Lyu et al. reported in 2022 a COF for direct air capture [6]. To this end, they converted the imine linkage to a tetrahydroquinoline linkage through aza-Diels–Alder cycloaddition, and subsequently incorporated tris(3-aminopropyl)amine into the framework. Due to the introduction of primary amines, the resultant COF showed an impressive adsorption of 0.304 mmol CO₂ g⁻¹ at 0.4 mbar CO₂ and 298 K, meaning it can adsorb CO₂ from ambient air. At the same temperature and 1 bar of CO₂, it adsorbed around 2.14 mmol

g^{-1} . However, the post-synthetic conversion is comprised of two steps and requires the use of toxic 2-chloroethyl vinyl ether, making it less attractive for industrial production. Furthermore, the CO_2 -sorption occurs via chemisorption: the CO_2 molecules react with the amine groups to produce carbamates. This means more energy will be needed to desorb the CO_2 from the COF again. Another interesting work where linkages are responsible for the CO_2 sorption is the work of Das. et al from 2019 [7]. They synthesized a benzimidazole linked COF, which adsorbed an impressive 3.08 mmol g^{-1} of CO_2 at 273 K and 1 bar. The benzimidazole was formed in a one-step reaction between aldehyde-functionalized and diamine-functionalized monomers. The latter are synthetically not trivial to synthesize and tend to be air-sensitive. Furthermore, because the formation reaction is relatively irreversible, the obtained COFs were only moderately crystalline. However, this work inspired us to explore a similar linkage type for CO_2 -sorption: the thiazole linkage. As explained in **subsection 1.1.2**, this linkage can be obtained from imines via post-synthetic modification with elemental sulfur. In this chapter, we synthesize a novel thiazole-linked COF via post-synthetic modification, and compare its CO_2 uptake with the parent imine COF.

3.2 Synthesis and characterization

This work will focus on the linkage conversion for enhancement of CO_2 sorption. Nonetheless, we decided to start from an imine COF that already shows appreciable CO_2 sorption, in order to end with a material with as high a CO_2 uptake as possible. We figured that a highly-nitrogen rich COF would be a good starting point. The 1,2,4-triazole motif is a candidate of choice: this five-membered heterocyclic compound features three nitrogen sites which could act as adsorption sites for CO_2 .

The aldehyde monomer 4,4',4''-(tris((1,2,4)triazolo)-(1,3,5)-triazine-tribenzaldehyde (TTT) could be prepared in two steps starting from

commercially available 4-formylbenzonitrile and cyanuric chloride. We found the literature synthesis of this compound to be unsuccessful in our hands, and therefore modified the recipe [8]. The synthetic details are given in **subsection 3.5.1**. From this monomer, we prepared an imine-linked 2D covalent organic framework, via condensation with 1,3,5-tris(4-aminophenyl)benzene (TAPB) (**Figure 3.1**, **Figure 3.5A**). For the synthesis, we used again the protocol developed in **chapter 2**: stirring both monomers in a mixture of n-butanol, water and acetic acid for 16h at 70°C. After synthesis, the imine linkages in the TAPB-TTT COF were converted to thiazole linkages using a modification of the procedure based on the work of Haase et al. [9]. This simple method uses only cheap elemental sulfur (S_8) to selectively transform imines to thiazoles. The S_8 oxidizes the imine bond to a thioamide in a first step. It then cyclizes the formed thioamide group to yield the thiazole ring. We found that pursuing the reaction for a longer time at a lower temperature of 320 °C instead of the originally reported 350 °C yielded a more crystalline endproduct. The resultant COF was denoted as TAPB-TTT-S (**Figure 3.2**, **Figure 3.5B**). Details of the synthesis of TAPB-TTT and TAPB-TTT-S are given in the experimental section, **subsection 3.5.2**.

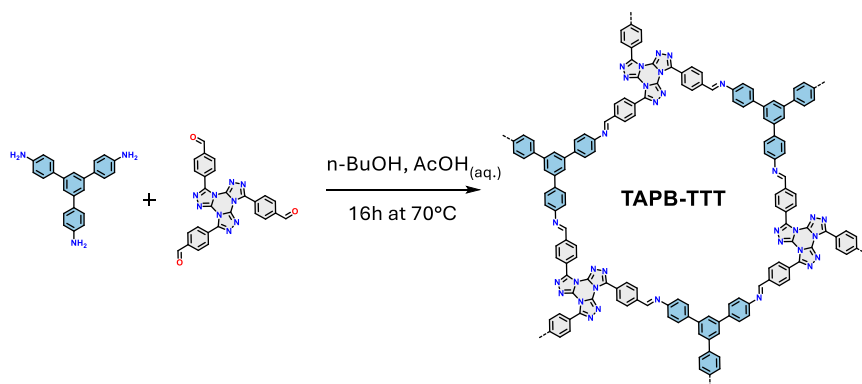


Figure 3.1. Synthesis of TAPB-TTT

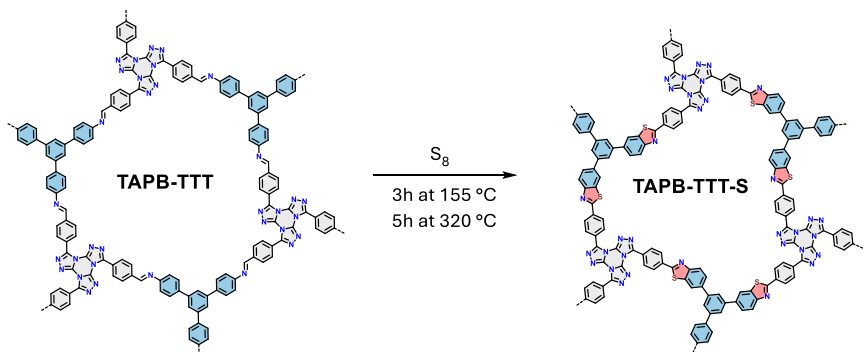


Figure 3.2. Synthesis of TAPB-TTT-S by post-synthetic modification of TAPB-TTT

The successful polymerization of the monomers TAPB and TTT to form the imine COF could be confirmed by FTIR spectroscopy (**Figure 3.3**). The characteristic aldehyde C=O vibration of TTT at 1696 cm^{-1} and amine N-H stretching vibrations TAPB at 3435 cm^{-1} and 3354 cm^{-1} have largely disappeared, while a new peak at 1626 cm^{-1} could be seen, indicative of the imine bond C=N stretching vibration. In TAPB-TTT-S, this vibration is no longer visible. The thiazole formation causes a shift of the C=N stretching to lower wavenumbers (usually around $1600\text{--}1610\text{ cm}^{-1}$), at which point it becomes hard to discern from the broad peak originating from the C=N vibrations in the tris(triazolo)triazine core. Further evidence of the formation of the thiazole ring in TAPB-TTT-S can be found in the new peaks at 1383 cm^{-1} and 814 cm^{-1} , ascribed to the thiazole C-S stretching and ring breathing vibrations respectively [10].

The crystalline structure of TAPB-TTT was confirmed by powder X-ray diffraction (PXRD). The obtained experimental patterns for TAPB-TTT show an intense peak at $2\theta = 3.8^\circ$, ascribed to the (100) reflection. Furthermore, weaker signals at 6.6° , 7.6° , 10.0° and 25.2° were visible, which correspond to the (110), (200), (210), and (001) reflections, respectively. These peaks correspond very well with the simulated pattern with AA

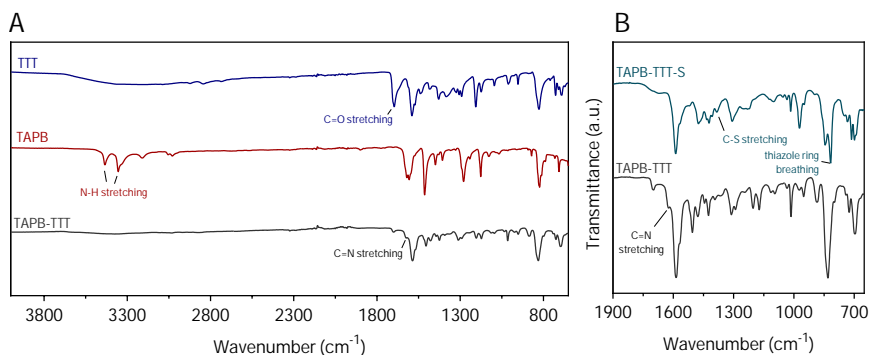


Figure 3.3. FTIR spectra of TTT, TAPB and TAPB-TTT (A); FTIR spectra of TAPB-TTT and TAPB-TTT-S (B)

stacking (**Figure 3.4**). TAPT-TTT then shows a hexagonal unit cell with an in-plane unit cell dimension of 26.9141 Å, and an interlayer stacking distance of 3.5699 Å. Pawley refinement further confirmed that this pattern is in good agreement with the theoretical structure (**Figure A.23**).

The PXRD pattern of TAPB-TTT-S, obtained after post-synthetic modification of TAPB-TTT, evidenced the crystalline nature of this thiazole-linked COF. The pattern was highly similar to that of TAPB-TTT, and agrees very well with the pattern simulated for a hexagonal thiazole-linked COF with AA stacking. The (100) peak shifts slightly to 3.9°, and the (110), (200), (210), and (001) shift correspondingly to 6.7°, 7.7°, 10.2° and 25.3°. The conversion of the imine bond to a five-membered thiazole ring leads to contraction of the unit cell, decreasing the a- and b-axis to 26.6581 Å. Meanwhile the increased conjugation in the layers enhances the π - π stacking, leading to a slightly smaller interlayer stacking distance of 3.466 Å. Further confirmation could again be obtained from Pawley refinement (**Figure A.23**).

Having established the crystalline nature and chemical composition of both COFs, we analyzed the permanent porosity of TAPB-TTT and TAPB-TTT-S by means of N₂-sorption at 77K. Both COFs showed a type

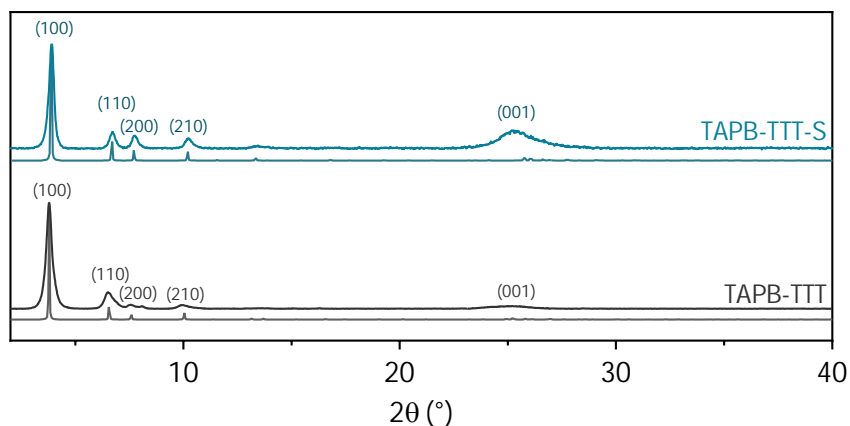


Figure 3.4. Experimental PXRD patterns of TAPB-TTT and TAPB-TTT-S. The simulated patterns for AA stacking are shown just below the experimental pattern in the same colour.

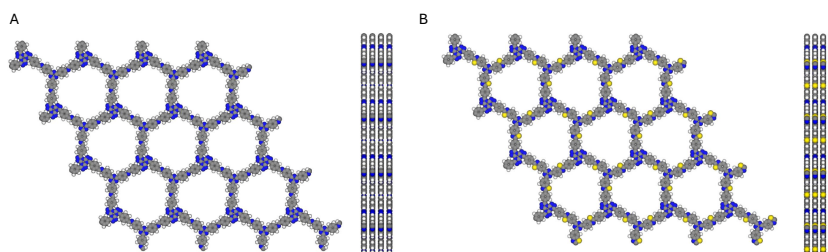


Figure 3.5. Simulated structures of TAPB-TTT (A) and TAPB-TTT-S (B)

IV isotherm, indicating their mesoporous nature (**Figure 3.6A**). The Brunauer-Emmett-Teller (BET) surface areas and pore volumes were calculated to be $1457 \text{ m}^2 \text{ g}^{-1}$ and $1323 \text{ m}^2 \text{ g}^{-1}$, while the total pore volumes (at $p/p_0 = 0.95$) were 0.85 ml g^{-1} and 0.80 ml g^{-1} respectively. The BET plots are shown in **Figure A.24**. We estimated the pore size distribution by means of quenched solid density functional theory (QSDFT), and obtained for TAPB-TTT an average pore size of 2.31 nm, in good agreement with the theoretical pore size from the simulated structure (2.33 nm). As observed in the PXRD patterns, the thiazole ring formation

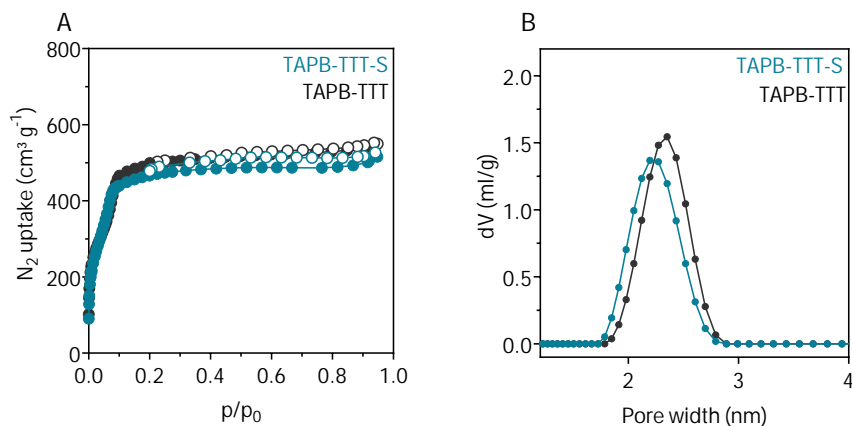


Figure 3.6. N₂-isortherms measured at 77K of TAPB-TTT and TAPB-TTT-S (A), pore size distributions of TAPB-TTT and TAPB-TTT-S (B)

leads to a contraction of the pore. This is also reflected in the pore size distribution of TAPB-TTT-S, which shows a maximum at around 2.18 nm, slightly smaller than the experimentally obtained maximum pore size of TAPB-TTT (**Figure 3.6B**).

Interestingly, we noted that the TAPB-TTT COF synthesized by using our protocol outlined in **chapter 2** showed significantly improved crystallinity and porosity over the same COF made by solvothermal synthesis according to Zhang et al. [8], despite using a lower reaction temperature and over four times shorter reaction time. Indeed, the FWHM of the (100) reflection of our COF was 0.327°, over % 30 lower than the FWHM of 0.514° obtained by their solvothermal synthesis. At the same time, the BET surface area of TAPB-TTT obtained by solvothermal synthesis was 1085 m² g⁻¹, more than 25% lower than the value of 1457 m² g⁻¹ we obtained. This again proves the wide applicability and the effectiveness of this method.

The conversion of imine to triazole could furthermore be confirmed by X-ray photoelectron spectroscopy (XPS) measurements. The N 1s spectrum of TAPB-TTT was deconvoluted in three peaks, at 402.1, 339.7

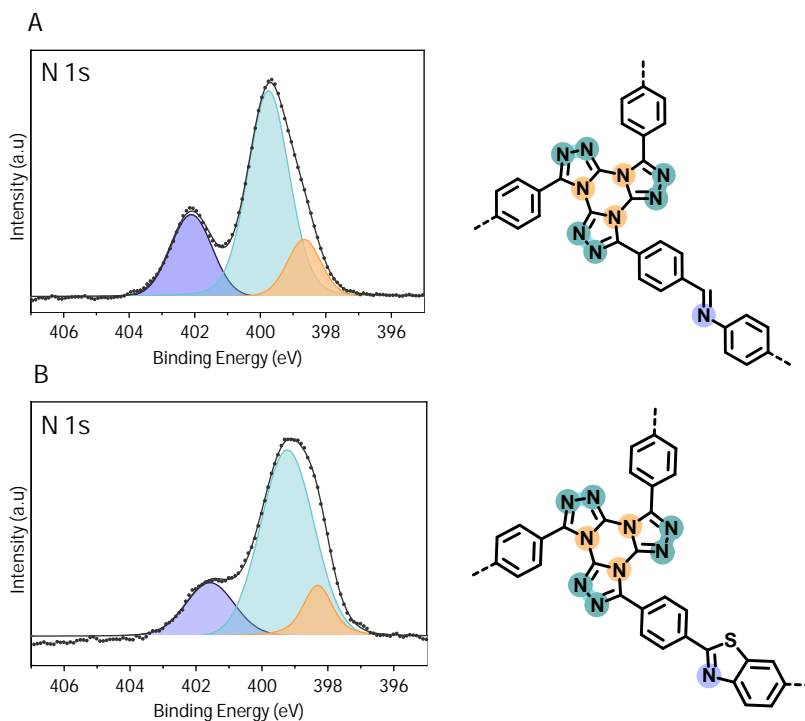


Figure 3.7. High-resolution XPS spectra of N 1s for TTT-TAPB (A) and TTT-TAPB-S (B). The deconvoluted peaks correspond in color to the chemical nitrogen species depicted on the right.

and 398.7 eV. These were assigned to the nitrogen from the imine linkages, the nitrogen from the triazole moieties in TTT, and nitrogen from the triazine core in TTT respectively. Upon conversion to thiazole, the peak for the nitrogen in the thiazole ring had shifted significantly to 401.5 eV, indicating the different electron density around the nitrogen atoms as a result of the different chemical environment.

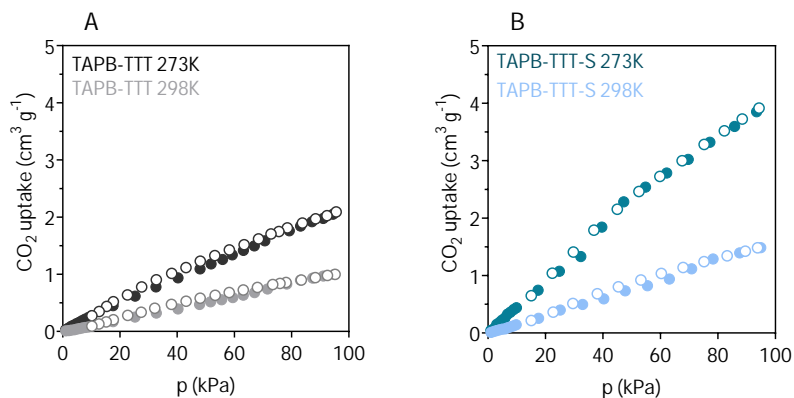


Figure 3.8. CO₂-sorption isotherms at 273 K and 298 K of TAPB-TTT (A) and TAPB-TTT-S (B)

3.3 CO₂ sorption performance

Next, we investigated the CO₂ sorption capacity of TAPB-TTT and TAPB-TTT-S. Owing to the presence of the highly nitrogen-rich tris(triazolo)triazine units, TAPB-TTT already displays a decent CO₂ uptake of 1.02 mmol g⁻¹ at 298 K, and 2.1 mmol g⁻¹ at 273 K. After the conversion of the imine linkages to the thiazole linkages, TAPB-TTT-S has an enhanced CO₂ uptake of 1.48 mmol g⁻¹ at 298 K, and 3.93 mmol g⁻¹ at 273 K, corresponding to an increase in CO₂ uptake with 45% at 298 K, and 87% at 273 K. These findings are in line with earlier articles which report that the incorporation of heteroatoms increases the CO₂-sorption capacity of COFs [11].

All isotherms show virtually no hysteresis, indicating that the high CO₂ can be ascribed to physisorption rather than chemisorption. We calculated the isosteric heat of adsorption (Q_{st}) for both COFs based on the Clausius-Clapeyron equation (**Figure A.26**). We obtained a (Q_{st}) of -28.44 kJ mol⁻¹ for TAPB-TTT, and an increased value of -32.16 kJ mol⁻¹ for TAPB-TTT-S. These Q_{st} values are in line with previously reported values for COFs [1].

3.4 Conclusion

In this chapter, we successfully demonstrated the conversion of the nitrogen-rich imine-linked COF TAPB-TTT to a thiazole-linked COF TAPB-TTT-s. The conversion was studied by FTIR, PXRD, N_2 -sorption and XPS. We show that the linkage conversion of imine-linked COFs to thiazole-linked COFs significantly enhances the CO_2 -sorption capacity, with an 87% increase in CO_2 -sorption at 1 bar and 273 K for TAPB-TTT-S compared to TABP-TTT. The isosteric heat of adsorption decreased from $-28.44 \text{ kJ mol}^{-1}$ to $-32.16 \text{ kJ mol}^{-1}$, demonstrating the enhanced affinity of the thiazole linkages compared to the imine linkage. Given the convenient synthetic procedure and wide scope of existing imine COFs, we envision that this strategy can be used in general to enhance the CO_2 -sorption capabilities of imine COFs.

3.5 Experimental

3.5.1 Monomer synthesis

4-(1H-tetrazol-5-yl)benzaldehyde 1.31 g 4-formylbenzonitrile (10 mmol), 780 mg sodium azide (12 mmol), and 200 mg $Cu(OAc)_2 \cdot 2H_2O$

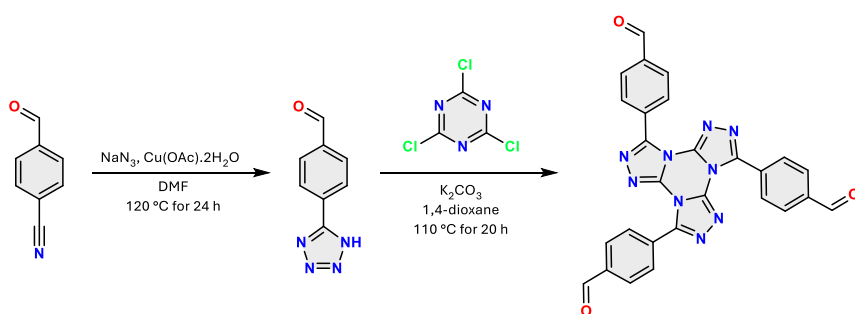


Figure 3.9. Synthesis of 4-(1H-tetrazol-5-yl)benzaldehyde and TTT

were added to a 20 mL Schlenk tube. 10 mL DMF was added, and the mixture was sparged with argon for 15 minutes. The headspace of the Schlenk tube was then flushed with argon, and the tube was closed, then heated at 120°C for 24 hours. After cooling to room temperature, the contents of the Schlenk tube were transferred to a 100 mL beaker, and 20 mL of a 5M HCl solution was added. This mixture was stirred for 30 minutes at room temperature. The obtained white precipitate was washed with water and methanol, then dried under vacuum for 16 hours. ¹H-NMR (DMSO-d₆) 10.10 (s, 1H), 8.26 (d, 2H), 8.14 (d, 2H).

4,4',4''-(tris((1,2,4)triazolo)-(1,3,5)-triazine-tribenzaldehyde (TTT) 870 mg 4-(1H-tetrazol-5-yl)benzaldehyde, 275 mg cyanuric chloride and 2780 mg K₂CO₃ were added to 40 mL dry dioxane. The mixture was sparged with argon for 15 minutes, then refluxed at 110°C under argon for 20 hours. After cooling down to room temperature, the off-white precipitate was filtered with water, methanol and acetone, then dried under vacuum for 16 hours. ¹H-NMR (DMSO-d₆) 10.18 (s, 93), 8.25 (d, 6H), 8.20 (d, 6H).

3.5.2 Synthesis of TAPB-TTT and TAPB-TTT-S

TAPB-TTT 31 mg TTT (~0.06 mmol) and 21 mg TAPB (~0.09 mmol) were added to a 4 mL glass vial containing an oblong teflon stirring bar with a length of 1 cm. 1.5 mL of a solution consisting of 1 mL n-butanol, 0.150 mL water and 0.350 mL glacial acetic acid was added. The vial was closed with a plastic screwcap, heated to 70°C in an aluminium heating block and stirred for 16 hours at 250 RPM. After cooling to room temperature, the obtained yellow slurry was filtered over a nylon filter of 0.45 μm pore diameter, washed with 10 mL H₂O, 10 mL DMF, 10 mL acetone, then 10 mL methanol. The powder was soaked in the solvent for 10 minutes each washing step. The resulting bright-yellow powder was dried at 90°C under vacuum for 16 hours (~94% yield).

TAPB-TTT-S For the post-synthetic modification of the imine linkage to the thiazole linkage, 20 mg of TAPB-TTT was thoroughly ground with ele-

mental sulfur for 5 minutes in an agate pestle and mortar. The resulting mixture was transferred to a glass ampoule, evacuated to 0.40 mbar for 5 minutes, and flamesealed under vacuum. The ampoule was heated in a muffle furnace. The temperature was first increased to 155°C over a period of two hours, then held at 155°C for 3 hours. Then, the temperature was increased to 320°C in 3 hours and held at this temperature for 5 hours, before cooling down to room temperature. The ampoule was opened, and the obtained brown monolith was soaked in 20 mL of chlorobenzene: *o*-dichlorobenzene in a 2:3 volume ratio at 120°C while stirring. The material was filtered over a nylon filter of 0.45 µm pore diameter, washed with methanol and acetone, and dried under vacuum for 16 hours.

3.5.3 Materials Characterization

Fourier Transform Infrared Spectroscopy (FT-IR) in the region of 4000 cm^{-1} to 650 cm^{-1} was recorded on a Thermo Nicolet™ iS50 FTIR Spectrometer with a diamond ATR in a frequency range from 4000 to 650 cm^{-1} Figure A.3. Powder X-ray diffraction (PXRD) patterns were collected on a Bruker D8 Advance diffractometer equipped with an autochanger and LynxEye XE-T Silicon strip Line detector, operated at 40 kV, 30 mA using $\text{Cu-K}\alpha$ radiation ($\lambda = 1.5406 \text{ \AA}$) in Bragg-Brentano geometry. The patterns were baseline corrected using the Bruker DIFFRAC.EVA software. $^1\text{H-NMR}$ spectra were collected on a Bruker Avance 300 at 300 MHz. The residual solvent signal at 7.26 ppm for CDCl_3 and at 2.50 ppm for $\text{DMSO-}d_6$ was used for chemical shift referencing. The surface chemical composition of the samples was investigated by X-ray photoelectron spectroscopy (XPS) using the PHI 5000 VersaProbe II spectrometer equipped with a monochromatic $\text{Al K}\alpha$ X-ray source ($h\nu = 1486.6 \text{ eV}$). To do so, the samples were excited with an X-ray beam (size: 200 μm) over an area of 500 x 500 μm^2 at a power of 50 W. Wide range survey scans and high-resolution spectra were recorded with a pass energy of 187.85 eV and 23.5 eV and a step size of 0.8 eV and 0.1 eV respectively. All spectra were

acquired at a take-off angle of 45° relative to the sample surface in the XPS chamber where the pressure was constantly maintained below 10⁻⁶ Pa. The high-resolution spectra were deconvoluted using Fityk 1.3.1. The spectra were background corrected using a Shirley baseline. The peaks were fitted to Pseudo-Voigt peak profiles. The fitting optimization was done using the Levenberg–Marquardt algorithm. Nitrogen sorption was performed at 77 K using a Micromeritics Tristar II. Samples were activated before measurement by heating at 120 °C for 16 hours under vacuum. Pore size distributions were determined using the calculation model for N₂ at 77 K on carbon (cylindrical/spherical pore, QSDFT adsorption branch model) of the ASiQwin software (v 1.27) from Quantachrome. Adsorption points are depicted as closed circles, while open circles are desorption points Figure A.4. The range for calculation of the BET surface area was chosen so that the following criteria were met:

1. The term $V_{ads}(1 - \frac{p}{p_0})$ must continuously increase with $\frac{p}{p_0}$
2. C must be positive
3. The value for R^2 must be equal to or greater than 0.995
4. The $\frac{p}{p_0}$ value corresponding to V_m must lie within the selected BET range.

CO₂ and N₂ sorption measurements at 273 K and 298 K were taken on a 3P Micro Flex 200, equipped with a cryoTune.

3.5.4 Structural Modelling

Pawley refinement of the PXRD patterns was carried out using the Reflex module of BIOVIA Materials Studio 2017 (17.1.0.48) (Dassault Systèmes, San Diego, 2017). The geometry optimized models of the COFs were used to provide starting unit cell parameters for refinement. The experimental PXRD patterns were refined from 2.0 to 40° in 2θ , and peaks were fitted to

Pseudo-Voigt peak profiles. The freely varying parameters set for the refinement were the full width at half maximum (FWHM) parameters U , V , W from the Caglioti formula (describing peak broadening), the profile parameters NA and NB (describing peak shape angle dependence), and the unit cell parameters a , b , c (while keeping atomic fractional coordinates fixed). The experimental background was modelled with a polynomial of degree 20. No corrections were made for line shift or peak asymmetry or broadening due to crystallite size, lattice strain, or preferred orientation. The theoretical maximum pore diameter was calculated from the simulated structure using Mercury Pore Analyser.

References

1. Li, H., Dilipkumar, A., Abubakar, S. & Zhao, D. Covalent organic frameworks for CO₂ capture: from laboratory curiosity to industry implementation. *Chemical Society Reviews* **52**, 6294–6329 (2023).
2. Guan, X., Li, H., Ma, Y., *et al.* Chemically stable polyarylether-based covalent organic frameworks. *Nature chemistry* **11**, 587–594 (2019).
3. Zhao, S., Dong, B., Ge, R., *et al.* Channel-wall functionalization in covalent organic frameworks for the enhancement of CO₂ uptake and CO₂/N₂ selectivity. *RSC advances* **6**, 38774–38781 (2016).
4. Popov, D. A., Luna, J. M., Orchanian, N. M., *et al.* A 2,2-bipyridine-containing covalent organic framework bearing rhenium (I) tricarbonyl moieties for CO₂ reduction. *Dalton Transactions* **47**, 17450–17460 (2018).
5. Liu, H., Chu, J., Yin, Z., *et al.* Covalent organic frameworks linked by amine bonding for concerted electrochemical reduction of CO₂. *Chem* **4**, 1696–1709 (2018).
6. Lyu, H., Li, H., Hanikel, N., Wang, K. & Yaghi, O. M. Covalent organic frameworks for carbon dioxide capture from air. *Journal of the American Chemical Society* **144**, 12989–12995 (2022).
7. Pyles, D. A., Crowe, J. W., Baldwin, L. A. & McGrier, P. L. Synthesis of benzobisoxazole-linked two-dimensional covalent organic frameworks and their carbon dioxide capture properties. *ACS Macro Letters* **5**, 1055–1058 (2016).
8. Liu, X., Zhang, Z., Zhang, Q., *et al.* Tris (triazolo) triazine-based Covalent Organic Frameworks for Efficiently Photocatalytic Hydrogen Peroxide Production. *Angewandte Chemie International Edition*, e202411546 (2024).
9. Haase, F., Troschke, E., Savasci, G., *et al.* Topochemical conversion of an imine-into a thiazole-linked covalent organic framework enabling real structure analysis. *Nature communications* **9**, 2600 (2018).

10. Deng, M., Sun, J., Laemont, A., *et al.* Extending the π -conjugation system of covalent organic frameworks for more efficient photocatalytic H₂O₂ production. *Green Chemistry* **25**, 3069–3076 (2023).
11. Chen, H., Qin, J., Ruan, X., *et al.* Linkage engineering of covalent-organic frameworks for CO₂ capture. *Separation and Purification Technology*, 129378 (2024).

Covalent Triazine Framework/Carbon Nanotube Hybrids as Electrocatalysts for the Reduction of CO₂

¹ ***Parts of this work have been published in:*** Andreas Laemont, Sara Abednatanzi, Parviz Gohari Derakshandeh, Florian Verbruggen, Erika Fiset, Qing Qin, Kevin Van Daele, Maria Meledina, Johannes Schmidh, Martin Oschatz, Pascal Van Der Voort, Korneel Rabaey, Markus Antonietti, Tom Breugelmans and Karen Leus "Covalent triazine framework/carbon nanotube hybrids enabling selective reduction of CO₂ to CO at low overpotential." *Green Chemistry* 22.10 (2020): 3095-3103.

4.1 Introduction

As mentioned in **subsection 1.2.3**, electrochemical reduction is one of the methods capable of generating several base chemicals, including carbon monoxide, formic acid and methane from CO₂. The electrochemical reduction of CO₂ can be conducted in aqueous media, which is a cheap, abundant and environmentally friendly way to facilitate the proton and electron transfer steps – although alternative electrolytes are being researched as well [1]. Furthermore, the reaction can be performed under atmospheric pressure and at room temperature. By changing reaction parameters such as the applied potential, electrolyte, electrocatalyst or pH, one can tune the product selectivity towards a desired endproduct and ensure a minimum of by-product formation. Finally, the electricity necessary to drive the reaction can be produced in a renewable manner.

A widespread industrial implementation however has so far not been realized. To achieve this, improvement of the catalyst cost, current density, overpotential and stability will be necessary [2–6]. The traditional (noble) metal-based catalysts are often expensive or suffer from a poor selectivity due to the competitive and kinetically favoured H₂ evolution side reaction, low electrochemical stability or need for high overpotentials [7]. To overcome these shortcomings, a new generation of metal-free electrocatalysts has recently been described, the majority of which is based on nitrogen-doped carbons. Promising findings have been reported proving metal-free catalysts can indeed compete with and in some cases even outperform their metal-based rivals [8–15]. An ideal electrocatalyst should exhibit a high and stable current density at a low overpotential, combined with excellent selectivity towards one specific endproduct.

In this chapter, we explore the use of covalent triazine frameworks (CTFs) as suitable candidates for the metal-free electrocatalytic reduction of CO₂. Based on the stable triazine ring as linkage unit, CTFs exhibit excellent thermal and (electro)chemical stability. This triazine linkage furthermore results in an inherent high amount of nitrogen present within the

CTF structure, which enhances the adsorption of CO₂. Through a rational selection of the linker, the nitrogen content can be even further increased, or another heteroatom can be introduced. This co-doping of nitrogen-doped carbons with elements such as sulphur, fluorine or boron has proven to ameliorate catalytic performance [16, 17]. The customary ionothermal synthesis of CTFs relies on the trimerization of nitrile-containing linkers at elevated temperatures (> 400° C) in the presence of ZnCl₂ as a Lewis acid catalyst [18]. This method yields stable, but amorphous materials, with partial carbonization and irreversible C-N bond formation due to the applied harsh synthesis conditions [19]. This leads to a significant amount of defects, which can be used as active sites for electrochemical CO₂. However, as we mentioned in subsection 1.2.3, the overall conductivity of CTFs is relatively low.

In this work a novel approach is introduced to overcome the conductivity issue of CTFs. We do this by constructing hybrid nanostructures, in which a layer of porous and N-rich CTF is grown onto highly conducting functionalized multiwalled carbon nanotubes (MWCNTs) (**Figure 4.3**). The porous nature of the CTF allows for efficient water and CO₂ transport, and its abundance of nitrogen sites promotes CO₂ adsorption and provides active sites for the reduction reaction. Meanwhile the electrons are efficiently conducted through the carbon nanotubes onto the CTF layer. The surface of the multiwalled nanotubes was modified earlier with hydroxyl groups to facilitate the growth of the CTF onto the nanotube and strengthen the contact between both materials, thus improving electron transfer between the two phases.

4.2 Synthesis of CTF@MWCNT hybrids

To ensure promote the growth of the CTF homogeneously over the multiwalled carbon nanotubes (MWCNTs), hydroxyl functionalities were introduced on its surface (**Figure 4.1**). This functionalization was achieved



Figure 4.1. Acidic oxidation of pristine MWCNTs, followed by reduction using NaBH₄, yields hydroxyl-functionalized carbon nanotubes (MWCNT-OH)

by acidic oxidation of the MWCNTs in a HNO₃ solution according to the reported method of Abednatanzi et al [20]. By applying this method, a variety of oxygen-containing species is introduced onto the surface of the nanotube, the majority being carboxyl- and hydroxyl groups. A subsequent chemical reduction with NaBH₄ converted most of the carboxyl groups into hydroxyl groups. A broad O-H stretching vibration around 3000-3500 cm⁻¹, a C=O stretching vibration around 1720 cm⁻¹ and a small O-H bending vibration at 1455 cm⁻¹ were observed in the FTIR spectrum of MWCNT-OH, indicating the presence of hydroxyl and carboxyl groups on the surface of the MWCNT Figure A.29. Quantitative XPS analysis indicated circa 3.96 at% of oxygen was present in MWCNT-OH (**Table A.4**).

In the next step, three different hybrid materials were synthesised. For the first material, denoted as CTF1@MWCNT-OH, terephthalonitrile was used as linker which contained no additional nitrogen other than the

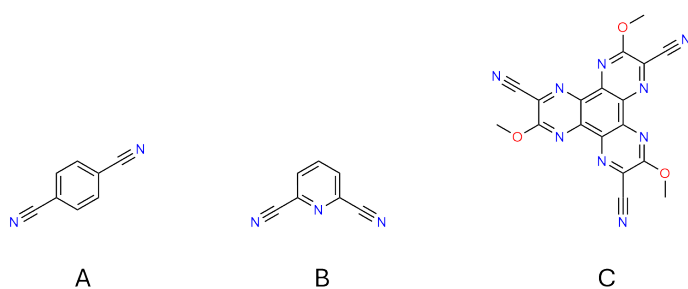


Figure 4.2. The used linkers: (a) terephthalonitrile, (b) pyridine-2,6-dicarbonitrile and (c) hexa-azatriphenylenetrimethoxytrinitrile

Sample	CTF1@ MWCNT-OH	pyCTF@ MWCNT- OH	HATCTF@ MWCNT-OH
linker	A	B	C
Amount (mg)	37.5	37.5	33
MWCNT-OH (mg)	75	75	66
ZnCl ₂ ratio	5:1	10:1	5:1
ZnCl ₂ (mg)	198	395	56
Temperature (° C)	400	500	500

Table 4.1. An overview of the synthesized hybrid materials under different reaction conditions

nitrogen present in the triazine rings. The two other hybrid materials, pyCTF@MWCNT-OH and HATCTF@MWCNT-OH, were built from 2,6-pyridinedicarbonitrile and hexa-azatriphenylenetrimethoxytrinitrile (HAT) respectively (**Figure 4.2**). These linkers both contain pyridinic nitrogen. Although this is still under debate, several authors have claimed that the pyridinic nitrogens are the most active sites for CO₂ reduction in nitrogen-doped carbons [13, 21]. These hybrid materials were synthesized using the ionothermal method, in which the terminal nitrile groups from three linkers fuse together in a cyclotrimerization reaction to form a triazine ring (**Figure A.27**). This trimerization reaction relies on the use of high temperatures (400 °C or 500 °C) depending on the choice of the linker, in the presence of MWCNT-OH and ZnCl₂. For comparison, the bulk HATCTF, pyCTF and CTF1 were also prepared under identical reaction conditions, but in the absence of the MWCNT-OH.

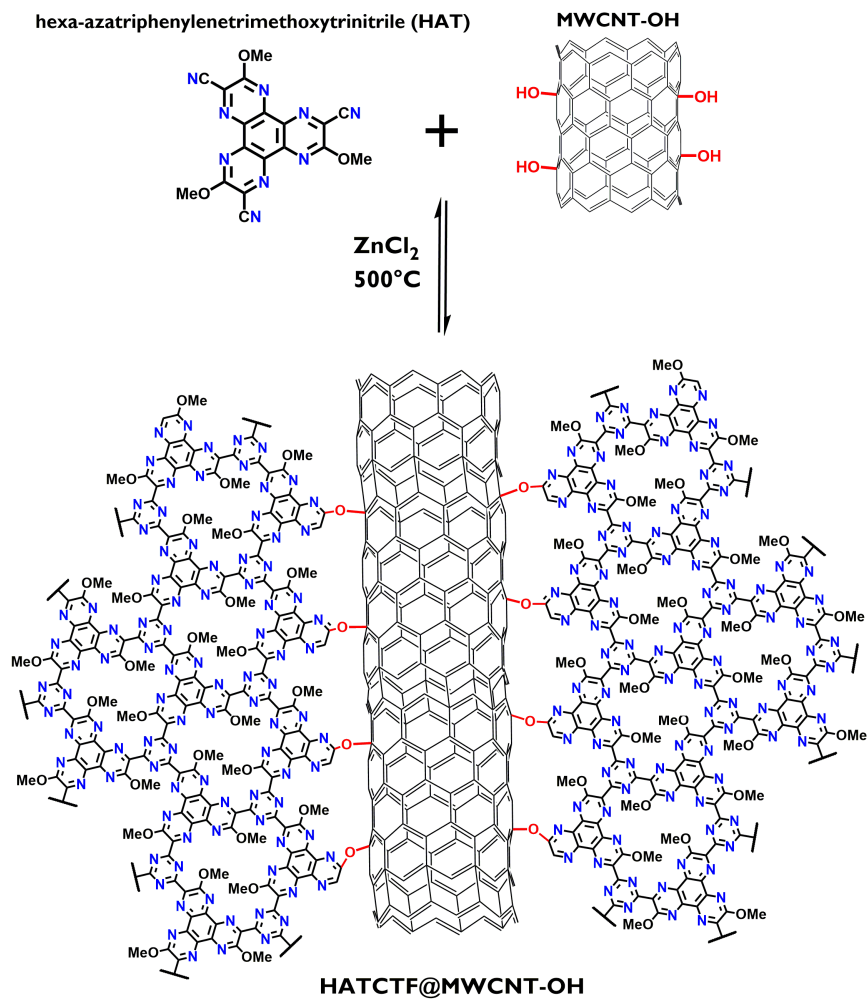


Figure 4.3. The synthesis of HATCTF@MWCNT-OH

4.3 Characterization of CTF@MWCNT hybrids

Elemental analysis indicated a significant increase in the nitrogen content of the hybrid materials in comparison to the pristine MWCNT-OH material which exhibited only 0.33 wt% of nitrogen (**Table 4.2**). The highest nitrogen content was observed for HATCTF@MWCNT-OH (8.27 wt%), followed by pyCTF@MWCNT-OH (6.57 wt%) and CTF1@MWCNT-OH which has a nitrogen content of 3.33 wt%.

DRIFTS measurements of the pristine CTFs showed two broad peaks around 1570 cm^{-1} and 1350 cm^{-1} which we ascribed to the triazine ring vibrations (**Figure A.28**). As the hybrid materials strongly absorb IR light, little structural information could be derived from their DRIFTS spectra (**Figure A.30**).

A comparison of the PXRD patterns of the MWCNT-OH, HATCTF and HATCTF@MWCNT-OH is depicted in **Figure 4.4A**. For all the CTF-based materials a broad (001) diffraction around $2\theta = 26^\circ$ is observed which can be attributed to a vertical spacing between the stacked sheets of 3.35 \AA [22]. A diffraction at a similar angle is seen in the pristine MWCNT-OH material, which corresponds to the (002) diffraction coming from the interlayer distance between the different concentric single-walled carbon nanotubes that make up a multiwalled carbon nanotube. In addition to this, the MWCNT-OH shows another diffraction at approximately 43° , which can be assigned to the (100) and (101) diffractions in the coiled carbon sheets of the carbon nanotubes [23]. This

Name	S_{BET} ($\text{m}^2\text{ g}^{-1}$)	V_{m} (cm^3/g)	N (wt%)	C (wt%)	H (wt%)
MWCNT-OH	263	1.58	0.33	91.92	0.14
CTF1@MWCNT-OH	323	0.34	3.33	87.52	0.70
pyCTF@MWCNT-OH	496	0.41	6.57	77.47	0.66
HATCTF@MWCNT-OH	290	0.76	8.27	81.74	0.67

Table 4.2. Elemental analysis, S_{BET} and pore volume of MWCNT-OH and the hybrid materials.

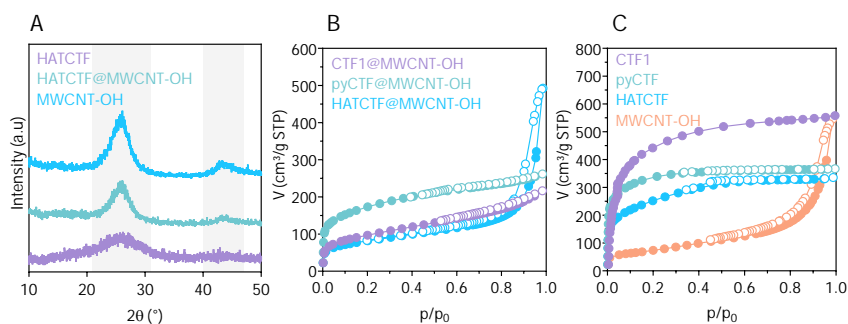


Figure 4.4. PXRD patterns of HATCTF, HATCTF@MWCNT-OH and MWCNT-OH (A), N₂-sorption isotherms of CTF1@MWCNT-OH, pyCTF@MWCNT-OH and HATCTF@MWCNT-OH (B), N₂-sorption isotherms of CTF, pyCTF, HATCTF and MWCNT-OH (C).

diffraction is not observed in the bulk HATCTF material, but is clearly present in the hybrid HATCTF@MWCNT-OH. The PXRD patterns of CTF1, pyCTF, CTF1@MWCNT-OH and pyCTF@MWCNT-OH can be found in **Figure A.31**.

Further elucidation of the formation of the hybrid materials was found by means of N₂-physisorption measurements (**Figure 4.4B, C**). The bulk CTF materials exhibit a type I isotherm, typical for a microporous material. The functionalized carbon nanotubes on the other hand exhibit a type IV isotherm: in between the randomly entangled carbon nanotubes are voids, where capillary condensation can take place at a p/p_0 values close to one. The isotherm of the HATCTF@MWCNT-OH exhibits both microporosity and capillary condensation, but to a lesser extent than what is observed in the MWCNT-OH material. We believe that the voids between the carbon nanotubes are filled with CTF. For the pyCTF-MWCNT-OH and CTF1-MWCNT-OH material, capillary condensation is no longer observed at all. A possible explanation lies in the significant difference in molecular weight of the linkers: 128 g/mol and 129 g/mol for terephthalonitrile and 2,6-pyridinedicarbonitrile respectively, versus 399 g/mol for hexa-azatriphenylenetrimethoxytrinitrile. Because for all

materials an equal weight ratio of 1:2 linker to MWCNT-OH was used, the pyCTF@MWCNT-OH and CTF1@MWCNT-OH reaction mixtures contain a larger molar amount of CTF as compared to HATCTF@MWCNT-OH, enough to entirely fill the voids between the multiwalled carbon nanotubes. The molar amount of hexa-azatriphenylenetrिमथoxytrinitrile is not sufficient to result in enough COF to entirely fill the mesoporic voids between the carbon nanotubes with HATCTF.

This theory is supported by the changes in the BET surface area and total pore volume for the hybrid materials as compared to MWCNT-OH (**Table 4.2**). For HATCTF@MWCNT-OH, the decrease in total pore volume is less pronounced than for pyCTF@MWCNT-OH and CTF1@MWCNT-OH. On the other hand, the increase in surface area for the hybrid materials is smaller for HATCTF@MWCNT-OH in comparison to the other hybrid materials. The filling of the mesoporic carbon nanotubes voids by the CTF causes the overall pore volume to decrease, but the BET surface area to increase, with both effects being more pronounced as a higher amount of CTF is present.

A combination of ADF-STEM imaging with EDX elemental mapping was used to investigate the morphology and chemical composition of the MWCNT-OH and the hybrid materials. **Figure A.32** contains the EDX spectrum and a HR ADF-STEM image of the multiwalled nanotubes

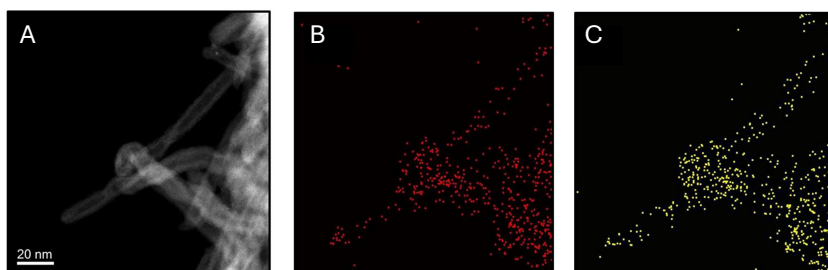


Figure 4.5. ADF-STEM image of nanotubes in the HATCTF@MWCNT-OH material showing the mapped area (A) together with EDX elemental maps for oxygen (B) and nitrogen (C)

functionalised with –OH groups. A clear oxygen signal is detected for the material and the oxygen distribution correlates well to the carbon distribution evidencing the homogeneous –OH functionalisation of the carbon nanotubes. The MWCNT-OH retained the classical multiwalled morphology .

Figure 4.5A shows an ADF-STEM image of HATCTF@MWCNT-OH, while **Figure 4.5B, C** show the correlating presence of respectively oxygen and nitrogen in HATCTF@MWCNT-OH, indicating the growth of nitrogen-rich HATCTF onto the carbon nanotube surface via oxygen linkages. This is evidencing the CTF presence in and around the nanotubes rather than a separate nitrogen-containing CTF phase mixing with nanotubes. No secondary phases were observed, also indicating the decoration of the MWCNT-OH by the HATCTF and creation of a true hybrid material.

In **Figure A.33**, the ADF-STEM image showing the mapped area together with elemental maps, EDX spectrum and HR ADF-STEM image of a single nanotube for the pyCTF@MWCNT-OH material are depicted. The EDX spectrum contains clear peaks of both nitrogen and carbon. The distribution of oxygen and nitrogen signals again are in agreement, revealing the homogeneous growth of CTF on the multiwalled nanotubes.

As a result of the high reaction temperature during synthesis, partial carbonization and irreversible C–C and C–N bond formation of the CTF materials occurs. This gives rise to different nitrogen species within the structure (**Figure 4.6**) [19]. XPS analysis of the hybrid materials indicated the presence of four distinct types of nitrogen: pyridinic-like nitrogen

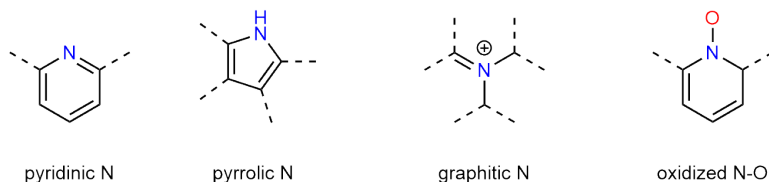


Figure 4.6. The four species of nitrogen encountered in the hybrid materials.

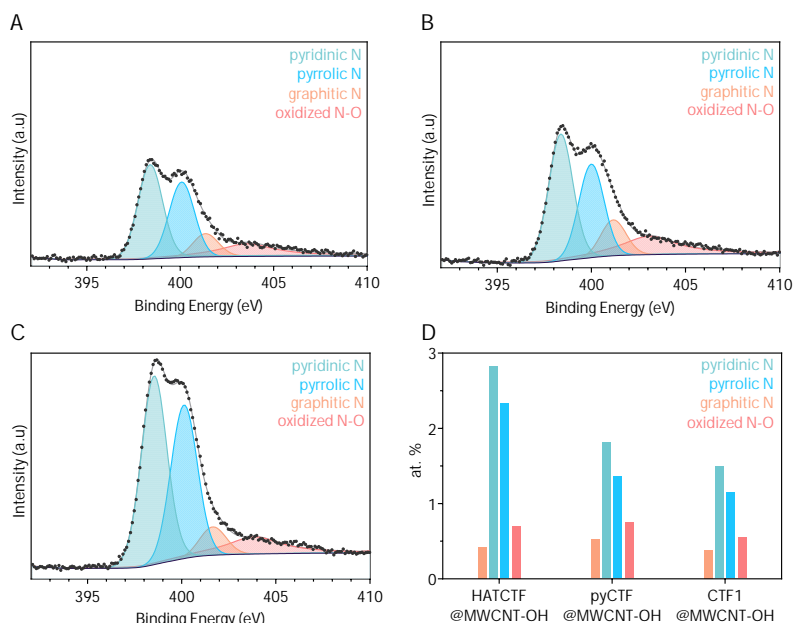


Figure 4.7. Deconvoluted XPS spectrum of the N1S peak of CTF1@MWCNT-OH (A), deconvoluted XPS spectrum of the N1S peak of pyCTF@MWCNT-OH (B), deconvoluted XPS spectrum of the N1S peak of HATCTF@MWCNT-OH (C), atomic nitrogen distribution of HATCTF@MWCNT-OH, pyCTF@MWCNT-OH and CTF1@MWCNT-OH (D)

(which includes the nitrogen in the triazine rings), pyrrolic-like nitrogen, graphitic nitrogen and oxygenated N-O species (**Figure 4.7A, B, C**). Despite the different linker, the nitrogen distribution of pyCTF@MWCNT-OH and CTF1@MWCNT-OH show a very similar trend (**Figure 4.7D**). The HATCTF@MWCNT-OH on the other hand is significantly richer in pyridinic and pyrrolic nitrogen, most likely as a result of the linker, which is rich in pyridinic nitrogen.

4.4 Electrocatalytic performance CTF@MWCNT hybrids

To test their electrocatalytic performance, each hybrid material was coated onto a glassy carbon electrode with a loading of ca. 1 mg/cm². The activity for the CO₂ reduction of the hybrid materials was examined by linear sweep voltammetry (**Figure A.35**) and by 1800 second chronoamperometry tests at different potentials in a range of -0.5 V to -0.9 V vs. RHE. The average current density at the last 200 seconds of the chronoamperometry is plotted versus the applied potential in **Figure 4.8A** for each hybrid material. At every measured potential an increase in current density was observed for HATCTF@MWCNT-OH in CO₂-saturated 0.1 M KHCO₃ as compared to the same electrolyte sparged with argon, indicating the occurrence of electrochemical CO₂ reduction (**Figure 4.8C**). Online GC analysis of the cell headspace during 1800 second chronoamperometry experiments confirmed this: CO and H₂ could be detected during the reaction in the CO₂-saturated 0.1 M KHCO₃ electrolyte at potentials as high as -0.5 V.

The Faradaic Efficiency (FE) for CO in the range of -0.5 V to -0.9 V for all materials is shown in **Figure 4.8B** and is maximal at the highest tested potential of -0.5 V. The rate of the competing hydrogen evolution reaction increases with decreasing potential. For all the hybrid materials, the FE for CO generation was maximal at -0.5 V, corresponding to an overpotential of circa 380 mV [7]. A clear correlation between the nitrogen content and the maximal FE at -0.5 V can be noted: while the nitrogen-poor CTF1@MWCNT-OH only produces 41% CO, pyCTF@MWCNT-OH and HATCTF@MWCNT-OH (containing 6.57 wt% and 8.27 wt% nitrogen respectively) generate 60% and 81% CO respectively. Upon shifting to more negative potentials, the CO generation decreased, while at the same time more H₂ was detected by the GC, meaning that lower potentials will foster hydrogen evolution at the cost of CO₂ reduction.

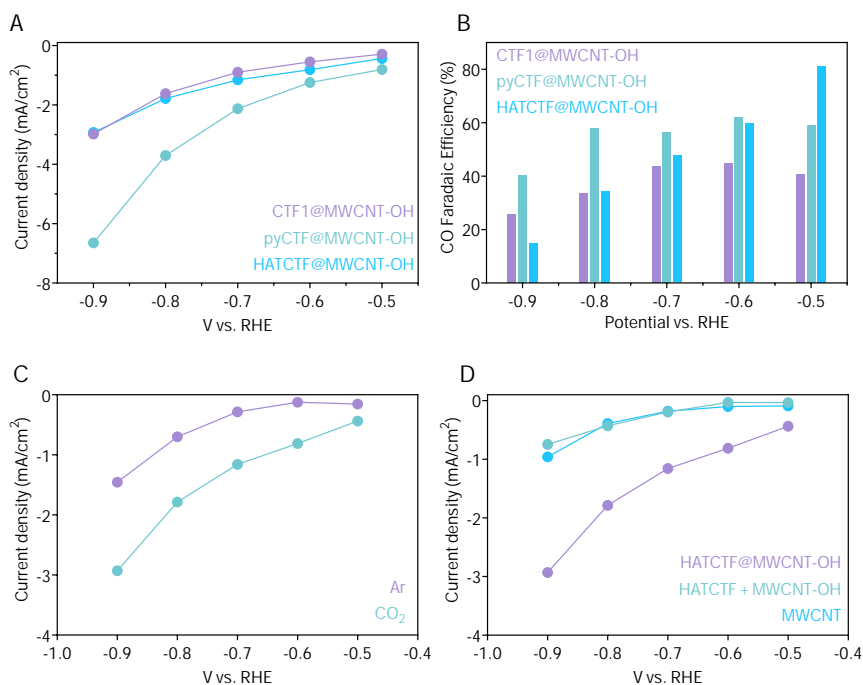


Figure 4.8. Total geometric current densities of the hybrid materials (A), Faradaic Efficiencies for CO of the hybrid materials (B), geometric current density of HATCTF@MWCNT-OH in Ar-sparged 0.1 M KHCO₃ and CO₂-saturated 0.1 M KHCO₃ (C), geometric current density for HATCTF@MWCNT-OH compared to HATCTF+MWCNT-OH and MWCNT in CO₂-saturated 0.1 M KHCO₃ (D)

The shift from CO to H₂ production happens almost linearly with increasingly negative potential in HATCTF@MWCNT-OH. In CTF1@MWCNT-OH and pyCTF@MWCNT-OH however, the FE for CO decreases less steep. These results can be explained by the observations made by N₂-sorption: HATCTF@MWCNT-OH contains a lower molar ratio of CTF to carbon nanotubes as compared to pyCTF@MWCNT-OH and CTF1@MWCNT-OH. As carbon nanotubes are known to catalyze hydrogen evolution [24], the relatively larger amount of it present in HATCTF@MWCNT-OH will more effectively promote hydrogen evolution at more negative poten-

tials. Interestingly, the current densities of HATCTF@MWCNT-OH and CTF@MWCNT-OH are very similar while pyCTF@MWCNT-OH shows more electrochemical activity at every potential (**Figure 4.8A**). This trend does not agree with the nitrogen content as detected by XPS or elemental analysis, but does correlate with the BET surface area: whereas HATCTF@MWCNT-OH and CTF@MWCNT-OH show a comparable BET surface area of around $300 \text{ m}^2 \text{ g}^{-1}$, the increased BET surface area (almost $500 \text{ m}^2 \text{ g}^{-1}$) of pyCTF@MWCNT-OH might explain the enhanced activity of this catalyst.

In order to prove the importance of the chemical bonding between the CTF and the carbon nanotube, an electrocatalytic test was performed in which a physical mixture of HATCTF and MWCNT-OH was used as catalyst. More specifically, HATCTF and MWCNT-OH were mixed together in a mortar in a 1:2 weight ratio, denoted as HATCTF+MWCNT-OH. While this sample also contains CTF and MWCNT-OH in the same weight ratio, they are not fused together, as is the case for HATCTF@MWCNT-OH (**Figure A.36**). The activity of HATCTF+MWCNT-OH is way smaller than that of HATCTF@MWCNT-OH at every potential (**Figure 4.8D**). Hydrogen gas was found to be the main product at -0.8 and -0.9 V. Note that at potentials of -0.7 V or higher, the concentration of evolved gasses was below the detection limit of the online GC. Even assuming the unlikely scenario of 100% FE towards CO at -0.5 V for HATCTF+MWCNT-OH, this would still mean the CO current density at -0.5 V of this sample is decreased by more than a factor 10 as compared to the HATCTF@MWCNT-OH.

It is important to mention that impurities of Mn, Fe, Cu and Zn were detected in HATCTF@MWCNT-OH via ICP-MS analysis (**Table A.5**). Mn, Fe and Cu are residual impurities from the synthesis of the carbon nanotubes, while Zn can be ascribed to the ZnCl_2 used for the synthesis of HATCTF. Despite extensive washing efforts we did not succeed in removing these impurities without destroying the catalyst. For these reasons, the catalysts described above cannot strictly be called metal-free. However, two control experiments were undertaken that prove that these

impurities are not the source of electrochemical activity for conversion of CO₂ to CO. Consecutive chronoamperometries of the pristine multiwalled carbon nanotubes showed that this material exhibits a much lower electrochemical activity, despite also containing metal impurities (**Figure 4.8D**). Online GC detected H₂ as the only gaseous endproduct. As mentioned above, another control experiment was undertaken in which carbon nanotubes were physically mixed but not thermally hybridized with HATCTF, in the same weight ratio as the composition of the catalyst (**Figure 4.8D**). Again, a much smaller current density was detected, however this time also some CO was formed. The combined results of these experiments prove that the activity towards CO generation originates from the CTF, and that hybridization with the carbon nanotubes greatly improves the overall activity of the catalyst.

4.5 Conclusion

An in situ growth strategy successfully yielded hybrid materials, composed of a layer of CTF grown on functionalized multiwalled carbon nanotubes. The hybrid materials were capable of selective electrochemical conversion of CO₂ to CO. The best results were obtained with HATCTF@MWCNT-OH, achieving 81 % FE at the very low overpotential of 380 mV and with a total current density of -0.48 mA cm⁻². At this overpotential, the HATCTF@MWCNT-OH shows at least a tenfold increase in CO generation activity as compared to a physical mixture of the HATCTF and MWCNT-OH. This observation indicates that the reported novel hybridization method is indeed a viable strategy to convert poorly conductive CTFs into functional electrocatalysts, whilst retaining their structural and chemical properties. XPS analysis indicated that the bottom-up synthesis strategy of CTFs offers some degree of control over the nature of the active sites via an adequate choice of linker.

4.6 Experimental

4.6.1 Linker Synthesis

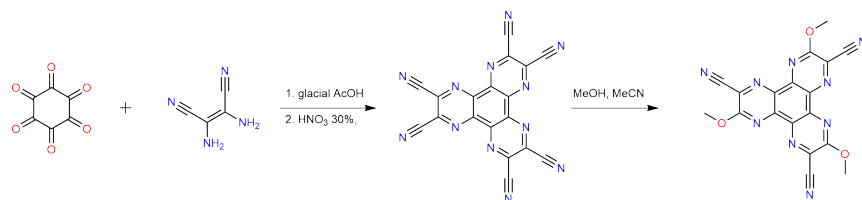


Figure 4.9. Synthesis of hexa-azatriphenylenetrimethoxynitrile (HAT)

HAT-(CN)₆ Hexa-azatriphenylenehexacarbonitrile, HAT-(CN)₆ was synthesized according to the published procedure of Czarnik et al [25]. For the synthesis of HAT-(CN)₆, hexaketocyclohexane octahydrate (4 g, 12.6 mmol) and diaminomaleonitrile (10.88 g, 100.8 mmol) were refluxed in glacial acetic acid (150 mL) for 2 h. The black suspension was filtered off while hot and washed with hot glacial acetic acid (3 × 25 mL) resulting in a black solid. The solid was suspended in 30 % HNO₃ (60 mL) and heated at 100 ° C for 3 h. The hot dark brown suspension was poured into ice water (200 mL) and cooled overnight. The suspension was filtered and the solid was refluxed in acetonitrile (400 mL) for 2 h and was filtered. The filtrate was evaporated under vacuum to give an orange solid (2.4 g, yield 50 %).

HAT HAT-(CN)₆ (700 mg) was dissolved in acetonitrile (40 mL) followed by the addition of 30 mL methanol, as reported by Chang et al [26]. The reaction mixture was refluxed for 50 hours at 85° C, and left to stand overnight at room temperature. The formed yellow precipitate was filtered. A further crop of product was obtained by adding a few drops of NaOMe to the collected filtrate, until a new precipitation started. The solution was left to stand for an additional 48 hours to precipitate further. The precipitate was filtered, washed extensively with methanol and water, and dried under vacuum overnight. ¹H-NMR (CDCl₃ 4.49 (s, 9H).

4.6.2 Synthesis of MWCNT-OH

Multiwalled carbon nanotubes (MWCNTs) were obtained from Nanocyl SA and used without further purification. For the functionalization of the nanotubes, 1g of MWCNTs was refluxed for 24 hours at 120° C in a 100 ml of a 5M nitric acid solution. The product was filtered through a nylon filter (0.45 μm), washed with water until the filtrate was pH-neutral, and dried overnight under vacuum. Afterwards, the MWCNT-COOH-OH material was dispersed in 100 mL methanol in a round bottom flask and placed in an ice bath. 5 g of sodium borohydride was added slowly under continuous stirring. After stirring for 24 hours at room temperature, the product was filtered through a nylon filter (0.45 μm), washed with water until the filtrate was pH-neutral and dried overnight under vacuum.

4.6.3 Synthesis of CTF@MWCNT-OH hybrid materials

Terephthalonitrile, pyridine-2,6-dicarbonitrile or hexa-azatrimethoxytrinitrile, was thoroughly ground in a mortar in the presence of a twofold mass amount of MWCNT-OH. Hereafter, the solid mixture was placed in a glass ampoule, together with an appropriate amount of ZnCl₂. Prior to use, the ZnCl₂ catalyst was dried at 120° C under vacuum for at least 24 hours. Next, the ampoule was degassed for at least 4 hours, and flame-sealed. For the linkers terephthalonitrile and hexa-azatrimethoxytrinitrile a 5:1 molar ratio of ZnCl₂ to linker was used, while for the pyridine-2,6-dicarbonitrile linker a 10:1 molar ratio was used. The glass ampoules were heated to 500° C (for the pyCTF@MWCNT-OH and HATCTF@MWCNT-OH material) or to 400° C (for the CTF1@MWCNT-OH), and kept at this temperature for 48 hours. After cooling down, the glass ampoules were opened, and the obtained black solids were refluxed in 1M HCl at 110° C to remove residual ZnCl₂. After 24 hours, the solids were filtered through a nylon filter membrane (0.45 μm), and washed with water until the filtrate was pH-neutral. Finally, the hybrid materials were stirred for 24 hours in THF at room

temperature, filtered through a nylon filter (0.45 μm), washed with THF and acetone, and afterwards dried overnight under vacuum.

4.6.4 Materials Characterization

Nitrogen sorption analysis was conducted at 77 K using a Belsorp-Mini II gas analyzer. Prior to the sorption measurements, the samples were dried under vacuum at 120 °C overnight. Specific surface areas were calculated based on Brunauer–Emmett–Teller (BET) analysis. Total pore size was calculated based on Barrett-Joyner-Halenda (BJH) analysis. Elemental analysis was measured on a Thermo Scientific Flash 2000 CHNS-O analyzer equipped with a TCD detector. Powder X-ray diffraction (PXRD) patterns were collected on a Thermo Scientific ARL X'Tra diffractometer, operated at 40 kV, 40 mA using Cu-K α radiation (1.540 Å). X-ray photoelectron spectroscopy (XPS) measurements were performed on a Thermo Fisher Scientific Escalab 250 Xi. Annular dark field scanning transmission electron microscopy (ADF-STEM) and energy dispersive X-Ray (EDX) spectroscopy experiments were carried out using a FEI Titan transmission electron microscope operated at an accelerating voltage of 200 kV and equipped with a probe spherical aberration corrector unit and a Super-X EDX system. The samples were prepared by dispersing powder samples in ethanol and dropping the dispersion onto a carbon coated TEM copper grid.

Electrochemical performance

The electrochemical performance of the different CTF@MWCNT-OH materials was examined in a gas tight electrochemical cell (H-type configuration), featuring two compartments, divided by a proton-permeable Nafion 117 membrane. The cathodic chamber with the glassy carbon working electrode (WE) was filled with 0.1 M KHCO₃, saturated with CO₂ (pH = 6.70) in the presence of the Ag/AgCl reference electrode. The

anodic chamber was filled with an unsaturated 0.1 M KHCO₃ solution in the presence of a platinum counter electrode. The cell was kept at a constant temperature of 18° C by means of water cooling. The WE, counter electrode and reference electrode were coupled to a PARSTAT 4000 potentiostat while the cell headspace was connected to a Thermo-Fisher Scientific TRACE™ 1300 Gas Chromatograph equipped with a TCD detector. The Faradaic efficiencies were calculated based on the online GC measurements of the gaseous endproducts H₂ and CO during chronoamperometry according to the following equation:

$$FE = \frac{znF}{Q}$$

In which *z* is the number of electrons exchanged to form one molecule of the desired product (in the case of CO and H₂, *z* = 2), *n* is the molar amount of endproduct formed measured via GC, *F* is the Faraday constant and *Q* is the total charge generated during the process in the time up until the sample injection. Since no gaseous products other than CO and H₂ were detected by means of GC and no liquid products were detected with NMR and HPLC the total Faradaic efficiency was normalized to 100%.

The WE consisted of a glassy carbon rod with a base of 0.2 cm², embedded in epoxy in such a way that only the ground plane is available for reaction. The surface was mechanically polished using alumina particles slurry before every reaction to a roughness of 0.05 μm. For each hybrid material, a catalyst ink was prepared, which consisted of 2 mg CTF@MWCNT-OH, 195 μl isopropanol, and 5 μl Nafion 117 solution (5 wt% in a mixture of lower alcohols). This ink was sonicated for at least one hour to obtain a good dispersion before usage. 20 μl of the ink was dropcasted onto the glassy carbon electrode surface of 0.2 cm² in four steps of 5 μl, resulting in a catalyst loading of ca. 1 mg/cm². After coating, the electrode was dried overnight in a closed container before usage.

References

1. Sharma, P. P. & Zhou, X.-D. Electrocatalytic conversion of carbon dioxide to fuels: a review on the interaction between CO₂ and the liquid electrolyte. *Wiley Interdisciplinary Reviews-energy And Environment* **6** (2017).
2. Jouny, M., Luc, W. & Jiao, F. General Techno-Economic Analysis of CO₂ Electrolysis Systems. *Industrial & Engineering Chemistry Research* **57**, 2165–2177 (2018).
3. Spurgeon, J. M. & Kumar, B. A comparative technoeconomic analysis of pathways for commercial electrochemical CO₂ reduction to liquid products. *Energy & Environmental Science* **11**, 1536–1551 (2018).
4. Verma, S., Kim, B., Jhong, H.-R. M., Ma, S. & Kenis, P. J. A. A Gross-Margin Model for Defining Technoeconomic Benchmarks in the Electroreduction of CO₂. *Chemsuschem* **9**, 1972–1979 (2016).
5. Song, Q.-W., Zhou, Z.-H. & He, L.-N. Efficient, selective and sustainable catalysis of carbon dioxide. *Green Chemistry* **19**, 3707–3728 (2017).
6. Yu, B., Zou, B. & Hu, C.-W. Recent applications of polyoxometalates in CO₂ capture and transformation. *Journal Of CO₂ Utilization* **26**, 314–322 (2018).
7. Zhang, W., Hu, Y., Ma, L., *et al.* Progress and Perspective of Electrocatalytic CO₂ Reduction for Renewable Carbonaceous Fuels and Chemicals. *Advanced Science* **5** (2018).
8. Wu, J., Ma, S., Sun, J., *et al.* A metal-free electrocatalyst for carbon dioxide reduction to multi-carbon hydrocarbons and oxygenates. *Nature Communications* **7** (2016).

9. Chen, Z., Mou, K., Yao, S. & Liu, L. Highly selective electrochemical reduction of CO₂ to formate on metal-free nitrogen-doped PC61BM. *Journal Of Materials Chemistry A* **6**, 11236–11243 (2018).
10. Yang, H., Wu, Y., Lin, Q., *et al.* Composition Tailoring via N and S Co-doping and Structure Tuning by Constructing Hierarchical Pores: Metal-Free Catalysts for High-Performance Electrochemical Reduction of CO₂. *Angewandte Chemie-international Edition* **57**, 15476–15480 (2018).
11. Liu, Y., Chen, S., Quan, X. & Yu, H. Efficient Electrochemical Reduction of Carbon Dioxide to Acetate on Nitrogen-Doped Nanodiamond. *Journal Of The American Chemical Society* **137**, 11631–11636 (2015).
12. Kumar, B., Asadi, M., Pisasale, D., *et al.* Renewable and metal-free carbon nanofibre catalysts for carbon dioxide reduction. *Nature Communications* **4** (2013).
13. Wang, H., Jia, J., Song, P., *et al.* Efficient Electrocatalytic Reduction of CO₂ by Nitrogen-Doped Nanoporous Carbon/Carbon Nanotube Membranes: A Step Towards the Electrochemical CO₂ Refinery. *Angewandte Chemie-international Edition* **56**, 7847–7852 (2017).
14. Mou, S., Wu, T., Xie, J., *et al.* Boron Phosphide Nanoparticles: A Nonmetal Catalyst for High-Selectivity Electrochemical Reduction of CO₂ to CH₃OH. *Advanced Materials* **31** (2019).
15. Cui, W., Liu, Q., Cheng, N., Asiri, A. M. & Sun, X. Activated carbon nanotubes: a highly-active metal-free electrocatalyst for hydrogen evolution reaction. *Chemical Communications* **50**, 9340–9342 (2014).

16. Yang, L., Jiang, S., Zhao, Y., *et al.* Boron-Doped Carbon Nanotubes as Metal-Free Electrocatalysts for the Oxygen Reduction Reaction. *Angewandte Chemie-international Edition* **50**, 7132–7135 (2011).
17. Xie, J., Zhao, X., Wu, M., *et al.* Metal-Free Fluorine-Doped Carbon Electrocatalyst for CO₂ Reduction Outcompeting Hydrogen Evolution. *Angewandte Chemie-international Edition* **57**, 9640–9644 (2018).
18. Kuhn, P., Antonietti, M. & Thomas, A. Porous, covalent triazine-based frameworks prepared by ionothermal synthesis. *Angewandte Chemie-international Edition* **47**, 3450–3453 (2008).
19. Osadchii, D. Y., Olivos-Suarez, A. I., Bavykina, A. V. & Gascon, J. Revisiting nitrogen species in covalent triazine frameworks. *Langmuir* **33**, 14278–14285 (2017).
20. Masteri-Farahani, M. New hybrid nanomaterial derived from immobilization of a molybdenum complex on the surface of multi-walled carbon nanotubes. *Journal of Sciences, Islamic Republic of Iran* **25**, 27–33 (2014).
21. Zhang, S., Kang, P., Ubnoske, S., *et al.* Polyethylenimine-Enhanced Electrocatalytic Reduction of CO₂ to Formate at Nitrogen-Doped Carbon Nanomaterials. *Journal Of The American Chemical Society* **136**, 7845–7848 (2014).
22. Katekomol, P., Roeser, J., Bojdys, M., Weber, J. & Thomas, A. Covalent Triazine Frameworks Prepared from 1,3,5-Tricyanobenzene. *Chemistry Of Materials* **25**, 1542–1548 (2013).
23. SAITO, Y., YOSHIKAWA, T., BANDOW, S., TOMITA, M. & HAYASHI, T. Interlayer Spacings In Carbon Nanotubes. *Physical Review B* **48**, 1907–1909 (1993).
24. Cui, W., Liu, Q., Cheng, N., Asiri, A. M. & Sun, X. Activated carbon nanotubes: a highly-active metal-free electrocatalyst for hydrogen evolution reaction. *Chemical communications* **50**, 9340–9342 (2014).

25. KANAKARAJAN, K. & CZARNIK, A. Synthesis And Some Reactions Of Hexaazatriphenylenehexacarbonitrile, A Hydrogen-free Polyfunctional Heterocycle With D_{3h} Symmetry. *Journal Of Organic Chemistry* **51**, 5241–5243 (1986).
26. Chang, T., Wu, B., Chiang, M., *et al.* Synthesis and mesomorphic behavior of a donor-acceptor-type hexaazatriphenylene. *Organic Letters* **7**, 4075–4078 (2005).

Conclusions

5.1 Conclusions

In this work, we have attempted to bring COFs a step closer towards industrialization. We did this in two ways.

One, by improving the synthesis conditions of imine-linked COFs so they are more amenable to industrial production. In **chapter 2**, we did an extensive optimization of reaction parameters, and found that a mixture of n-butanol with 10 v% H₂O and 4M AcOH is capable of producing a very broad range of COFs. Conveniently, this solvent is a bulk chemical, which is also relatively green and inexpensive. Using this solvent, the COF synthesis time and temperature could be reduced from 72 hours and 120 °C to 16 hours and 70 °C. This means the consumption of thermal energy drastically decreases and the space-time-yield increases. Perhaps most importantly, with this method, we scaled our imine COF synthesis to 10 gram. To the best of our knowledge, this is the largest reported amount of imine COF ever synthesized in one batch.

It is a long-standing question in COF synthesis as to why one solvent is capable of producing crystalline COFs, and others are not. In the same chapter, we could formulate for the first time a hypothesis that can answer this question. For this, we relied on the combined observations of optical microscopy, SEM, TEM, FT-IR and in situ Raman. According to our findings the key lies in stacking: apolar solvents with a sufficient amount of acid will promote the stitching together of protonated nanosheets, which in turns leads to better stacking. This stacking is vital to create robust crystalline COFs, which keep their crystallinity and porosity after

vacuum activation. The effect can be generalized to other apolar solvents, as long as they are still miscible with water and acetic acid.

In a second part, we focused on finding general ways to improve the application potential of covalent organic framework for carbon capture and utilization. In **chapter 3**, we explored linkage conversion as a strategy to enhance the CO₂-uptake of COFs. Specifically, we converted a nitrogen-rich imine-linked COF to a thiazole-linked COF using inexpensive molten sulfur. After successful conversion, the CO₂-uptake increased by 87%, to 3.93 mmol/g at 273 K.

Finally we studied new ways to make COFs useful catalysts for conversion of CO₂ to CO. In **chapter 4**, we tried to overcome the limited conductivity of CTFs to make them better suited as electrocatalysts for electrochemical conversion of CO₂. We could do this by growing layers of CTF *in situ* onto highly conductive multiwalled carbon nanotubes. The resulting hybrid materials show a significant improved catalytic activity: at least a tenfold increase in CO production as compared to a physical mixture of CTF and multiwalled carbon nanotubes.

In the second part of **chapter 2** we synthesized a new ligand, containing the terpyridine moiety. This tridentate ligand is very well suited to hold metals, which can be used as active sites for catalysis. As a proof of concept, we synthesized a new COF containing this ligand, using the method developed earlier in the chapter. After decoration with CuCl₂·2H₂O, this COF was capable of photocatalytically producing CO with 98.7% selectivity, without the use of sacrificial agents or photosensitizers.

Appendix

A

A.1 Supporting information of Chapter 1

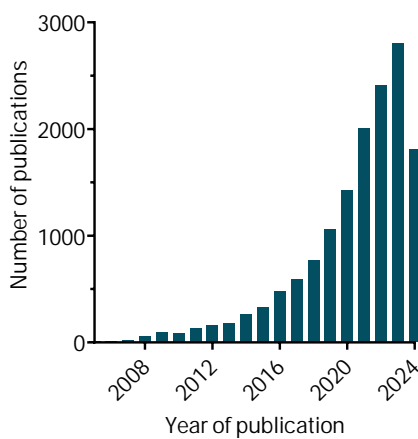


Figure A.1. The number of publications containing the keywords 'Covalent Organic Framework' or 'COF' according to Web Of Science, consulted August 2024.

A.2 Supporting information of Chapter 2

Name	Space Group	R _{wp}	R _p
TAPB-Ta	P-3	9.25%	6.61%
TAPB-TaBr ₂	P-3	5.56%	4.02%
TAPB-TaMe ₂	P-3	9.02%	5.32%
TAPB-TaOMe ₂	P-3	20.07%	13.56%
TAPB-TFB	P3	5.80%	4.26%
TAPM-Ta	I41/A	8.82%	6.54%
PDA-TFPPy	C222	11.31%	8.22%
TAPPy-Ta	C222	22.78%	16.02%
TAPT-IP	P31M	3.62%	2.60%
TAPT-TaMe ₂	P-3	6.33%	3.69%
TAPT-TFA	P3	12.64%	8.43%
TAPT-TFPO	P1	8.86%	6.89%

Table A.1. Overview of the Pawley refinement parameters for the different COFs

Name	S _{BET} (m ² /g)	C	R ²
TAPB-Ta	2107	54	0.9993
TAPB-TaBr ₂	1330	33	0.9996
TAPB-TaMe ₂	2164	24	0.9978
TAPB-TaOMe ₂	2329	27	0.9953
TAPB-TFB	1057	440	0.9999
TAPM-Ta	59	638	0.9990
PDA-TFPPy	1944	88	0.9960
TAPPy-Ta	2682	119	0.9990
TAPT-IP	570	128	0.9990
TAPT-TaMe ₂	2161	14	0.9985
TAPT-TFA	1505	232	0.9997
TAPT-TFPO	1204	930	1.0000

Table A.2. Overview of the BET surface areas and values for C and R² of the different COFs

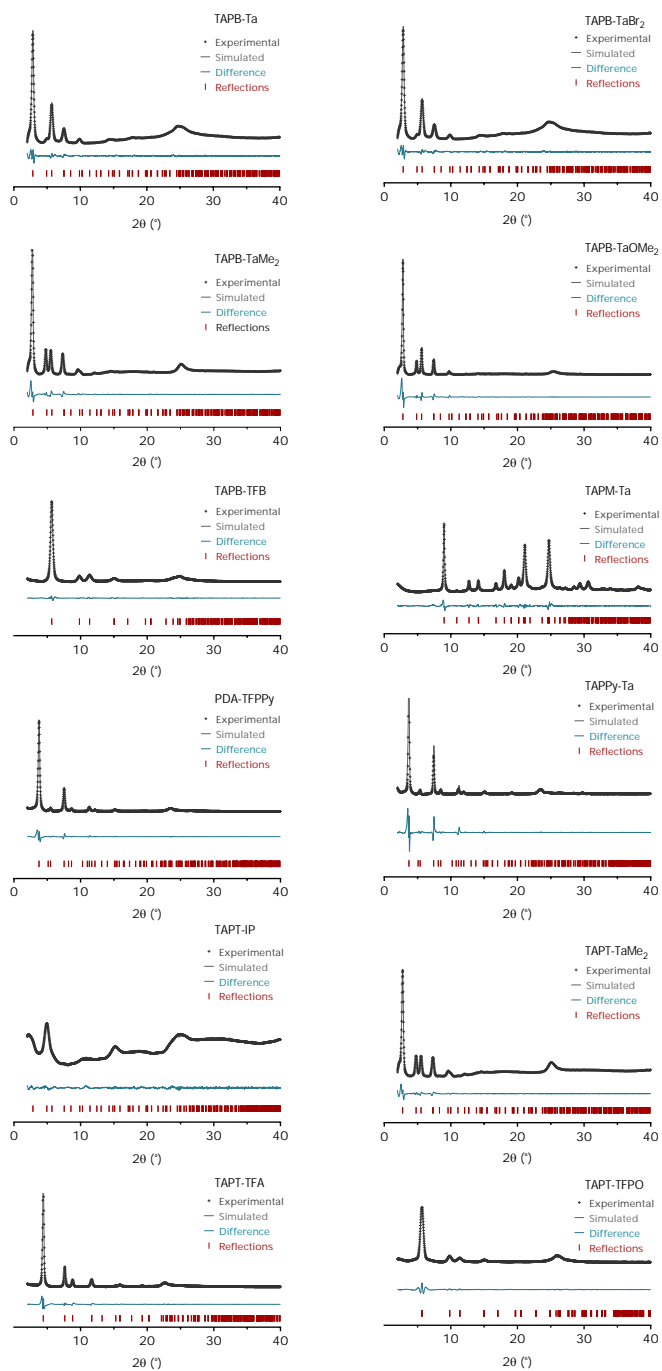


Figure A.2. Pawley refined PXRD patterns of the 12 synthesized COFs

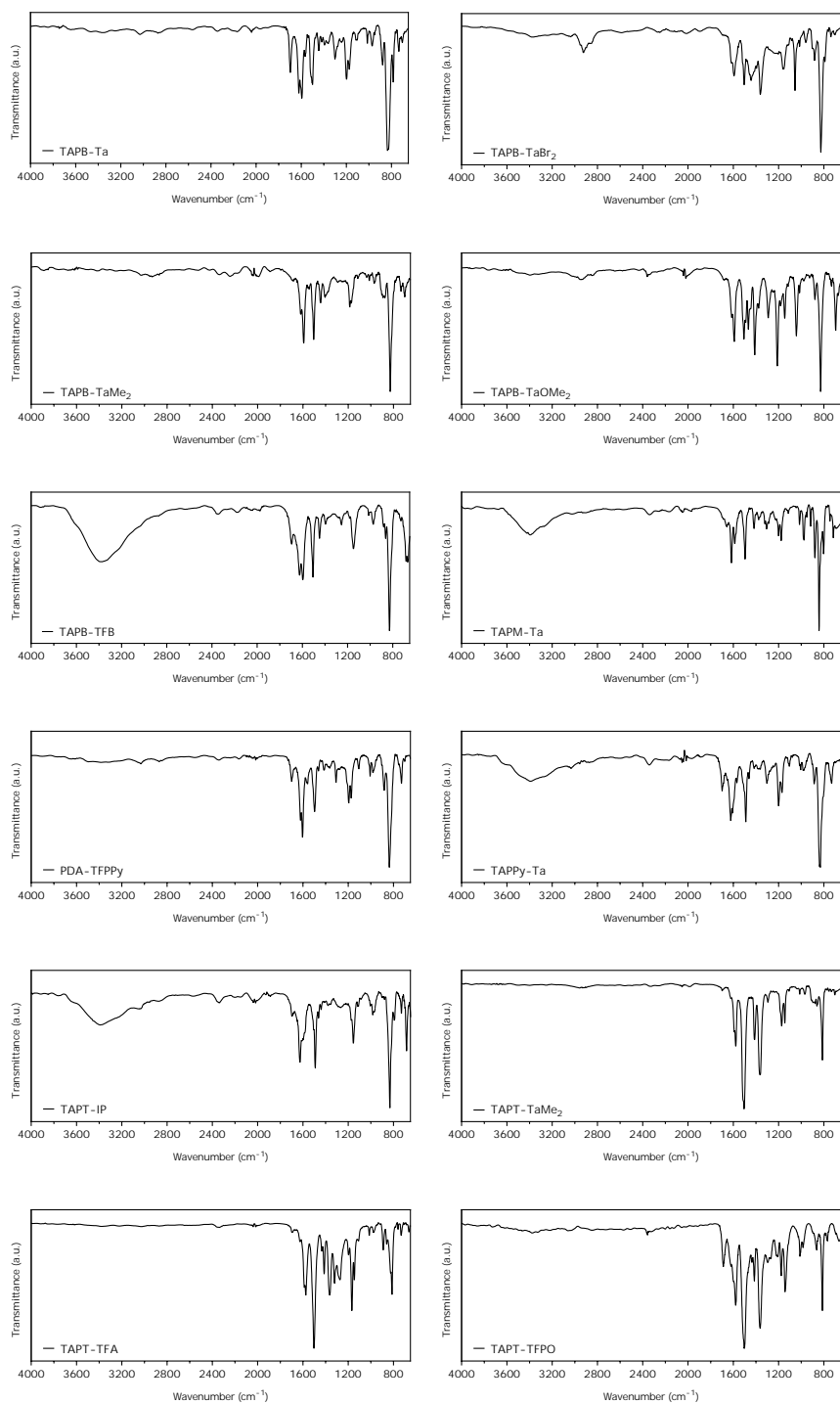


Figure A.3. FTIR spectra of the 12 synthesized COFs

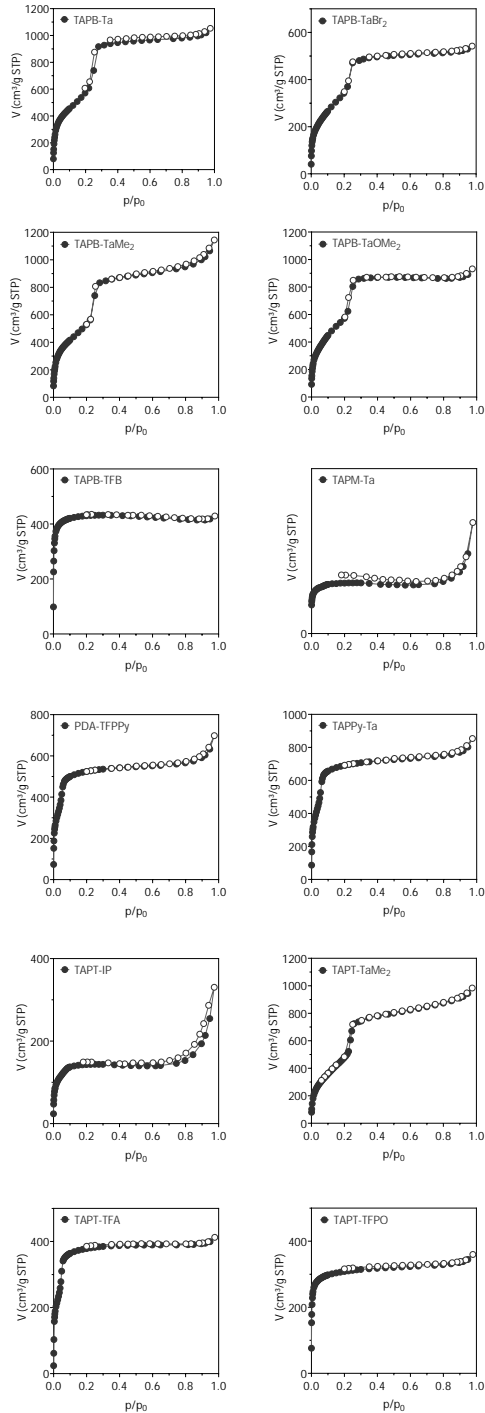


Figure A.4. N_2 -sorption isotherms of the 12 synthesized COFs

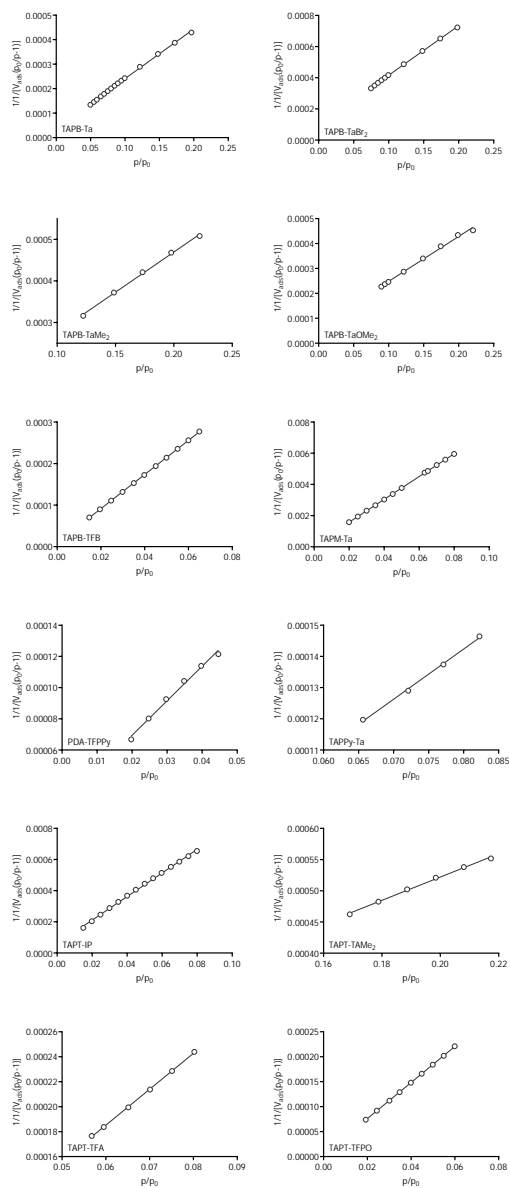


Figure A.5. BET plots of the 12 synthesized COFs

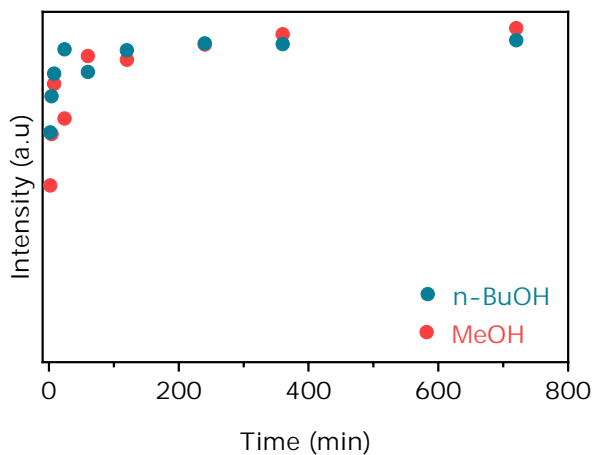


Figure A.6. Intensity over time of the peak at 1570 cm^{-1} during in situ Raman measurement during the synthesis of TAPB-TaBr₂ with multiplicative scattering correction (MSC) applied

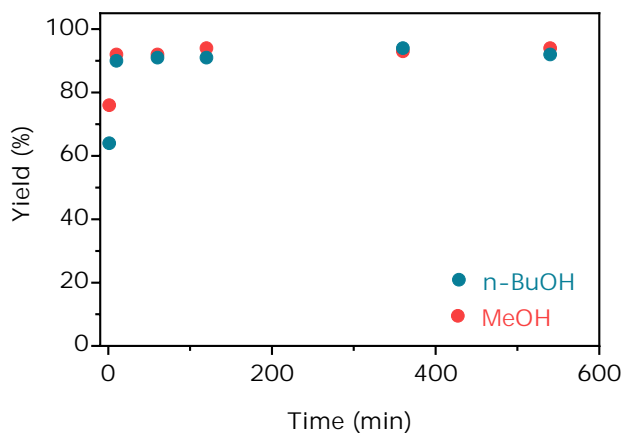


Figure A.7. Yield over time of TAPB-TaBr₂ in methanol or n-butanol, based on the weight of the COF after washing and drying

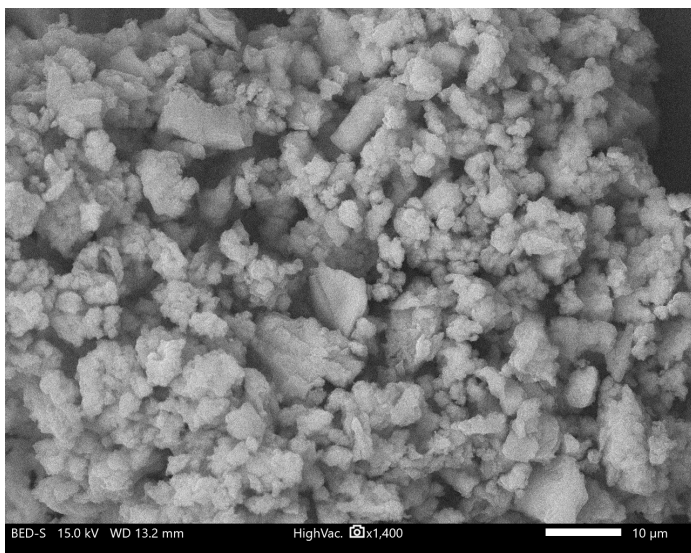


Figure A.8. SEM image of TAPB-TaBr₂ synthesized in n-BuOH

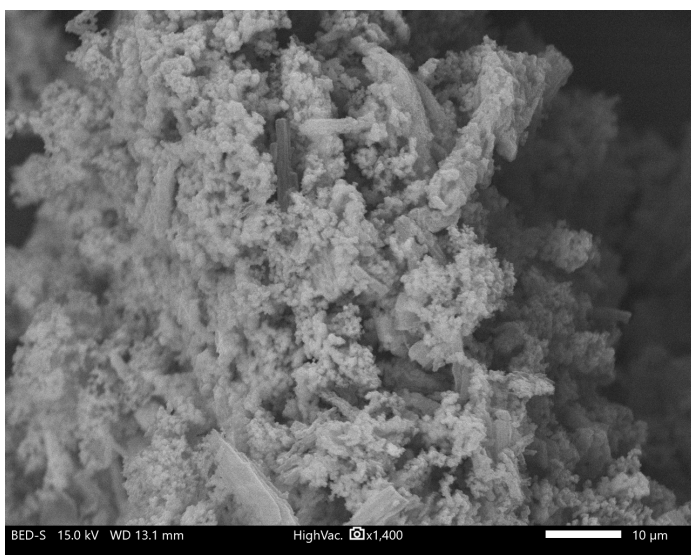


Figure A.9. SEM image of TAPB-TaBr₂ synthesized in MeOH

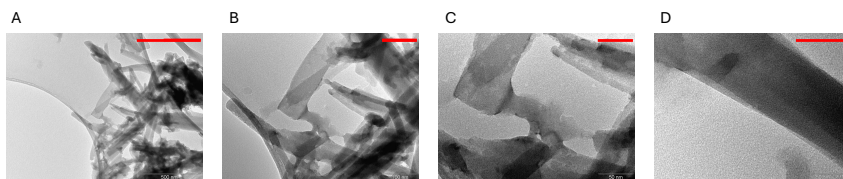


Figure A.10. TEM images of TAPB–TaBr₂ after 16 hours of synthesis at 70°C in n-BuOH containing 10 v% H₂O and 4 M AcOH with 80000 (A), 200000 (B), 400000 (C) and 600000 (D) magnification. The scale bars are 500 nm, 100 nm, 50 nm and 50 nm respectively.

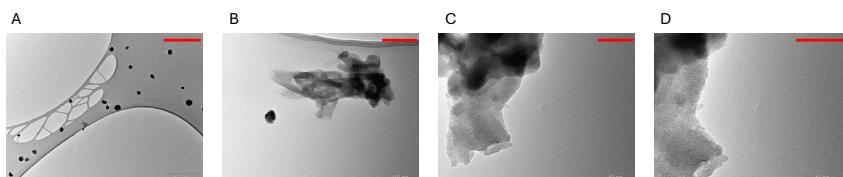


Figure A.11. TEM images of TAPB–TaBr₂ after 16 hours of synthesis at 70°C in MeOH containing 10 v% H₂O and 4 M AcOH with 50000 (A), 200000 (B), 400000 (C) and 600000 (D) magnification. The scale bars are 500 nm, 100 nm, 50 nm and 50 nm respectively.

COF	S _{BET} (m ² g ⁻¹)	Yield	FWHM (100) (°)	Time (h)	T (°C)	Solvent	Catalyst	Reference
TAPB-Ta	2107	88%	0.471	16	70	n-butanol	AcOH	This work
	2175	98%	-	0.5	25	1,4-dioxane:mesitylene	Sc(OTf) ₃	[1]
	2890	80%	-	72	120	1,4-dioxane:mesitylene	AcOH	[2]
	2035	87%	-	1	25	water	AcOH/sonication	[3]
	2121	-	0.446	72	120	1,4-dioxane:mesitylene	AcOH	[4]
1397	88.4%	-	2	25	o-dichlorobenzene:n-butanol	Fe(NO ₃) ₃	[5]	
TAPB-TaBr ₂	1330	92%	0.3277	16	70	n-butanol	AcOH	This work
	1393	91.5%	-	72	120	o-dichlorobenzene	/	[6]
	1376	93.5%	-	72	120	o-dichlorobenzene	/	[7]
	1200	86%	-	72	120	o-dichlorobenzene:n-butanol	Nb ₂ O ₅	[8]
TAPB-TaMe ₂	2164	91%	0.2867	16	70	n-butanol	AcOH	This work
	1850	75.7%	-	3	25	1,4-dioxane:mesitylene	Sc(OTf) ₃	[9]
	2050	67%	-	72	70	1,4-dioxane:mesitylene	AcOH	[10]
	2197	-	-	72	120	1,4-dioxane:mesitylene	AcOH	[11]
1810	81%	-	24	65	1,4-dioxane:mesitylene	AcOH	[12]	
TAPB-TaOMe ₂	2329	94%	0.2047	16	70	n-butanol	AcOH	This work
	1027	82%	-	72	120	o-dichlorobenzene:n-butanol	Sc(OTf) ₃	[13]
	2059	91%	-	1	25	water	AcOH/sonication	[3]
	2068	93.4%	0.73	2	25	o-dichlorobenzene:n-butanol	Fe(NO ₃) ₃	[5]
TAPB-TFB	1057	94%	0.4096	16	70	n-butanol	AcOH	This work
	810	-	-	72	120	1,4-dioxane:mesitylene	AcOH	[4]
	1268	92%	-	168	120	1,4-dioxane:mesitylene	AcOH	[14]
	962	-	-	72	25	acetonitrile	Sc(OTf) ₃	[15]
	1013	84%	-	1	25	water	AcOH/sonication	[3]
TAPM-Ta (hydrated)	59	84%	0.2048	16	70	n-butanol	AcOH	This work
	20	84%	-	48	90	1,4-dioxane	AcOH	[16]
PDA-TFPPy	1944	87%	0.2662	16	70	n-butanol	AcOH	This work
	2050	82%	-	96	120	o-dichlorobenzene:n-butanol	AcOH	[17]
	2032	80%	-	1	25	dioxane	plasma	[18]
TAPPy-Ta	2682	96%	0.1433	16	70	n-butanol	AcOH	This work
	2165	76%	-	1	25	o-dichlorobenzene:n-butanol	plasma	[18]
	1746	99%	-	1	25	water	AcOH/sonication	[3]
	3140	90%	-	4	70	o-dichlorobenzene:n-butanol	AcOH	[2]
	2093	69%	-	72	120	1,4-dioxane:mesitylene	AcOH	[19]
TAPT-IP	570	82%	0.7987	16	70	n-butanol	AcOH	This work
	30	-	-	48	25	1,4-dioxane:mesitylene	AcOH	[20]
	259	83%	-	1	25	water	AcOH/sonication	[3]
TAPT-TaMe ₂	2161	90%	0.2867	16	70	n-butanol	AcOH	This work
	1228	65%	-	24	65	1,4-dioxane:mesitylene	AcOH	[12]
TAPT-TFA	1505	83%	0.2253	16	70	n-butanol	AcOH	This work
	1550	-	-	72	120	o-dichlorobenzene:n-butanol	Nb ₂ O ₅	[13]
	1587	83%	-	1	25	water	AcOH/sonication	[3]
	1135	87.3%	-	72	120	1,4-dioxane:mesitylene	AcOH	[21]
TAPT-TFPO	1204	82%	0.4505	16	70	n-butanol	AcOH	This work
	1752	-	0.527	72	120	1,4-dioxane	AcOH	[22]
	1103	87.2%	-	72	120	1,4-dioxane	AcOH	[23]

Table A.3. Comparison between the yields, BET surface areas, and FWHM of the (100) peak in PXRD obtained by our method and some of the best literature results.

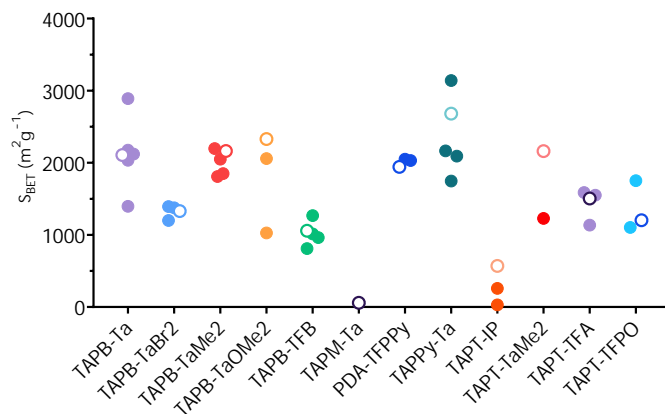


Figure A.12. Comparison between the BET surface areas obtained by our method and some of the best literature results. References and details of the literature synthesis methods can be found in **Table A.3**. The open circles are the values obtained by our method.

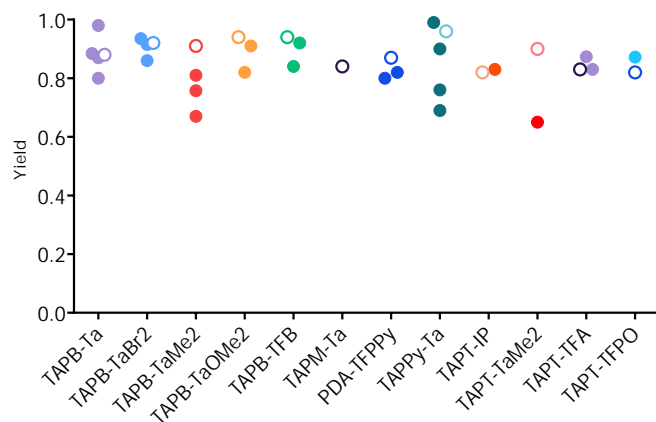


Figure A.13. Comparison between the yields obtained by our method and some of the best literature results. References and details of the literature synthesis methods can be found in **Table A.3**. The open circles are the values obtained by our method.

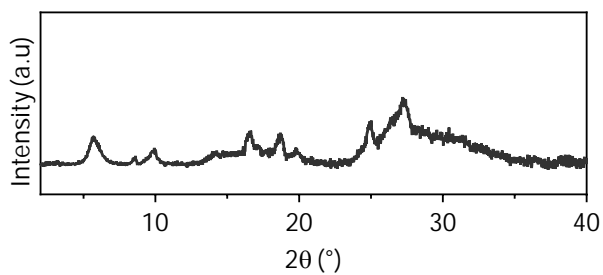


Figure A.14. PXRD pattern of the material resulting from the condensation of triformylphloroglucinol and TAPT



Figure A.15. Large scale synthesis of TAPT-TaMe₂

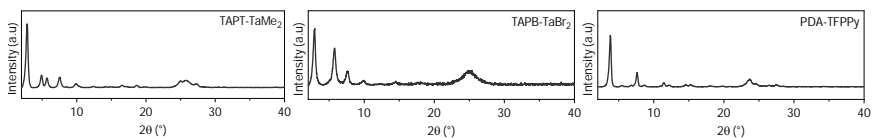


Figure A.16. XRD patterns of TAPT-TaMe₂ synthesized on 10 gram scale, and TAPB-TaBr₂ and PDA-TFPPy synthesized on 1 gram scale

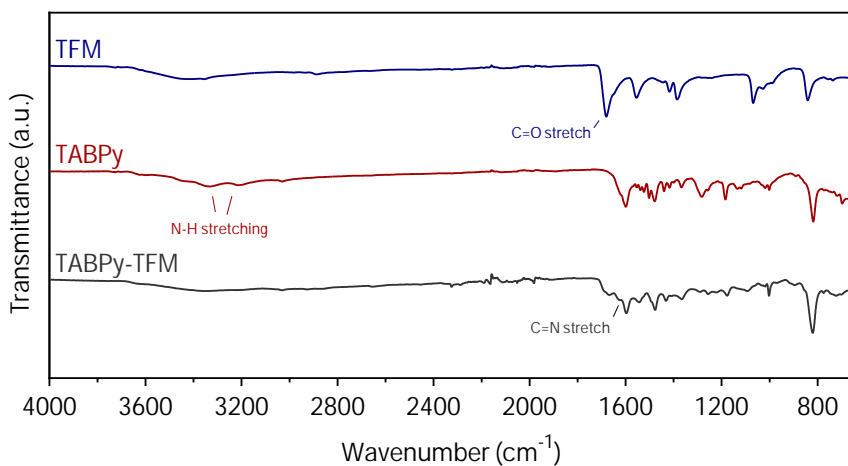


Figure A.17. FTIR spectra of TABPy, TFM and TABPy-TFM. The aldehyde C=O stretching vibration at 1680 cm⁻¹ diminishes in the spectrum of TABPy-TFM, while a new C=N stretching vibration at 1627 cm⁻¹ occurs.

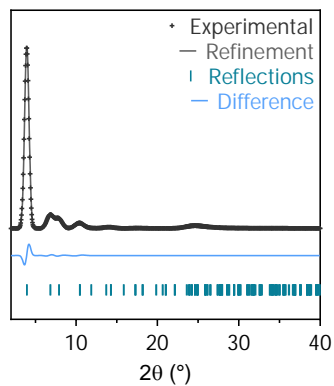


Figure A.18. Pawley refinement of TABPy-TFM with simulated AA stacking. Refinement parameters: $R_{WP} = 8.35\%$, $R_p = 6.40\%$

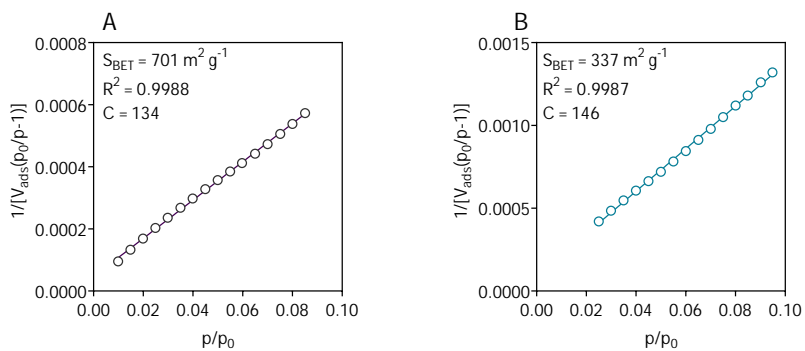


Figure A.19. BET plots of TABPy-TFM (A) and TABPy-TFM-Cu (B)

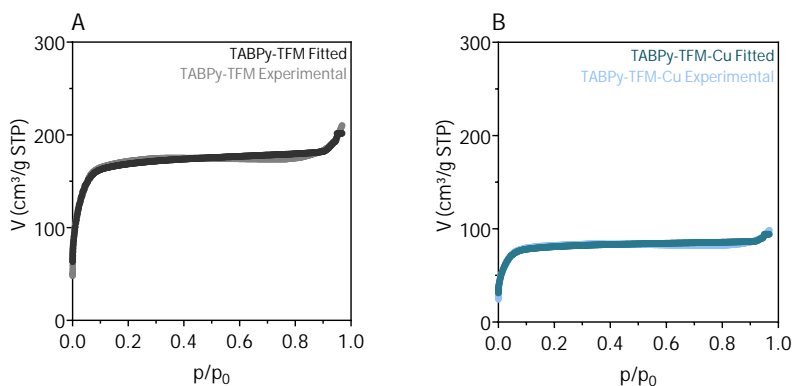


Figure A.20. Fitting comparison between the simulated and experimental isotherms for TABPy-TFM (A) and TABPy-TFM-Cu (B). The simulated isotherms were obtained from QSDFT, using the method "N₂ at 77 K on carbon (cylindrical/spherical pores, QSDFT adsorption branch)"

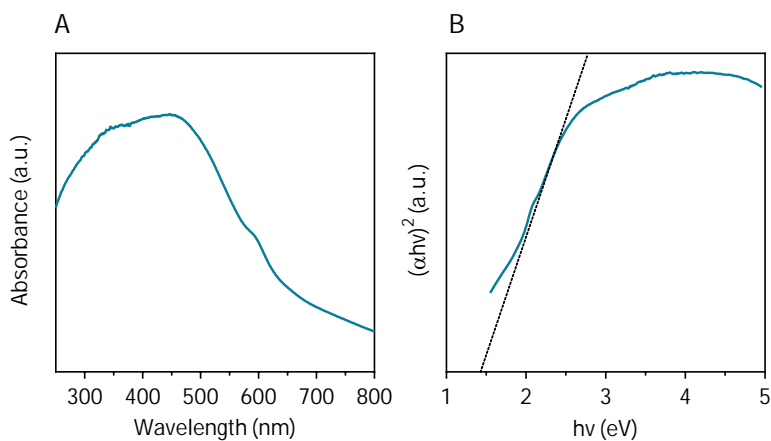


Figure A.21. UV-Vis measurement (A) and corresponding Tauc plot (B) of TABPy-TFM-Cu

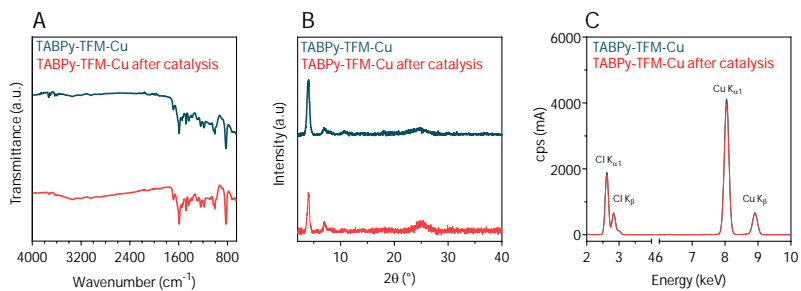


Figure A.22. FTIR spectra of TABPy-TFM-Cu before and after catalysis (A); PXRD patterns of TABPy-TFM-Cu before and after catalysis (B); XRF spectra of TABPy-TFM-Cu before and after catalysis (C)

A.3 Supporting information of Chapter 3

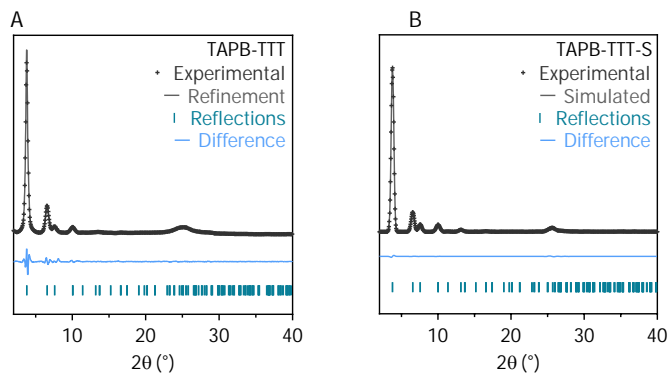


Figure A.23. Pawley refinement of TAPB-TTT with simulated AA stacking. Refinement parameters: $R_{WP} = 8.2\%$, $R_P = 8.2\%$ (A), Pawley refinement of TAPB-TTT-S with simulated AA stacking. Refinement parameters: $R_{WP} = 2.39\%$, $R_P = 1.27\%$ (B)

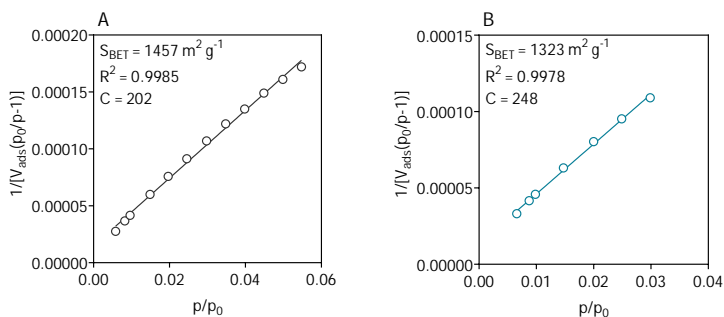


Figure A.24. BET plots of TAPB-TTT (A) and TAPB-TTT-S (B)

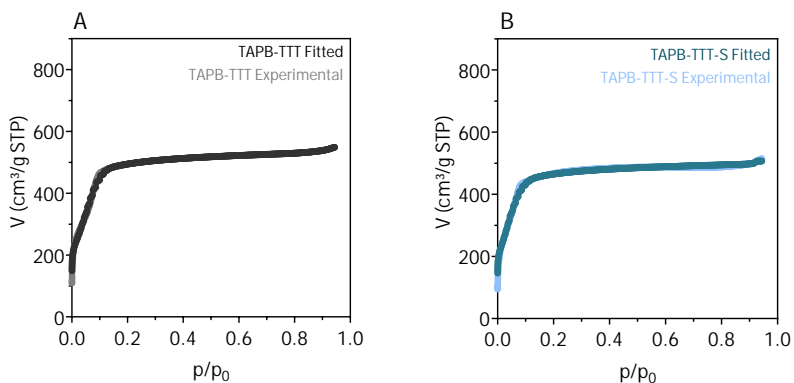


Figure A.25. Fitting comparison between the simulated and experimental isotherms for TAPB-TTT (A) and TAPB-TTT-S (B). The simulated isotherms were obtained from QSDFT, using the method " N_2 at 77 K on carbon (cylindrical/-spherical pores, QSDFT adsorption branch)"

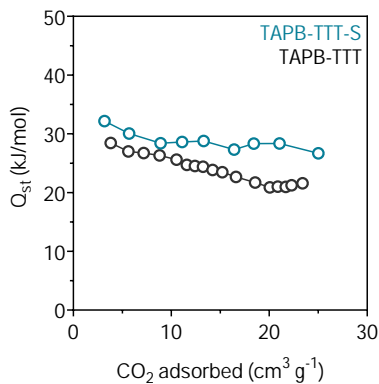


Figure A.26. The isothermic heat of adsorption of CO_2 of TAPB-TTT and TAPB-TTT-S

A.4 Supporting information of Chapter 4

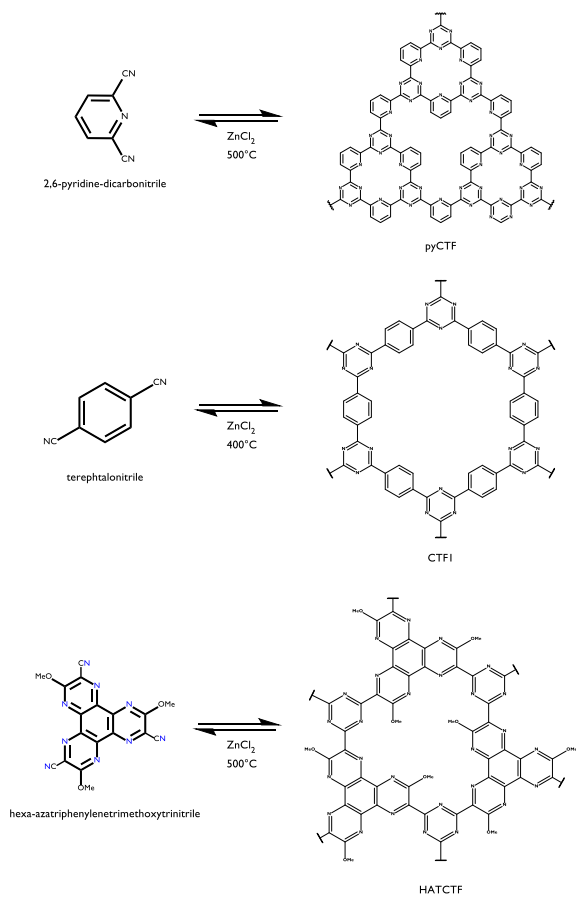


Figure A.27. Ionothermal synthesis of pyCTF, CTF1 and HATCTF

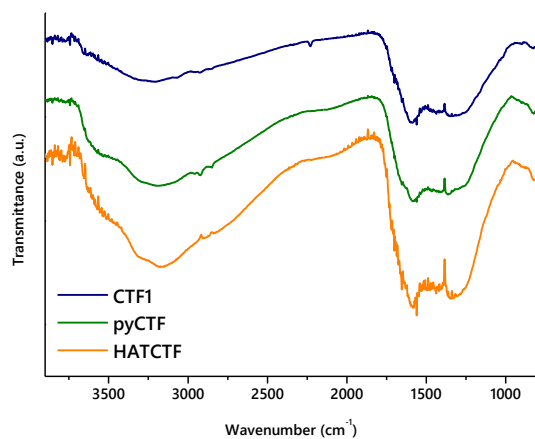


Figure A.28. DRIFTS spectra of CTF1, pyCTF and HATCTF. The broad peaks at around 1570 cm^{-1} and 1350 cm^{-1} were ascribed to the triazine ring vibrations. The absence of a nitrile peak around 2230 cm^{-1} indicates the successful trimerization of the nitrile-containing monomer.

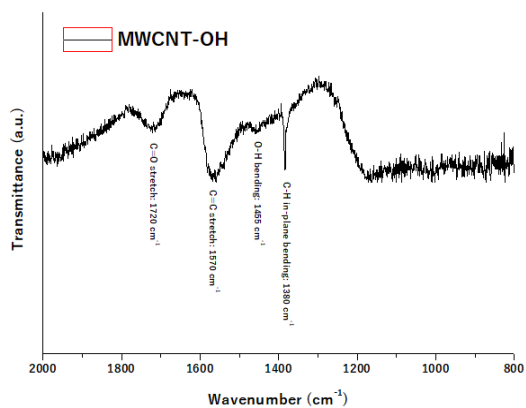


Figure S4: FTIR-ATR spectrum detail of MWCNT-OH

Figure A.29. FTIR-ATR spectrum detail of MWCNT-OH

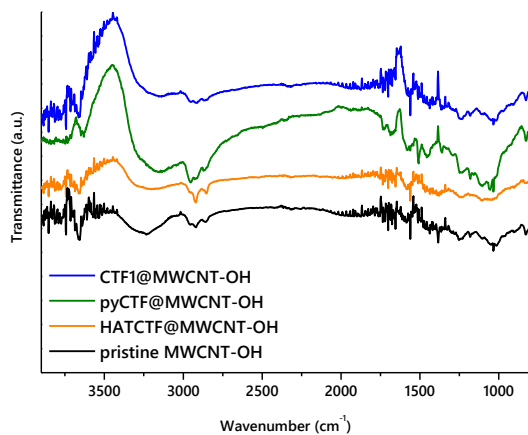


Figure A.30. DRIFTS spectra of CTF1@MWCNT-OH, pyCTF@MWCNT-OH and HATCTF@MWCNT-OH

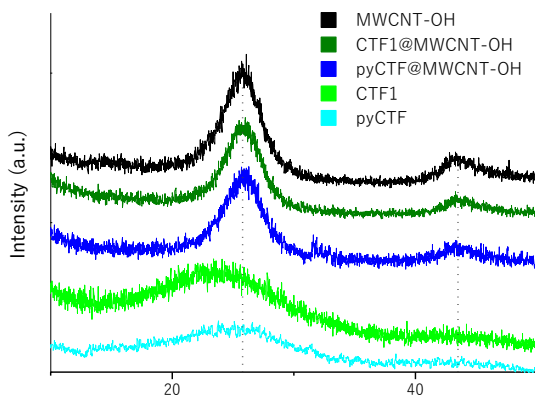


Figure A.31. PXRD patterns of MWCNT-OH, CTF1, pyCTE, CTF1@MWCNT-OH and pyCTF@MWCNT-OH

	C (at%)	O (at%)	N (at%)	Cl (at%)	Zn (at%)
MWCNT-OH	95.58	3.96			
CTF1@MWCNT-OH	92.19	3.32	3.6		
pyCTF@MWCNT-OH	91.78	2.81	4.48	0.31	0.15
HATCTF@MWCNT-OH	88.53	3.7	6.32		0.15

Table A.4. XPS elemental atomic percentages of MWCNT-OH and hybrid materials

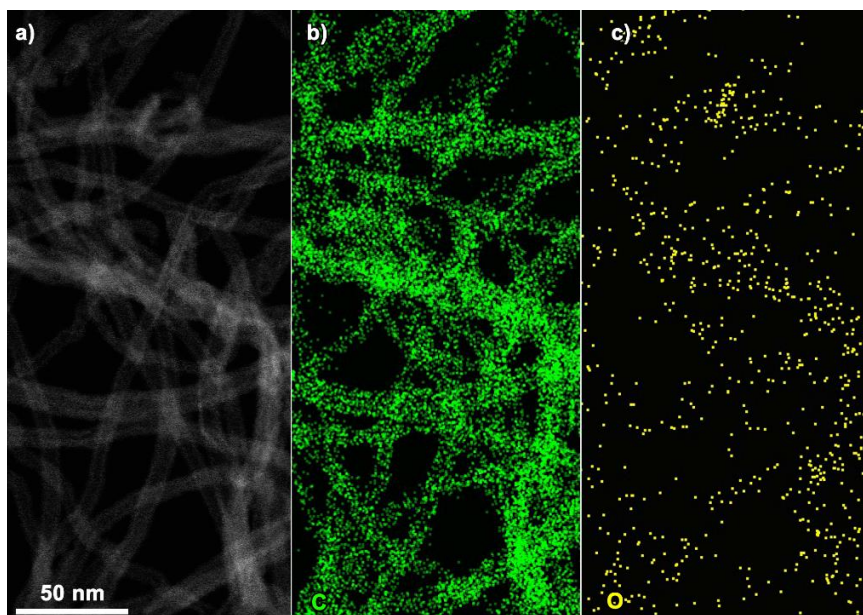


Figure A.32. STEM-EDX of MWCNT-OH

	Fe (g/kg)	Zn (g/kg)	Cu (mg/kg)	Mn (mg/kg)
HATCTF@MWCNT-OH	6.91	11.8	119	101
pristine MWCNT-OH	3.22	0.0604	76.9	88.8

Table A.5. ICP-MS analysis of HATCTF@MWCNT-OH and pristine MWCNT-OH

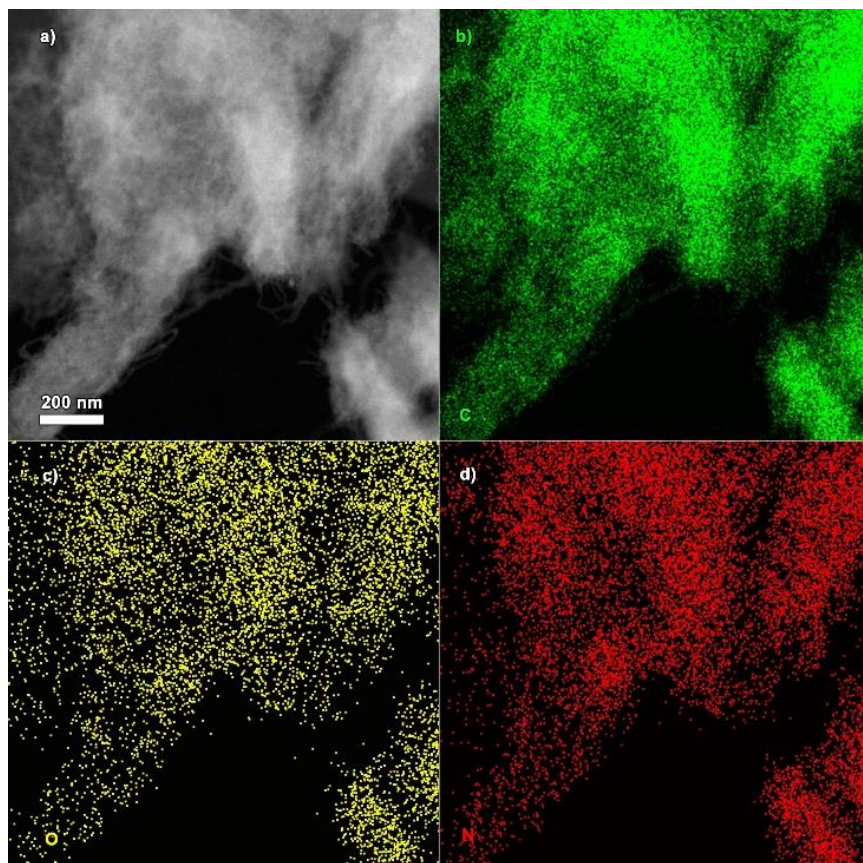


Figure A.33. STEM-EDX of pyCTF@MWCNT-OH

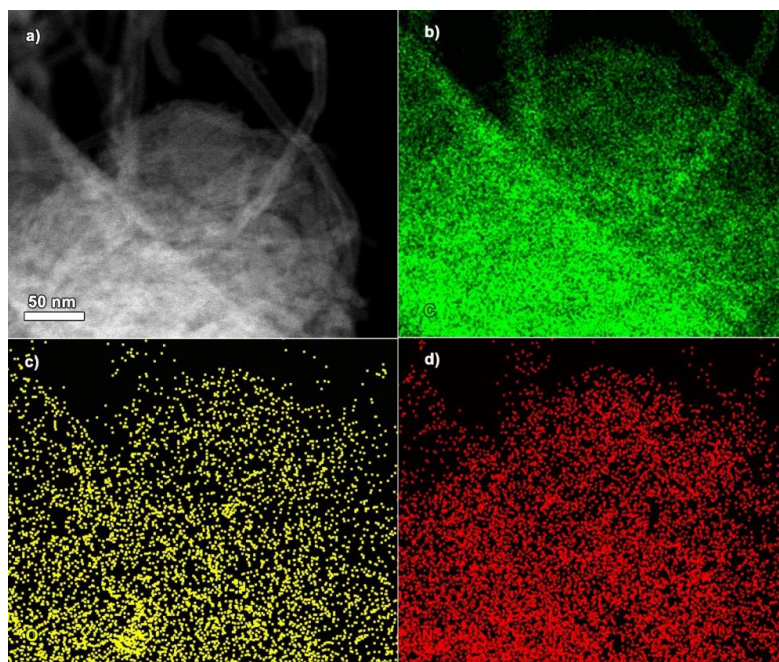


Figure A.34. STEM-EDX of HATCTF@MWCNT-OH

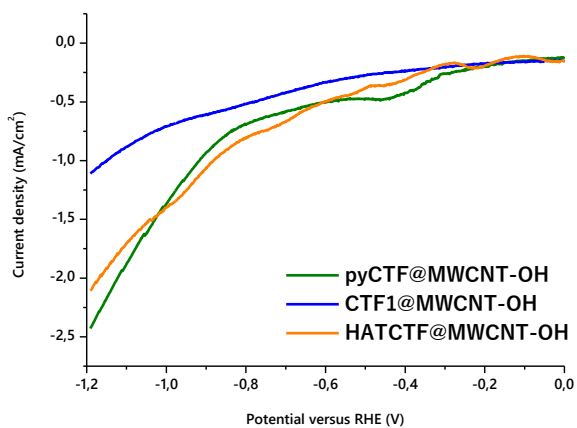


Figure A.35. LSV curves of pyCTF@MWCNT-OH, CTF1@MWCNT-OH and HATCTF@MWCNT-OH. Recorded in 0.1 M KHCO_3 at 5 mV/s

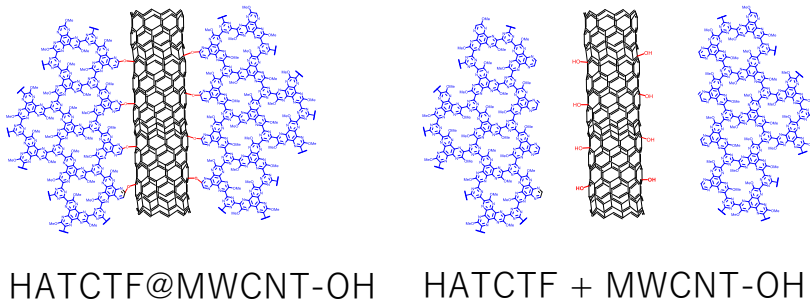


Figure A.36. Schematic interpretation of the structures of HATCTF@MWCNT-OH and HATCTF+MWCNT-OH

A.5 Scientific Publications

- Laemont, A., Abednatanzi, S., Derakshandeh, P. G., Verbruggen, F., Fiset, E., Qin, Q., Van Daele, K., Meledina, M., Schmidt, J., Oschatz, M., Van Der Voort, P., Rabaey, K., Antonietti, M., Breugelmans, T. & Leus, K. Covalent triazine framework/carbon nanotube hybrids enabling selective reduction of CO₂ to CO at low overpotential. *Green Chemistry* **22**, 3095–3103 (2020).
- Krishnaraj, C., Sekhar Jena, H., Bourda, L., Laemont, A., Pachfule, P., Roeser, J., Chandran, C. V., Borgmans, S., Rogge, S. M., Leus, K., Stevens, C. V., Martens, J. A., Van Speybroeck, V., Breynaert, E., Thomas, A. & Van Der Voort, P. Strongly Reducing (Diaryl-amino)benzene-Based Covalent Organic Framework for Metal-Free Visible Light Photocatalytic H₂O₂ Generation. *Journal of the American Chemical Society* **142**, 20107–20116 (2020)
- Chen, H., Liu, W., Laemont, A., Krishnaraj, C., Feng, X., Rohman, E., Meledina, M., Zhang, Q., Van Deun, R., Leus, K. & Van Der Voort, P. A Visible-Light-Harvesting Covalent Organic Framework Bearing Single Nickel Sites as a Highly Efficient Sulfur–Carbon Cross-Coupling Dual Catalyst. *Angewandte Chemie - International Edition* **60**, 10820–10827 (2021)
- Kaliya Perumal Veerapandian, S., De Geyter, N., Giraudon, J.-M., Morin, J.-C., Esbah Tabaei, P. S., De Weireld, G., Laemont, A., Leus, K., Van Der Voort, P., Lamonier, J.-F. & Morent, R. Effect of non-thermal plasma in the activation and regeneration of 13X zeolite for enhanced VOC elimination by cycled storage and discharge process. *Journal of Cleaner Production* **364** (2022).
- Debruyne, M., Borgmans, S., Radhakrishnan, S., Breynaert, E., Vrielinck, H., Leus, K., Laemont, A., De Vos, J., Rawat, K. S., Vanlommel, S., Rijckaert, H., Salemi, H., Everaert, J., Vanden Bussche, E., Poelman, D., Morent, R., De Geyter, N., Van Der Voort, P., Van

Speybroeck, V. & Stevens, C. V. Engineering of Phenylpyridine- and Bipyridine-Based Covalent Organic Frameworks for Photocatalytic Tandem Aerobic Oxidation/Povarov Cyclization. *ACS Applied Materials and Interfaces* **15**, 35092–35106 (2023)

- Sun, J., Sekhar Jena, H., Krishnaraj, C., Singh Rawat, K., Abednatanzi, S., Chakraborty, J., Laemont, A., Liu, W., Chen, H., Liu, Y.-Y., Leus, K., Vrielinck, H., Van Speybroeck, V. & Van Der Voort, P. Pyrene-Based Covalent Organic Frameworks for Photocatalytic Hydrogen Peroxide Production. *Angewandte Chemie - International Edition* **62** (2023)
- Deng, M., Sun, J., Laemont, A., Liu, C., Wang, L., Bourda, L., Chakraborty, J., Van Hecke, K., Morent, R., De Geyter, N., Leus, K., Chen, H. & Van Der Voort, P. Extending the π -conjugation system of covalent organic frameworks for more efficient photocatalytic H₂O₂ production. *Green Chemistry* **25**, 3069–3076 (2023)
- Sun, J., Chakraborty, J., Deng, M., Laemont, A., Feng, X., Liu, Y.-Y. & Van Der Voort, P. Metal-organic frameworks and covalent organic frameworks as photocatalysts for H₂O₂ production from oxygen and water. *Journal of Materials Chemistry A* **11**, 21516–21540 (2023)
- Debruyne, M., Raeymackers, N., Vrielinck, H., Radhakrishnan, S., Breynaert, E., Delaey, M., Laemont, A., Leus, K., Everaert, J., Rijckaert, H., Poelman, D., Morent, R., De Geyter, N., Van Der Voort, P., Van Speybroeck, V., Stevens, C. V. & Heugebaert, T. S. A. Development of Porous Organic Polymers as Metal-Free Photocatalysts for the Aromatization of N-Heterocycles. *ChemCatChem* **16** (2024).
- Laemont, A., Matthys, G., Lavendomme, R. & Van Der Voort, P. Mild and Scalable Conditions for the Solvothermal Synthesis of Imine-Linked Covalent Organic Frameworks. *accepted at Angewandte Chemie - International Edition* (2024)

- Matthys, G., Laemont, A., De Geyter, N., Morent, R., Lavendomme, R. & Van Der Voort, P. Robust Imidazopyridinium Covalent Organic Framework as Efficient Iodine Capturing Materials in Gaseous and Aqueous Environment. *Small*, 2404994 (2024).

References

1. Matsumoto, M., Dasari, R. R., Ji, W., *et al.* Rapid, low temperature formation of imine-linked covalent organic frameworks catalyzed by metal triflates. *Journal of the American Chemical Society* **139**, 4999–5002 (2017).
2. Feriante, C. H., Jhulki, S., Evans, A. M., *et al.* Rapid Synthesis of High Surface Area Imine-Linked 2D Covalent Organic Frameworks by Avoiding Pore Collapse During Isolation. *Advanced Materials* **32**, 1905776 (2020).
3. Zhao, W., Yan, P., Li, B., *et al.* Accelerated synthesis and discovery of covalent organic framework photocatalysts for hydrogen peroxide production. *Journal of the American Chemical Society* **144**, 9902–9909 (2022).
4. Zhu, D. & Verduzco, R. Ultralow surface tension solvents enable facile COF activation with reduced pore collapse. *ACS applied materials & interfaces* **12**, 33121–33127 (2020).
5. Zhu, D., Zhang, Z., Alemany, L. B., *et al.* Rapid, ambient temperature synthesis of imine covalent organic frameworks catalyzed by transition-metal nitrates. *Chemistry of Materials* **33**, 3394–3400 (2021).
6. Zhao, L., Tang, X., Ni, X., *et al.* Efficient and Selective Adsorption of cis-Diols via the Suzuki–Miyaura Cross-Coupling-Modified Phenylboronic-Acid Functionalized Covalent Organic Framework. *Langmuir* **40**, 1884–1891 (2024).
7. Liu, Q., Liao, Q., Hu, J., *et al.* Covalent organic frameworks anchored with frustrated Lewis pairs for hydrogenation of alkynes with H₂. *Journal of Materials Chemistry A* **10**, 7333–7340 (2022).
8. Zhu, Y., Zhu, D., Yan, Q., *et al.* Metal oxide catalysts for the synthesis of covalent organic frameworks and one-step preparation of covalent organic framework-based composites. *Chemistry of Materials* **33**, 6158–6165 (2021).

9. Corcos, A. R., Levato, G. A., Jiang, Z., *et al.* Reducing the pore size of covalent organic frameworks in thin-film composite membranes enhances solute rejection. *ACS Materials Letters* **1**, 440–446 (2019).
10. Burke, D. W., Sun, C., Castano, I., *et al.* Acid exfoliation of imine-linked covalent organic frameworks enables solution processing into crystalline thin films. *Angewandte Chemie* **132**, 5203–5209 (2020).
11. Yang, Y., Kang, J., Li, Y., *et al.* Enhanced photocatalytic hydrogen peroxide production activity of imine-linked covalent organic frameworks via modification with functional groups. *New Journal of Chemistry* **46**, 21605–21614 (2022).
12. Kang, C., Zhang, Z., Usadi, A. K., *et al.* Aggregated structures of two-dimensional covalent organic frameworks. *Journal of the American Chemical Society* **144**, 3192–3199 (2022).
13. Zhu, Y., Zhu, D., Yan, Q., *et al.* Metal oxide catalysts for the synthesis of covalent organic frameworks and one-step preparation of covalent organic framework-based composites. *Chemistry of Materials* **33**, 6158–6165 (2021).
14. Li, X., Gao, Q., Aneesh, J., *et al.* Molecular engineering of bandgaps in covalent organic frameworks. *Chemistry of Materials* **30**, 5743–5749 (2018).
15. Li, W., Bie, Z., Zhang, C., *et al.* Combinatorial synthesis of covalent organic framework particles with hierarchical pores and their catalytic application. *Journal of the American Chemical Society* **145**, 19283–19292 (2023).
16. Fischbach, D. M., Rhoades, G., Espy, C., Goldberg, F. & Smith, B. J. Controlling the crystalline structure of imine-linked 3D covalent organic frameworks. *Chemical Communications* **55**, 3594–3597 (2019).
17. Waller, P. J., AlFaraj, Y. S., Diercks, C. S., Jarenwattananon, N. N. & Yaghi, O. M. Conversion of imine to oxazole and thiazole linkages

- in covalent organic frameworks. *Journal of the American Chemical Society* **140**, 9099–9103 (2018).
18. He, J., Jiang, X., Xu, F., *et al.* Low power, low temperature and atmospheric pressure plasma-induced polymerization: facile synthesis and crystal regulation of covalent organic frameworks. *Angewandte Chemie* **133**, 10072–10077 (2021).
 19. Meng, Y., Lin, G., Ding, H., Liao, H. & Wang, C. Impregnation of sulfur into a 2D pyrene-based covalent organic framework for high-rate lithium–sulfur batteries. *Journal of Materials Chemistry A* **6**, 17186–17191 (2018).
 20. Krishnaraj, C., Jena, H. S., Rawat, K. S., *et al.* Linker engineering of 2D imine covalent organic frameworks for the heterogeneous palladium-catalyzed Suzuki coupling reaction. *ACS Applied Materials & Interfaces* **14**, 50923–50931 (2022).
 21. Yang, J., Acharjya, A., Ye, M.-Y., *et al.* Protonated Imine-Linked Covalent Organic Frameworks for Photocatalytic Hydrogen Evolution. *Angewandte Chemie International Edition* **60**, 19797–19803 (2021).
 22. Hu, H., Tao, Y., Wang, D., *et al.* Rational modification of hydroxy-functionalized covalent organic frameworks for enhanced photocatalytic hydrogen peroxide evolution. *Journal of Colloid and Interface Science* **629**, 750–762 (2023).
 23. Chen, Y., Luo, X., Zhang, J., *et al.* Bandgap engineering of covalent organic frameworks for boosting photocatalytic hydrogen evolution from water. *Journal of Materials Chemistry A* **10**, 24620–24627 (2022).